MATERIALS AND DEVICES FOR MECHANICALLY FLEXIBLE INTEGRATED PHOTONICS

by

Lan Li

A dissertation submitted to the Faculty of the University of Delaware in partial fulfillment of the requirements for the degree of Doctor of Philosophy in Materials Science and Engineering

Winter 2016

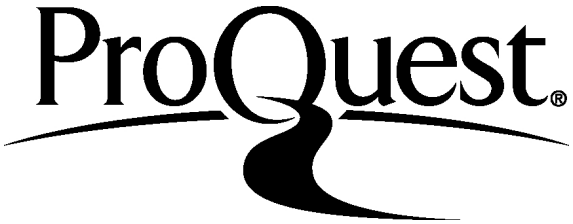

MATERIALS AND DEVICES FOR MECHANICALLY FLEXIBLE

INTEGRATED PHOTONICS

by

Lan Li

Approved: _____

Darrin J. Pochan, Ph.D.
Chair of the Department of Materials Science and Engineering

Approved: _____

Babatunde A. Ogunnaike, Ph.D.
Dean of the College of Engineering

Approved: _____

Ann L. Ardis, Ph.D.
Interim Vice Provost for Graduate and Professional Education

I certify that I have read this dissertation and that in my opinion it meets the academic and professional standard required by the University as a dissertation for the degree of Doctor of Philosophy.

Signed: _____

Juejun Hu, Ph.D.
Professor in charge of dissertation

I certify that I have read this dissertation and that in my opinion it meets the academic and professional standard required by the University as a dissertation for the degree of Doctor of Philosophy.

Signed: _____

Joshua Zide, Ph.D.
Member of dissertation committee

I certify that I have read this dissertation and that in my opinion it meets the academic and professional standard required by the University as a dissertation for the degree of Doctor of Philosophy.

Signed: _____

Matthew F. Doty, Ph.D.
Member of dissertation committee

I certify that I have read this dissertation and that in my opinion it meets the academic and professional standard required by the University as a dissertation for the degree of Doctor of Philosophy.

Signed: _____

Michael Haney, Ph.D.
Member of dissertation committee

ACKNOWLEDGMENTS

Without the help and efforts from a lot of people, I really cannot complete this dissertation right now. Here I would like to acknowledge them one by one.

Firstly, I would like to express my sincere gratitude towards my advisor Dr. Juejun Hu for his continuous support of my Ph.D study. Thanks for his wisdom and knowledge that can always help me find the solutions to the problems in the experiments; thanks for his motivation and patience that can always encourage me to overcome the difficulties bravely; and also thanks for his friendship that make me realize that he is not only an advisor in the research, a mentor in my career path, but also a friend in my life.

My exceptional thanks also go to Dr. Michael E. Mackay. Thanks for his insightful supportive and invaluable supervision in the first one and a half of my Ph.D. years. His guidance directs me to learn how to conduct a research project step by step from the very beginning.

Besides my advisors, I would like to thank the rest of my thesis committee: Dr. Joshua Zide, Dr. Matthew F. Doty and Dr. Michael Haney for their precious time, insightful comments and continuous encouragement. I did learn a lot from their questions and suggestions towards my thesis project from different perspectives.

Also deserving special thanks are my collaborators. Firstly of all, let me acknowledge Dr. Kathleen Richardson, Dr. J. David Musgraves, and Sylvain Danto from University of Central Florida for the long-lasting supply of chalcogenide glass, which is so important to us that we cannot achieve anything without their support.

Besides, I am also willing to deliver my appreciation to Dr. Nanshu Lu, Shutao Qiao from University of Texas at Austin and Dr. Jingjing Li, Wei-ming Wang from University of Hawaii at Manoa for their efforts and contribution in the development and simulation of the multi-neutral axis mechanical design. Then please let me thank Dr. Xinqiao Jia, Aidan B. Zerdoum for their collaboration in the cytocompatibility test of the fabricated TiO_2 photonic devices. Also I feel grateful towards Dr. Michael Haney at University of Delaware and Dr. Xiaochen Sun, Dr. Ning-Ning Feng from LaXense Inc for their helpful discussion and suggestion in the design and power consumption analysis of optical interconnect design. Thanks for all of my collaborators for their contribution and scientific guidance in my research project.

Here I would like to acknowledge my fellow labmates (Hongtao Lin, Yi Zou, Okechukwu Anthony Ogbuu, Qingyang Du, Sarah Geiger, Jerome Michon, Derek Kita, Duanhui Li, Tian Gu, Gufan Yin) for the stimulating discussions, selfless help and for all the fun we have had in the last few years. Thanks for their efforts to help me get familiar with the new environment and new reach field quickly since I became one of them. I feel really lucky that I joined this dynamic group and obtained the chance to both work and live happily with them. Also I am grateful to have the chance to work with the visiting scholars (Dr. Ping Zhang, Dr. Wei Zhang, Dr. Li Zhang), visiting graduates (Junying Li, Yizhong Huang), visiting undergraduates (Yangchen Liu , Nicholas Gelardo) and high school intern (Nicholas Xiao). Thanks for their contribution and help in the experiment study such as sol-gel preparation, thin film deposition and data analysis. Certainly I also would like to express my gratitude towards my colleagues (Jeong Jae Wie, Ngoc A. Nguyen, Roddel Remy, Wenluan Zhang, Hao Shen, Brett Guralnick, and Robert Jones) in Dr. Mackey's group. Thanks for their understanding

and help for the use of some characterization equipment such as XRD, DMA TGA, DSC, DLS, AFM, SEM and so on.

I am also greatly appreciated for the assistance and support from my friends, colleagues and the staffs at both University of Delaware and MIT. They all helped me in various ways so that I can accomplish this thesis work. I would like to acknowledge Mathew Zablocki, David Eng, Maciej Murakowski, Stephen Kozacik and Alicia Zablocki in Dr. Dennis Prather's group for their kindness and sharing with us their expertise in the use of equipment such as AB-M mask aligner, Reactive ion etching. Many thanks also go to Jinglin Liu, Bin Wei, Jing Qu and Chin-Chen Kuo from Dr. David Martin's group; Liang Gong from Dr. John Rabolt's group; Xinran Zhou from Dr. Matthew F. Doty's group; Yujun Zhong from Dr. Joshua Zide's group; Xian Xu, Xi Long, XiaoWei Yang from Dr. Xinqiao Jia's group; Tianzhi Luo from Dr. Kristi Kiick's group; Ming Luo from Dr. Thomas Epps's group; Danning Zhang from Dr. John Gillespie's group; Roy Murray from S. Ismat Shah's group; Dr. Fei Deng, Dr. Chaoying Ni and Frank Kriss for their support and assistance in the use of experiments such as SEM, FIB, EDX, FT-IR, Uv-vis, Ellipsometry, SEM, FIB, DLS, AFM, XRD, GPC, etc; Besides, I am also willing to express my gratitudes towards Charlie Garbini, Kjeld Krag-Jensen, Kurt Broderick, Gary Riggott for their advice on experiment safety and instruction for the use of lab tools; Kathleen Forwood, Christine Williamson, Robin Buccos, Naima Hall and Lisa Sinclair for their assistance so that I can graduate smoothly.

Furthermore, I still need thank all of my friends who shared lots of happy memories with me during the past few years. Thanks to Songwei Zheng, Queming Qiu for taking of me like brother and sister; thanks to Jinglin Liu, Bin Wei, Jiayin Wang,

Selina Huang, Jingsi Gao, Ming Luo, etc for the accompany and unforgettable days we have spent together.

Last but not the least, I would express my deep thanks to my dear family. Thanks for always being there for me and supporting me, especially my parents and sisters. Their unconditional love and support will always be the sunshine when I come across difficulties. Also special thanks to my husband Hongtao for his 9 years' companion in both my life and work. Certainly I won't miss my angel, Lucas. Thanks for his coming to our family. His arrival shows me a lot about the beauty and delicacy of life, which makes me understand better to live with gratitude towards the world.

TABLE OF CONTENTS

LIST OF TABLES

LIST OF FIGURES

ABSTRACT

Flexible integrated photonics is a new technology that has only started to burgeon in the past few years, which enables a wide cross-section of emerging applications ranging from flexible optical interconnects to conformal sensors on biological tissues. Such devices are traditionally fabricated using pattern transfer methods. However these techniques are relatively complicated and limit the fabrication yield. Direct patterning of a-Si devices on a polymer substrate has recently been reported; nevertheless, the optical quality of the a-Si film is compromised due to the low deposition temperature. This thesis includes our work in material development, micro-mechanical design and device engineering towards enabling novel flexible integrated photonic systems.

First, we pioneered a monolithic approach to realize flexible, high-index-contrast chalcogenide glass photonics with significantly improved processing throughput and yield. Noting that the conventional multilayer bending theory fails when laminates have large elastic mismatch, we derived a mechanical theory accounting for multiple neutral axes in one laminated structure to accurately predict its strain-optical coupling behavior. Through combining monolithic fabrication and local neutral axis designs, we fabricated devices that boast record optical performance (Q = 460,000) and excellent mechanical flexibility enabling repeated bending down to sub-millimeter radius without measurable performance degradation. The capabilities of these devices far surpass those of current ‘state-of-the-art’ designs. Moreover, we demonstrated that

our flexible glass device technology offers a simple, effective fabrication route for 3-D photonic structures including vertical-stack resonator filters, interlayer waveguide couplers, and woodpile photonic crystals.

Furthermore, we investigated TiO_2 as a material candidate for biocompatible and flexible integrated photonics. Amorphous TiO_2 films were deposited using a low temperature (< 250 °C) sol-gel process and exhibited a low optical loss of 3 dB/cm. Structural and optical properties of the films were systematically characterized. We also fabricated and tested TiO_2 optical waveguides and resonators monolithically integrated on flexible polymer substrates, measuring resonator quality factors as high as 20,000. Despite the inherent mechanical rigidity of the TiO_2 material, we experimentally demonstrated repeated folding down to a < 0.3 mm radius of devices fabricated with the developed multi-neutral-axis mechanical design without degrading their optical performance. Finally, we showed through in-vitro tests that the TiO_2 devices are cytocompatible. These results pave the way towards emerging applications of flexible photonics technology such as epidermal sensing, optical imaging, optogenetic modulation, and data communications.

Chapter 1

INTRODUCTION

1.1 Integrated Photonics

Photonics is the science and technology of generating, controlling, and detecting photons as electronics is the science of dealing with electrons. The emergence of novel photonic devices with the development of semiconductor fabrication technology, results in the appearance of some more complex devices such as lasers, detectors, modulators, showing the important connection between photonics and electronics [1].

The term "integrated photonics", first proposed in 1960 by Dr. Stewart E. Miller, refers to the fabrication and integration various passive and active components on a single planar substrate, combining and interconnecting them through optical transmission lines called waveguides. The basic idea is to use photons instead of electrons to create integrated optical circuits similar to those in conventional and well-established integrated micro-electronic circuits. Unlike conventional electronic circuits, in which the dominant device is the transistor, optical components designed for generation, focusing, splitting, coupling, isolation, polarization control, switching, modulation, filtering and light detection, should ideally be integrated in a single chip to achieve integrated photonic circuits. The creation of integrated photonic circuits requires the stringing together of individual "building blocks" of photonic elements in appropriate sequences [1]. These "building blocks" include passive components such as optical waveguide, micro-resonators, couplers and active elements such as lasers and

photodetectors. Here in this thesis we will focus on the integration of passive photonic devices on flexible substrate.

1.2 Flexible Photonic Materials and Devices

Realization of electronics and photonics with performance equal to current established technologies that use rigid semiconductor or glass materials, but in light-weight, bendable, foldable, stretchable or even compressible forms would enable many emerging applications [2, 3]. Examples include flexible aberration-free optical imaging [4], short-reach optical interconnects [5, 6], epidermal sensing [7, 8], photodetectors [9], solar cells [10-12], light emitting diodes [13-15], broadband photonic tuning [16], Fano reflectors [17], strain gauges [18] and so on. It has become a rapidly developing field in recent years at the forefront of photonics, especially for the integration of on-chip photonic devices on deformable polymer substrates (Figure 1.1).

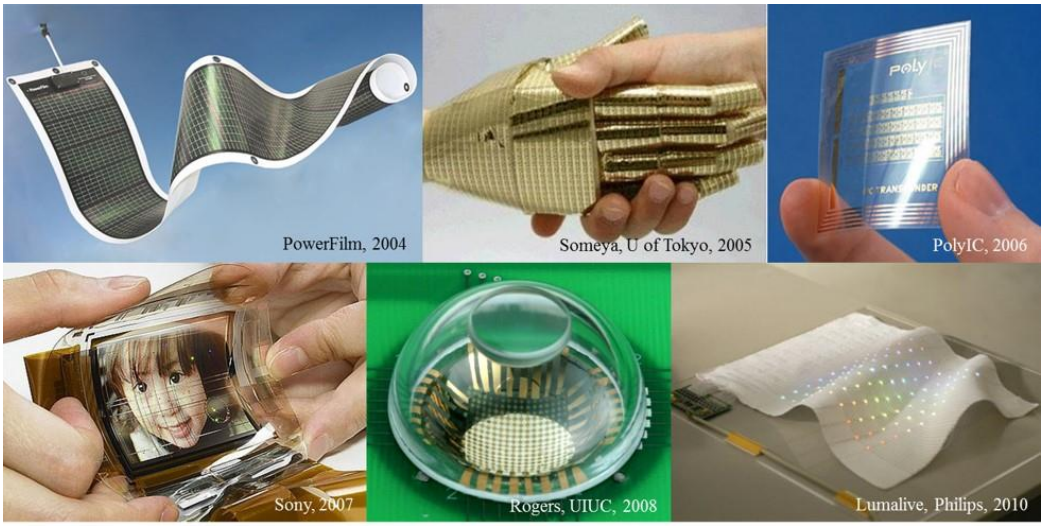

Figure 1.1 Different kinds of applications for electronics and photonics on flexible substrates

Organic polymers are generally considered the preferred materials for flexible photonic devices given their inherent mechanical flexibility and compatibility. Besides serving as the flexible substrate material, polymers are also used for waveguiding [19, 20], filtering [21, 22], light emission [23-25] and optical modulation [26]. However, polymers cannot possess the high refractive indices, which is very necessary for strong optical confinement. The high-density integration of photonic structures will also be more difficult to achieve considering the larger dimension of the devices due to the low index contrast between polymer core and polymer cladding. Besides polymers, new materials are progressively being introduced onto flexible platforms to offer new functionalities. Many of these materials are traditionally regarded as rigid or even brittle in their bulk form; however, free-standing nanomembranes made of the same materials can be tightly bent without cracking, since surface strain induced by bending is proportional to the membrane thickness. In particular, semiconductor NanoMembranes (NMs) present an attractive material platform for active photonic device integration on polymer substrates [9, 17, 23, 27-29]. Semiconductor NMs retain a single crystalline structure essential for efficient optoelectronic device operation. The small thickness of the NMs can provide a large mechanical flexibility in the devices that their bulk counterparts usually do not possess. This is also applied to other amorphous other amorphous glasses systems. Glassy materials keep offering many useful characteristics such as low cost, excellent transparency, high threshold to optical damage, a relatively wide interval of refractive indices to choose from, and last but not the least, the easiness of monolithic integration on different substrates, makes themselves more attractive candidates for the fabrication of flexible integrated photonic devices [30-32]. So in this

work we have focused on the use of glass materials to fabricate the devices on flexible substrates.

1.3 Overview of the Thesis

This thesis is divided into seven chapters.

In Chapter 1, we generally introduce the concept and history of integrated photonics as well as all kinds of materials that have been used to fabricate integrated photonic devices on flexible substrates.

In Chapter 2, we manifest three major challenges that still exist currently in the realization of flexible photonics with super mechanical and optical performance. The first one is the extreme mechanical flexibility; the second one is the capability for multilayer and active integration; the third one is possibility to be biocompatible for Bio-sensing application. Where there are challenges, there are opportunities. Chapter 3 to Chapter 6 will discuss how we develop new design and fabrication approach to overcome all those difficulties. Besides, two different fabrication approaches are also introduced in Chapter 2, and our choice of monolithic fabrication method is determined.

In Chapter 3, by using chalcogenide glass (ChG) materials, we describe a simple monolithic method to fabricate integrated photonic devices directly on flexible substrates. The optical and mechanical performance of the fabricated micro-disk resonators and passive waveguides has also been characterized and discussed in this Chapter.

In Chapter 4, a new multi-neutral axis mechanical design is established to explain the mechanism of the flexibility of the fabricated photonic devices. Both FEM simulation and analytical model are provided in this Chapter. Besides, we validate the

developed mechanical theory by demonstrating a series of strain-optical coupling experiments. Excellent agreement is shown between the theory and experimental results.

In Chapter 5, we demonstrate several 3-D integrated flexible photonic devices thanks to the excellent planarization capability of SU-8 on patterned ChG structures. This approach offers a facile and simple alternative for 3-D photonic structure fabrication to conventional methods involving ion implantation, wafer bonding, or pick-and-place nanomanipulation as well as the integration with active devices.

In Chapter 6, sol-gel TiO_2 photonic devices on flexible substrate have been presented. In spite of the mechanical and optical performance characterization, the cytocompatibility has also been studied to confirm that our simple monolithic fabrication approach, multi-neutral axis mechanical design and the use of TiO_2 provide a possible route to achieve flexible integrated biophotonic components.

In Chapter 7, we make a summary to all the worked mentioned in this Ph.D thesis. Some future application such as the waveguide integrated flexible photodetectors by using our developed approach is also introduced in this Chapter.

Chapter 2

CHALLENGES AND OPPORTUNITIES

2.1 Challenges and Opportunities for Flexible Photonics

However, there are still some challenges in the fabrication of integrated flexible photonic devices. In this thesis, the primary focus is to overcome all those challenges to realize the monolithic integration of two kinds of glasses materials on flexible substrates.

2.1.1 Mechanical Robustness

The first challenge is the mechanical robustness, which is the key attribute to characterize the flexibility of the devices. We have made a table to compare the smallest bending radius, bending cycles as well as the degradation of the device performance after bending among the current state-of-the-art flexible electronic and photonic devices, which is shown in Table 2.1. To the best of our knowledge, there has been no report on the fatigue analysis of flexible micro-electronic or micro-photonic devices that can sustain sub-millimetre bending. In order to make highly flexible photonics with superior performance, a unique mechanical design aiming to reduce the strain level in devices is extremely necessary besides using a small thickness of the semiconductor nanomembrane or glass materials.

Table 2.1 Summary of reported fatigue testing results of flexible micro-electronic and photonic devices.

Device type	Bending radius (mm)	Bending cycles	Performance metric	Percentage change after tests
OLED with transparent contacts [33]	10.5	1000	Electroluminesence intensity	50%
PDMS flat-panel solar cell concentrator [12]	20	1000	Efficiency	Insignificant
Flexible molecular-scale electronics [34]	5	1000	Decay coefficient	17%
Flexible a-IGZO TFT amplifier [35]	5	1000	Gain	Insignificant
Flexible grapheme based capacitor [36]	5	10000	Capacitance	3.5%
Flexible silicon thin film transistor [37]	3	2000	Threshold voltage	< 20%

The common strategy to make rigid materials flexible is to bring the devices to the so called “neutral plane”. When you bend a simple beam, there is always a tensile strain on the top surface and a compressive strain at the bottom surface. Right in the middle we have what's known as a “neutral plane” where strain vanishes. So if we place our device at the neutral plane, it will experience minimal strain despite the large mechanical deformation. This is a commonly design for flexible electronics. However, there is an important distinguish between flexible electronics and flexible photonics. For flexible electronics, there is no problem if you embed the devices deeply in the flexible substrates, but for photonics, we often want to have evanescent interaction of the light

with the external environment for biochemical sensing and evanescent optical coupling (Figure 2.1), which means you have to put devices right close to the surface. To achieve efficient optical coupling, current flexible photonic devices are placed on the surface of polymer substrates. As a consequence, the devices are subjected to large strains upon bending and exhibits only moderate flexibility with a bending radius typically no less than 5 mm [5, 9, 18]. This mechanical performance severely limits possible deployment degrees of freedom for devices of this type.

In this doctoral research work, we have developed a multi-neutral-axis design, which is implemented to render the structure highly mechanically flexible, enabling repeated bending of the devices down to sub-millimetre bending radius without measurable optical performance degradation. Chapter 4 will discuss this in detail.

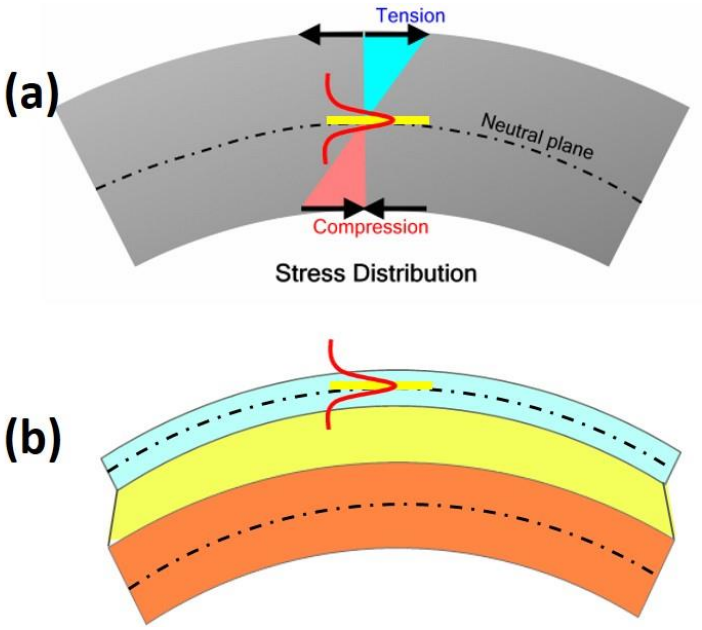

Figure 2.1 Pure bending of a (a) single layer for flexible electronic devices design and (b) multi-layer structure for flexible photonic devices design; the top and bottom surfaces undergo tensile and compressive strain, respectively. The neutral plane position is denoted by dashed line. Strain vanishes at the neutral plane, and thus maximum bending flexibility is achieved when the photonic devices are located at the plane. Here are multiple neutral planes in multi-layer structure design.

2.1.2 Multilayer and Active Integration Capability

The second challenge is the capability for multilayer and active integration of photonic devices on flexible substrates. Though there are some conventional techniques to fabricate 3-D multilayer devices such as wafer bonding [38], nano-manipulation [39], ion implantation [40], or multi-step chemical mechanical polishing (CMP) [41]; the fabrication yield cannot be promised considering the extreme complexity of the process.

The approach to be presented in this work, offers a simple and robust alternative route for novel 3-D photonic structure processing. Since our technology utilizes high-index chalcogenide glass materials as the backbone photonic materials, their amorphous

nature further enables us to scale the fabrication method to 3-D monolithic photonic integration on plastic substrates using multilayer deposition and patterning. The excellent planarization capability of ultra-thin resin ensures pattern fidelity in the multilayer process. In Chapter 5, we demonstrate the fabrication of several important device building blocks including broadband interlayer waveguide couplers, vertically coupled resonators, and woodpile photonic crystals using our approach. It is worth noting that all devices presented were fabricated using simple, low-cost UV contact lithography without resorting to fine-line patterning tools such as electron beam lithography or deep-UV lithography, and we expect significant device performance improvement through further optimization of processing steps.

Besides, our monolithic method also provide potential capability and simplicity for the integration with some active devices such as laser and photodetector, making it possible to fabricate a fully optical link platform on flexible substrate for application such as on-chip sensing and optical communication.

2.1.3 Potential for Bio-sensing [42]

Besides its well-established roles in communications and information technology, photonics is increasingly penetrating into other emerging application arenas, in particular, biotechnology and healthcare [43]. Integrated photonic devices are uniquely poised for in-vitro and in-vivo sensing, diagnostics, therapeutics, and stimulation functions given their small form factor, low power consumption, robustness, large multiplexing capacity, as well as strong light-molecule/tissue interactions enabled by tight optical confinement in these devices. Nevertheless, conventional photonic integration is based on rigid substrate platforms such as semiconductors or glass, and their mechanical stiffness makes the resulting devices inherently incompatible with soft

biological tissues. For instance, the large elastic mismatch between optogenetic neural probes and the brain tissue contributes to undesired tissue reactions such as glial scarring and tissue encapsulation [44]. Conformal sensor integration on human skin serves as another example where device mechanical flexibility becomes indispensable. In addition to mechanical stiffness, the presence of residual chemicals used in the photonic device processing, which may be toxic, can present another potential barrier towards biophotonic applications [45].

Traditional solutions to the aforementioned challenges entail exclusively using compliant, biocompatible organic polymeric materials for photonic device fabrication. A few examples of such materials include silk fibroin, gelatin, and agarose hydrogel [46-48]. The limited material selections and the low index contrast available in organic systems, however, pose severe constraints on the photonic functionalities that can be attained in these materials. Hybrid inorganic-organic photonics, exemplified by nanomembrane-based devices [9, 17, 27, 49-51], offers a preferred solution for flexible photonic integration given the diverse repertoire of photonic components already demonstrated based on these systems. However, the biocompatibility of the constituent materials and residual chemicals used in processing these hybrid photonic devices, despite its critical importance to many *in-vitro* and *in-vivo* applications, has rarely been addressed [52-54].

In this thesis, we investigate amorphous TiO_2 thin films deposited using a low-temperature sol-gel process as a new material for integrated biophotonic components in Chapter 6.

2.2 Fabrication Approaches

The requirement of mechanical flexibility poses unique constraints on the material processing and mechanical engineering of flexible photonic devices in addition

to their optical design considerations. To date, most flexible photonic components are fabricated either using transfer printing or direct monolithic patterning. In this section, we will first discuss the two processing routes.

2.2.1 Transfer Printing of Semiconductor Nanomembrane Structures and Devices [32]

Transfer printing, alternatively termed stamp printing, has several variants but all of them involve release of the functional layers (e.g. crystalline semiconductor NMs) or structures (e.g. fabricated devices) from the starting substrate, and transfer of the functional layers or structures onto a foreign flexible substrate. Figure 2.2 shows a general transfer printing process flow. The source material (e.g., SOI, GeOI, III-V multi layers with a sacrificial layer) is first being patterned into membrane (or strip forms) down to the sacrificial layer (Figure 2.2a-b). Top membrane layers are then released by undercutting the sacrificial layer (Figure 2.2c), with fully released membrane settles down on the handling substrate via van der Waals force (Figure 2.2d) (note: this in-place bonding case only applies to thin sacrificial layers. The wet etch step either completely releases the devices, which subsequently settle down and are weakly bonded to the silicon substrate via van der Waals force, or partially undercut the supporting oxide layer beneath the devices to form pedestal structures. The latter method prevents lateral shift of devices during the wet etch process [16, 55]. Finally membrane transfer process can take place with either a *direct flip transfer* or *stamp-assisted transfer* processes (Figure 2.2e-f). In the *direct flip transfer* process, an adhesion layer is applied on the host (foreign) substrate first. The membrane to be transferred can be picked up by the host substrate directly to complete the transfer. The adhesion layer (e.g., glue) can be dissolved afterwards, if needed. In the *stamp-assisted transfer* process, a stamp

(e.g., PDMS) was used to press toward the handling substrate, and lift-up the membrane to be transferred. Then the membrane attached to the stamp was picked up and attached to a new host substrate, which can be coated with glue, if needed. Slowly peeling off the stamp or removing the stamp with shear force, the NM can be left on the new host substrate [56].

By releasing high-quality flexible materials from SOI and other source substrates and transfer-printing them to a new host substrate, integration of dissimilar material systems becomes feasible on both rigid and flexible substrates, with individually optimized material structures, energy-efficient and flexible integration process, and intelligent functions. The transfer-printing steps can also be repeated to produce stacked multi-layer photonic structures [50]. Besides Si [57], many materials including III-V semiconductors [9, 58], metals [59], and organic semiconductors [60] are all amenable to transfer printing processing.

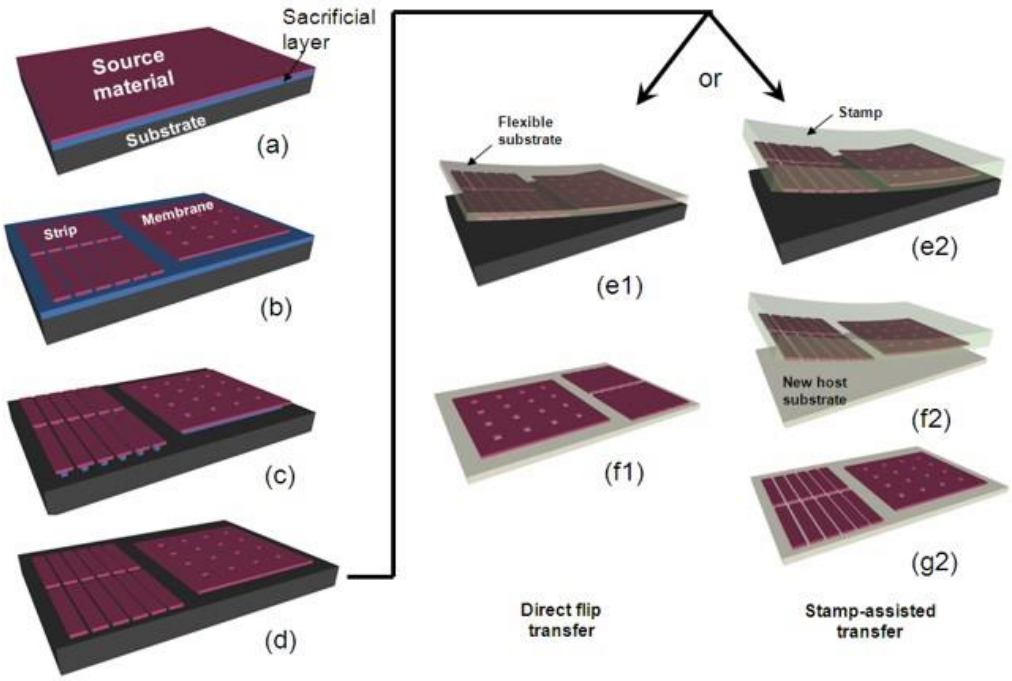

Figure 2.2 General process illustration for crystalline semiconductor membrane release, transfer and stacking. (a) Begin with source material (e.g., SOI, GeOI, III-V multi layers with a sacrificial layer). Metallization can be applied here, if needed. (b) Pattern top layer into membrane (or strip forms) down to the sacrificial layer. (c) Release membrane by undercutting the sacrificial layer. (d) Fully released membrane settles down on the handling substrate via van der Waals force ("in-place bonding"). Direct flip transfer: (e1). Apply glue on host (e.g., flexible) substrate and attach it to the handling substrate. (f1) Lift-up the host substrate and flip to complete the transfer. Glue can be dissolved if needed. Stamp-assisted transfer: (e2) Bring a stamp (e.g., Polydimethylsiloxane, or PDMS) toward the handling substrate, press and lift-up. (f2) Apply the stamp with membrane attached to a new host substrate (which can be coated with glue, but not necessary). (g2) Slowly peel off the stamp or remove the stamp with shear force, leaving the membrane to stay on the new host substrate. Multiple layers can be applied by repeating (a)-(f1) or (a)-(g2).

Based on transfer printed NMs on flexible substrates, various high performance photonic and optoelectronic devices have been demonstrated, including flexible

photodetectors, LEDs, and solar cells, flexible Si Fano resonance filters, and mostly significantly, fast flexible electronics, with record speed of RF performances, owing to high electron mobility in single crystalline semiconductors [61-66]. Many excellent results have also been reported by Lagally *et al*. [61, 67] and Rogers *et al*. [27, 68, 69] on the unique electronic, photonic, and thermoelectronic, and mechanical properties associated with this new class of inorganic flexible semiconductor membrane material system. To improve the yield of the printing transfer process, Xu *et al.* reported an innovative stamp printing technique with an adhesion controllable suspended configuration [49]. To address the alignment challenge over the large area flexible substrate, a local alignment scheme in combination with more accurate Si-NM transfer measures for minimizing alignment errors was reported [65]. Recently, based on the strained Si/SiGe/Si-NMs transferred onto flexible substrates, another record was set for fast flexible transistors, with maximum oscillation frequency of 15 GHz demonstrated [64]. These results indicate the great potential of properly processed Si-NMs for high-performance flexible optoelectronics [66].

2.2.2 Monolithic Integration on Plastic Substrates [32]

Compared to the hybrid transfer printing approach, direct monolithic patterning of passive photonic devices on flexible substrates offers a much simplified alternative with improved yield, large-area patterning capability, and potential compatibility with roll-to-roll processing. The typical process flow of monolithic photonic device fabrication on plastic substrates is schematically illustrated in Figure 3.1 and Figure 5.1. The flexible polymer substrate is first attached to a rigid handler substrate to facilitate handling in subsequent processing steps, followed by deposition of the thin film device layer via Physical Vapor Deposition (PVD), Chemical Vapor Deposition (CVD), or

solution processing (spin-coating and dip-coating). It is critical to ensure the flatness and low roughness of the substrate and film surfaces, since surface height variation can lead to defocus and image distortion during projection lithography, or stitching error during electron beam lithography. Patterning of the thin film into functional photonic structures is accomplished through plasma etching (note that the RF power should be kept low to reduce plasma damage to the polymer substrate [18]), lift-off [70], nanoimprint [71], or nanostencil lithography [72]. The monolithic fabrication route has been applied to create optical waveguides, resonators, gratings, and plasmonic nanostructures on flexible substrates.

In this work, we demonstrate monolithic photonic integration on plastic substrates using high-refractive-index chalcogenide glass (ChG) materials. This process yields high-index-contrast photonic devices with record optical performance and benefits significantly from improved processing protocols based on simple, low-cost contact lithography. We show that this versatile process can be readily adapted to different glass compositions with tailored optical properties to meet different candidate applications. More details about the developed monolithic integration approach are discussed in Chapter 3.2.

2.3 Summary

In this chapter we have discussed the three major challenges that may influence the development of flexible photonics with super mechanical and optical performance: mechanical flexibility, multilayer and active integration capability and cytocompatibility. General introduction of the related strategies and fabrication methods we took has also been provided here.

Chapter 3

FLEXIBLE CHALCOGENIDE GLASS PHOTONIC DEVICES

3.1 Chalcogenide Glass Materials

Chalcogenide glasses (ChGs) are amorphous semiconductor compounds of one or multiple chalcogens elements from Group VI of the periodic table, namely, sulfur (S), selenium (Se) or tellurium (Te). While oxygen (O), strictly speaking, is also a chalcogen, oxide materials are usually treated separately since they have been known well and studied for a long time. Although polonium (Po) is also chemically a chalcogenide, it is not used in chalcogenide glasses due to its strong radioactivity and high price. Usually chalcogenide glasses contain glass formers such as arsenic (As), antimony (Sb), germanium (Ge) and/or gallium (Ga) so that their optical and thermomechanical properties can be tuned. These glasses materials have relatively high refractive index ranging from 2 to 3 depending on different composition of the elements, which allows strong optical confinement of passive devices such as waveguides and resonators to be integrated compactly in a large scale [73]. That is to say, the higher the index contrast, the larger the number of function per chip would be. This is an extremely important factor of quality because it reduces the number of separate chips, interconnections, pigtailing, packaging and costs [74].

Another good attribute of chalcogenide glasses is the broad infrared transparency window. They are low-phonon-energy materials. Sulfide-based glasses typically transmit light up to 12 μm, selenides to 16 μm, and tellurides to 20 μm. The large IR transparency windows overlap with the spectral vibrational spectrum of most

organics chemicals and biomolecules, making chalcogenide glasses attractive candidate in sensing applications [73].

Besides, chalcogenide glasses can be monolithically integrated on different substrates including polymers thanks to their amorphous structure and low thermal deposition temperature (substrate temperature close to room temperature). This versatility is particularly advantageous for monolithic and hybrid integration with different functional comments such as not only passive structures (waveguides, resonators…), but also some active devices (light sources, detectors…).

On the whole, we choose chalcogenide glasses to fabricate photonic devices on flexible substrates for the following three reasons:

1) Low substrate temperature during the thermal deposition;
2) Broad IR transparency window;
3) Large index tuning range.

3.2 Fabrication Methods of Flexible Chalcogenide Glass Photonic Devices [70]

Using chalcogenide glasses to fabricate photonic devices requires good-quality thin films before any device patterns can be transferred. There are several common methods such as thermal evaporation [75, 76], sputtering [77], pulsed laser deposition [75, 77] and solution processing techniques [78, 79]. Solution processing has recently emerged as a promising technique for low-cost, large-area chalcogenide glass film deposition. It can be combined with soft lithography such as micro-molding in capillaries [80] and nanoimprint [79] for photonic device fabrication. But still, the solvent residue in glass thin films will always be a problem, which lead to additional absorption loss of the photonic devices.

In this thesis work, we choose thermal evaporation approach to fabricate the flexible integrated photonic devices considering that high temperature and plasma would bring some damage to the polymer substrates. Lift-off method is adopted to fabricate various photonic structures on flexible substrates from the evaporated thin films.

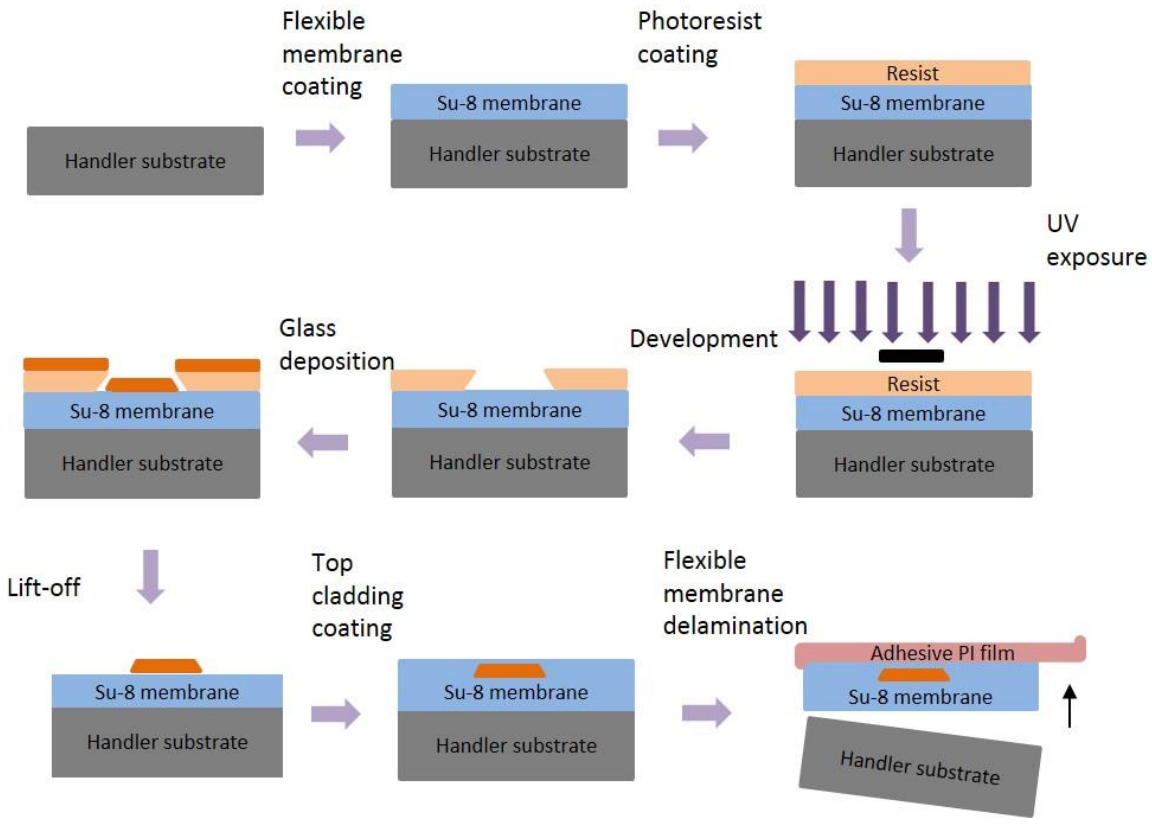

Figure 3.1 Schematic overview of the monolithic flexible photonic device fabrication process using lift-off method.

Lift-off method is a method of creating structures of a target material on the surface of a substrate using a sacrificial material such as photoresist. There are four steps:

1) preparing substrates; 2) creating inverse patterns using photolithography; 3) depositing target material; 4) removing the rest of photoresist covered by the target material. It is a versatile, low temperature process which is not limited to specific glass compositions and substrates [76].

Figure 3.1 shows the fabrication flow how we make the photonic devices on flexible substrates using lift-off method. First, an SU-8 epoxy layer was spin coated on the handler wafer. SU-8 epoxy was used as the cladding polymer given its proven chemical stability, excellent optical transparency, and superior planarization capacity. Prior to UV exposure, SU-8 epoxy behaves as a thermoplastic polymer amenable to thermal reflow treatments to create a smooth surface finish even on substrates with multi-level patterned structures; after thermal or UV cross-linking, the epoxy becomes a thermosetting resin and is robust against mechanical deformation, humidity, and subsequent thermal processing. Capitalizing on this unique property of SU-8, we developed an ultra-thin epoxy planarization process with a high degree of planarization (DOP) critical to 3-D photonic integration. Details of the planarization process are described in Chapter 5. Then a negative photoresist (NR9-1000PY, Futurrex Inc.) pattern was lithographically defined on the SU-8 layer using contact lithography on an ABM Mask Aligner. Chalcogenide glass films were thermally evaporated onto the substrates from bulk glasses synthesized using a melt-quenching technique. The deposition was performed using a custom-designed system (PVD Products, Inc.). The deposition rate was monitored real-time using a quartz crystal micro-balance and was stabilized at 20 Å/s. After the deposition, the sample was sonicated in acetone to dissolve the resist layer, leaving a glass pattern reverse to that of the photoresist. Top cladding layer will then be coated on the sample surface to protect the device structure.

Lastly, the whole photonic structure embedded in SU-8 layer shall be delaminated from the handler substrate using adhesive Kapton tape to form free-standing flexible structures. The Kapton tape consists of two layers, a silicone adhesive layer and a polyimide substrate, and it serves dual purposes: firstly, it facilitates the delamination process; and secondly, the low-modulus silicone adhesive serves as an effective strain-relieving agent in our local-neutral-axis design to be discussed later. Figure 3.3a shows a photo of a final free-standing flexible photonic circuit chip. Good-quality micro-disk resonators have been fabricated using this approach. Their mechanical and optical performance was characterized and would be discussed in Chapter 4.

However, lift-off method still has some shortages to fabricate resonators with extreme high Quality-factor. The first biggest reason is the limitation of photolithography. If the lithography recipe including exposure dose, baking time and temperature, development conduction is not optimized, it will be challenging to transfer patterns with smooth edge from the photomask (Figure. 3.2a). Though you can obtain "perfect" recipe, line edge roughness still cannot be avoided since it is caused by a number of statistically fluctuating effects at those small dimensions such as shot noise (photon flux variations), statistical distributions of chemical species in the resist such as photoacid generators, the random walk nature of acid diffusion during chemical amplification, and the nonzero size of resist polymers being dissolved during development. It is unclear which process or processes dominate in their contribution to line edge roughness [81]. Besides, a "perfect" recipe is not suitable for the lift-off process since sufficient resist under-cut is very necessary to obtain structures with smooth side wall as shown in Figure 3.2b-f. In fact, structures patterned by a little bit under-exposed negative resist with large thickness will work better. Or additional glass

materials would adhere to the edge of the resist and finally remain as the source of the side wall scattering loss (Figure 3.2d). And Figure 3.2e-f shows one example of the cross-section and top surface images of a good lift-off waveguide.

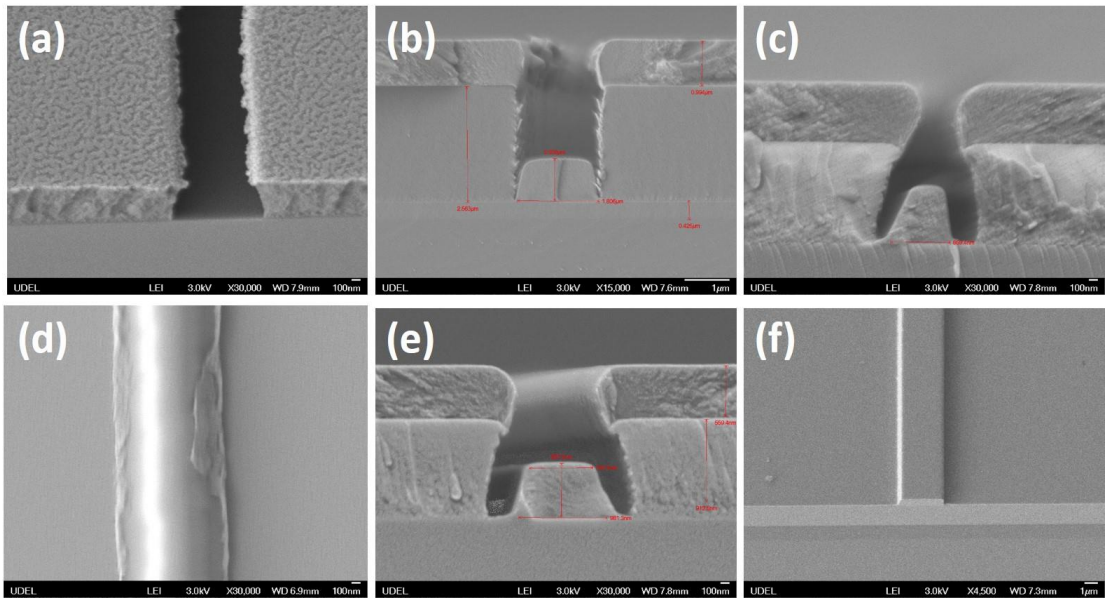

Figure 3.2 SEM images of the device pattern at different steps of the lift-off process. (a) A bad example of the pattern after photolithography; (b) Small negative resist under-cut for the lift-off process; (c) An example indicating the evaporation is a line-of-sight technique; (d) Surface image of a lift-off waveguide from the small resist under-cut pattern; (e) Cross-section image of a good lift-off sample with sufficient under-cut and vertical evaporation of glasses towards the substrate; (f) Surface image of the waveguide from a good lift-off sample.

Our best flexible micro-disk resonator device shown in Figure 3.3a obtained by lift-off method exhibited an intrinsic Quality-factor as high as 460,000, the highest value ever reported in photonic devices on plastic substrates. We have also tested the fabrication process with several different Chalcogenide glass compositions with vastly

different optical properties (indices and Tauc optical band gaps) to demonstrate the process' material compatibility: Figure 3.3b shows University of Delaware logos patterned on flexible substrates made of three glass compositions: $Ge_{23}Sb_7S_{70}$ (n = 2.1, Eg = 2.2 eV), As_2Se_3 (n = 2.8, Eg = 1.8 eV) and As_2S_3 (n = 2.4, Eg = 2.1 eV), all of which exhibit good adhesion to the SU-8 substrate. Figure 3.3c shows a microscopic image of a 30 µm-radius and 450 nm-thick $Ge_{23}Sb_7S_{70}$ micro-disk resonator pulley coupled to a 800 nm wide channel bus waveguide.

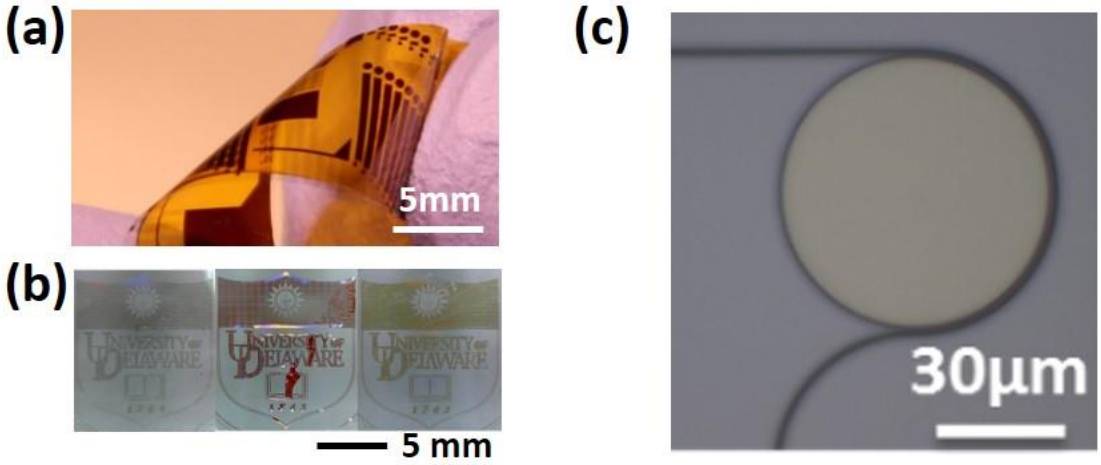

Figure 3.3 Flexible ChG photonic devices. (a) Photo of a flexible photonic chip showing a linear array of micro-disk resonators; (b) University of Delaware logo on PDMS flexible substrates made of Ge23Sb7S70, As2Se3 and As2S3 glasses (from left to right); (c) Optical image of the fabricated micro-disk resonator on flexible substrate.

3.3 Optical Performance Characterization of the Flexible Chalcogenide Glass Photonic Devices [70]

3.3.1 Optical Transmission Measurement Setup

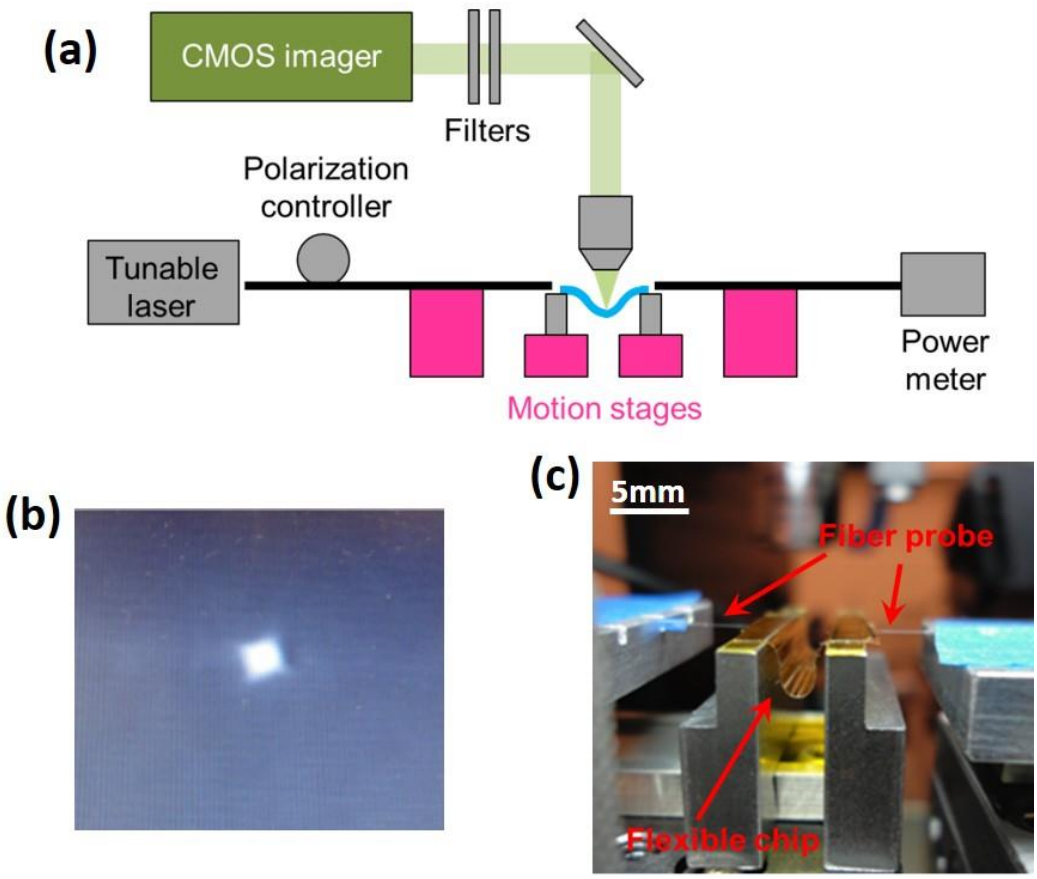

Figure 3.4 (a) Schematic diagram of the testing setup; (b) Far-field image of TE guided mode output from a single-mode flexible Ge23Sb7S70 glass waveguide; (c) Photo of a flexible waveguide chip under bending test: an imaging processing software was used to extract the bending radius of the chip from the image.

Figure 3.4a schematically illustrates the optical transmission measurement setup used to characterize the photonic devices. Tapered lens-tip fibres were used to couple

light from an external cavity tuneable laser (Agilent 81682A) into and out of the waveguides through end facets formed by cleaving the samples prior to delamination from the Si handler substrates. To facilitate optical coupling into the single-mode waveguides, the 0.8 μm wide bus waveguides are tapered to a width of 2 μm near their end facets. The fibre-to-waveguide coupling loss is not optimized in this work and is estimated to be approximately 4 dB per facet. Figure 3.4b shows a far-field image of quasi-TE guided mode output from a single-mode $Ge_{23}Sb_7S_{70}$ glass waveguide on a plastic substrate and Fiure 3.4c shows a photo of a flexible chip under bending test. The chip was glued onto the linear motion sample stages using double-sided sticky tapes. Bending radius of the flexible chip was measured from the image using an imaging processing software (Image J).

3.3.2 Optical Performance Characterization in $Ge_{23}Sb_7S_{70}$ Glass Micro-disk Resonators Fabricated on Flexible Substrates

3.3.2.1 Quality Factor

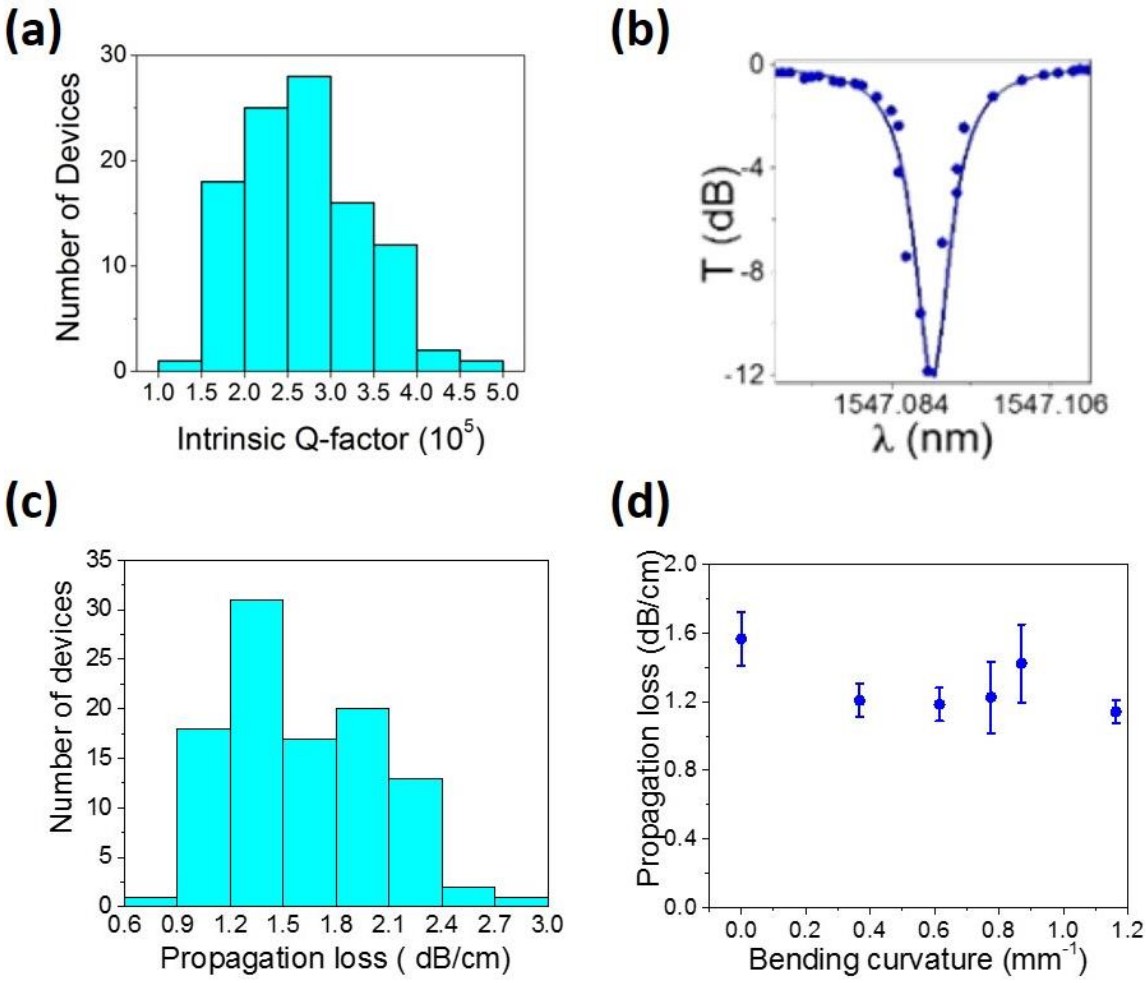

Figure 3.5 Q-factor and loss of the flexible resonators. (a) Intrinsic Q-factor distribution measured in flexible micro-disk resonators; (b) An example of the resonator transmission spectrum; (c) Optical loss distribution measured in flexible micro-disk resonators; (d) Optical loss in a flexible resonator as a function of bending radius measured when the device was in the mechanically deformed state.

Using the optical measurement setup, we have tested over 100 resonator devices randomly selected from samples fabricated in several different batches, and all of them operate as designed after going through the entire fabrication process. Figure 3.5a plots the intrinsic Q-factor distribution of the devices measured near 1550 nm wavelength, showing an average Q-factor of $(2.7 \pm 0.7) \times 10^{5.}$ A normalized resonator transmission spectrum is shown in Figure 3.5b as an example: our best device exhibited an intrinsic Q-factor as high as 460,000, the highest value ever reported in photonic devices on plastic substrates.

3.3.2.2 Propagation Loss

Since the flexible substrates are not amenable to cleavage, it is difficult to use the cut-back method to measure waveguide propagating loss. The non-planar nature of the devices also makes scattered light streak imaging unreliable. Therefore, we choose to evaluate the propagation loss in the flexible photonic devices using optical resonator measurements. The linear propagation loss α in a traveling-wave optical resonator is related to its intrinsic Q-factor Q_{in} through:

$$\alpha = 2\pi n_g / Q_{in}\lambda \qquad (3.1)$$

where n_g denotes the group index of the resonant mode and λ is the resonant wavelength. The intrinsic quality factor can be deduced from the loaded Q-factor and resonant peak extinction ratio following protocols outlined in literature [82]. This method is particular suitable for flexible device characterization as it directly probes the modal attenuation in resonators and does not require reproducible facet quality. It is worth noting that since we used micro-disk resonators in our experiments, the loss figures cited in this section refer to the linear propagation loss of micro-disk modes.

The statistical distribution of propagation loss in the resonator devices we measured is presented in Figure 3.5c (calculated from Figure 3.5a). The average loss is (1.6 ± 0.4) dB/cm. Our prior measurement showed that the intrinsic material loss in thermally evaporated $Ge_{23}Sb_7S_{70}$ films was well below 0.5 dB/cm[76], and thus sidewall roughness scattering is the primary loss mechanism in our devices.

3.3.2.3 Impact of Bending

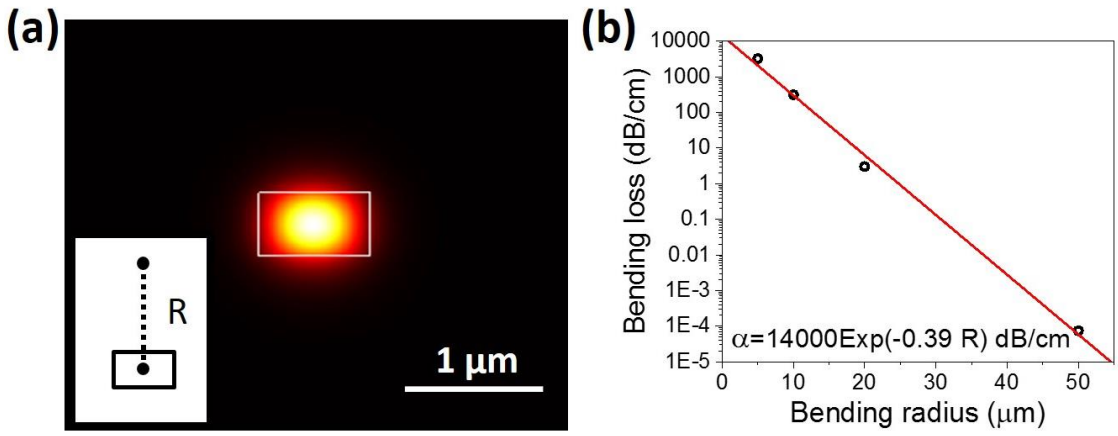

Figure 3.6 Bending loss simulations. (a) Quasi-TE mode intensity profile for a 0.8 μm × 0.45 μm waveguide with a bending radius of 500 μm; the inset illustrates the waveguide bending direction in our mechanical tests; (b) Radiative bending losses at different bending radii fitted to an exponential model.

We further note that optical loss in the devices is largely independent of the bending radius when they are mechanically deformed: as an example, Figure 3.5d plots the propagation loss in a flexible resonator measured when the device was bent. The change imparted by the bending deformation is insignificant considering the measurement error. This observation can be readily explained by the tight optical

confinement in our high-index-contrast photonic devices, which effectively suppresses radiative loss in bent guided wave structures. Figure 3.6a shows the quasi-TE mode radiative loss due to bending in a $Ge_{23}Sb_7S_{70}$ waveguide of 800 nm width and 450 nm height, simulated using the full-vectorial waveguide mode solver package FIMMWAVE (Photon Design). It is apparent that radiative bending loss remains negligible down to 50 μm radius (Figure 3.6b). Therefore, it is anticipated that no radiative loss was experimentally observed when we mechanically deform our flexible chip.

3.4 Fatigue Test of the Flexible Chalcogenide Glass Photonic Devices [70]

Fatigue tests of flexible electronic or optoelectronic devices evaluate the mechanical durability of the devices as they undergo repetitive bending for a large number (> 1,000) of cycles. Figure 3.7a shows the experimental setup we used for the fatigue test. Two edges of a flexible chip were attached to two sample holders, and the holders were mounted on a sliding track. Linear translational motion of the holders thus resulted in bending of the chip. To reproducibly control the bending radius, metal chucks of different thicknesses were glued to one of the holders as spacers to define the translational distance and hence bending radius. Optical transmission spectra of the same waveguides and resonators were repeatedly measured in a "flat" state of the chip using fiber end-fire coupling before and after multiple bending cycles at 0.8 mm bending radius.

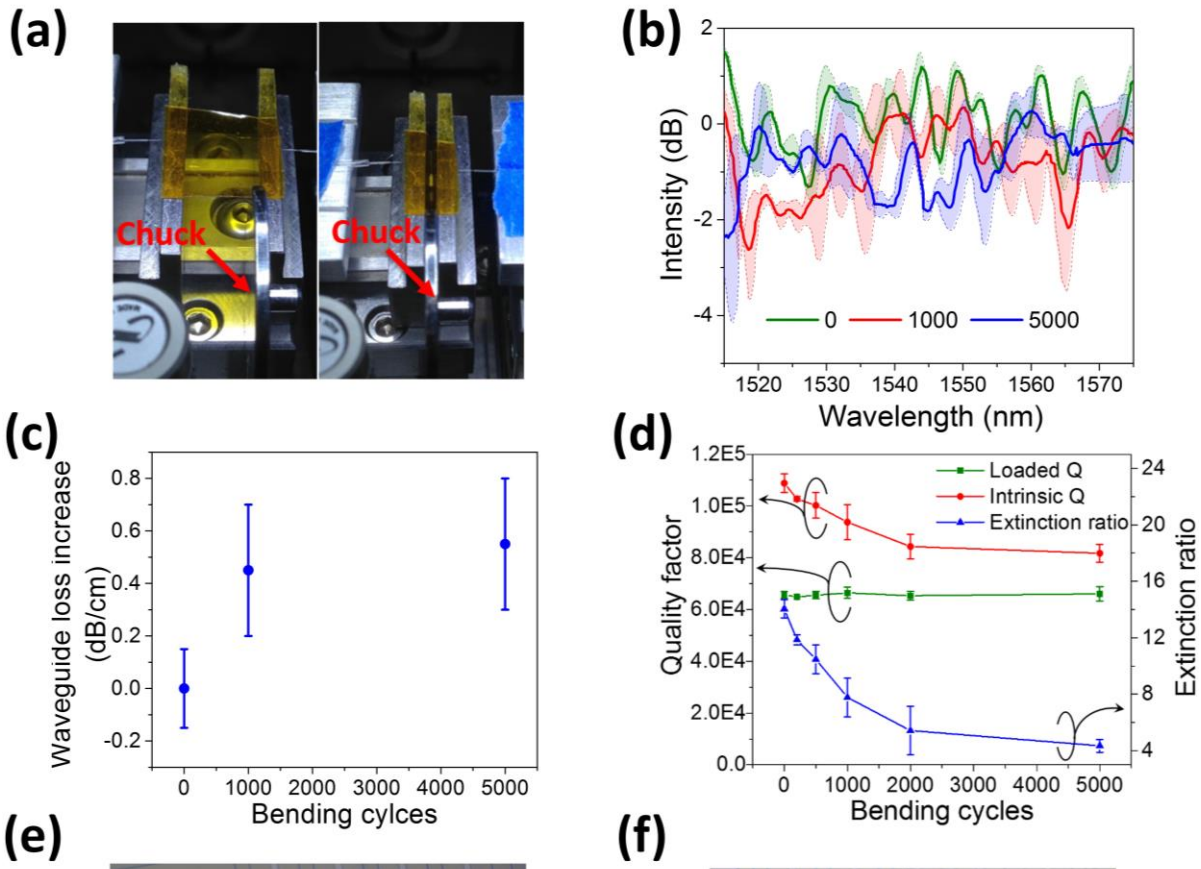
(a)
Chuck
Chuck
(b)
Intensity (dB)
2
0
-2
-4
0
1000
5000
1520
1530
1540
1550
1560
1570
Wavelength (nm)
(c)
Waveguide loss increase (dB/cm)
0.8
0.6
0.4
0.2
0.0
-0.2
0
1000
2000
3000
4000
5000
Bending cylces
(d)
Quality factor
1.2E5
1.0E5
8.0E4
6.0E4
4.0E4
2.0E4
0.0
Loaded Q
Intrinsic Q
Extinction ratio
24
20
16
12
8
4
Extinction ratio
0
1000
2000
3000
4000
5000
Bending cycles
(e)
30 µm
200 µm
(f)
30 µm
200 µm

Figure 3.7 Fatigue test of the flexible photonic chip. (a) Photos of the fatigue testing setup. The red arrow points to the metal chuck spacer; (b) Normalized optical transmission spectra of a flexible waveguide after multiple bending cycles at 0.8 mm bending radius. The shaded regions denote the measurement error bar at different wavelength, which was defined as the standard deviation of optical transmittance collected in multiple transmission measurements for the same devices; (c) Spectrum-averaged (1510-1580 nm wavelengths) waveguide propagation loss change due to repeated bending cycles; error bar origins from the same device for multiple tests; (d) Loaded Q-factors, intrinsic Q-factors and extinction ratios of a flexible Ge23Sb7S70 micro-disk resonator after multiple bending cycles at 0.8 mm bending radius; error bar origins from the same device for multiple test; (e) Top-view optical microscope image of flexible resonators prior to the fatigue test; (f) Optical microscope image of the same set of resonators after 5,000 bending cycles at 0.8 mm bending radius, revealing structural integrity of the devices free of cracks. The scattered spots are dust particles deposited on the chip surface during the mechanical tests, which were carried out in a non-cleanroom environment.

Figure 3.7b plots the insertion loss of a flexible $Ge_{23}Sb_7S_{70}$ waveguide before and after up to 5,000 bending cycles: the same waveguide was used throughout the measurement to ensure consistent facet quality. The intensity fluctuations were partially attributed to excitation of higher order modes at the 2 μm wide input/output waveguide taper sections. The changes of waveguide propagation loss deduced from the measurement were plotted in Figure 3.7c. The results indicate a (0.5 ± 0.3) dB/cm waveguide loss increase after 5,000 cycles at a frequency of 1.5 Hz. The same fatigue tests were performed on $Ge_{23}Sb_7S_{70}$ micro-disk resonators. After 5,000 bending cycles, we observed a 23% decrease of the device intrinsic Q-factor (Figure 3.7d). We inspected the flexible chip under optical microscope (up to 50x magnification) before and after 5,000 bending cycles and no micro-cracks were observed across the chip (Figure 3.7e-f). Therefore, we conclude that the loss increase (~ 0.5 dB/cm) likely stems from layer delamination or sub-micron cracks that cannot be resolved with an optical microscope,

although further study is required to elucidate the loss mechanism. The superior mechanical durability of our devices can be seen from a comparison with state-of-the-art flexible electronic devices shown in Table 3.1. To the best of our knowledge, our study also represents the first report of fatigue analysis on flexible micro-electronic or micro-photonic devices that can sustain sub-millimeter bending.

Table 3.1 Comparison of reported fatigue testing results of flexible micro-electronic and photonic devices with that of our fabricated devices.

Device type	Bending radius (mm)	Bending cycles	Performance metric	Percentage change after tests
Chalcogenide glass resonator (this report)	0.8	5000	Quality factor	23%
OLED with transparent contacts[33]	10.5	1000	Electroluminesence intensity	50%
PDMS flat-panel solar cell concentrator[12]	20	1000	Efficiency	Insignificant
Flexible molecular-scale electronics[34]	5	1000	Decay coefficient	17%
Flexible a-IGZO TFT amplifier[35]	5	1000	Gain	Insignificant
Flexible grapheme based capacitor[36]	5	10000	Capacitance	3.5%
Flexible silicon thin film transistor[37]	3	2000	Threshold voltage	< 20%

3.5 Summary

As a summary for this chapter, we pioneered a monolithic approach to realize flexible, high-index-contrast glass photonics with significantly improved processing throughput and yield. Using this approach, we demonstrate the first flexible glass photonic chip integrated with planar waveguide-coupled micro-disk resonators made of Ge-Sb-S chalcogenide glass. The resonators feature a high intrinsic quality factor (Q) of 4.6×10^5 at the 1550 nm telecommunication band, an order of magnitude higher than previous reports on flexible substrates. Our in-situ measurements show that the flexible chip can be readily bent down to sub-millimeter radius without adversely affecting the optical performance of devices.

Chapter 4

MULTI-NEUTRAL-AXIS MECHANICAL DESIGN AND STRAIN-OPTICAL COUPLING

4.1 Mechanical Design for Flexible Photonic Devices [32, 70]

So what kind of mechanical design strategy we should use to fabricate photonic devices to be such flexible against mechanical bending. The basic design idea to improve flexibility is to minimize the strain of the photonic device layer at a given mechanical deformation configuration. This is particularly important for photonic devices made of rigid materials such as glasses.

4.1.1 Classical Simple Bending Theory

In the case of simple bending, strain minimization can be attained by adopting the so-called "neutral plane" configuration (Figure 4.1a). At the neutral plane, the strain vanishes. Therefore, positioning thin film photonic devices at the neutral plane inside a multi-layer stack minimizes their strains during bending. For a multi-layer stack with the 1st layer on top and the nth layer at the bottom, cross-sectional planes before bending are assumed to remain planar after bending in the classical bending theory. Under this assumption, the neutral plane position from the top surface is given by:

$$b = \frac{\sum_{i=1}^{n} \bar{E}_i d_i \left(\sum_{j=1}^{i} d_j - \frac{d_i}{2} \right)}{\sum_{i=1}^{n} \bar{E}_i d_i} \qquad (4.1)$$

where $\overline{E}_i = E_i/\left(1-\nu_i^2\right)$ represents the plane strain Young's modulus with ν_i being the Poisson's ratio, and d_i is thickness of the i[th] layer, respectively. The equation assumes linear mechanics, pure bending, and no-slip boundaries between the layers, which suggests zero shear deformation in the layers [83]. These assumptions are usually valid in the case of small bending (bending radius $r \gg \sum_{i=1}^{n} d_i$). Based on the simple bending theory, elastic strain in the stack linearly increases with the distance away from the neutral plane. Bending-induced tensile strain can be calculated analytically using:

$$\varepsilon = \frac{y}{\rho} \quad (4.2)$$

where y is the distance from the point of interest to the neutral axis and ρ represents the radius of the neutral axis. Elastic strain in the stack linearly increases with the distance away from the neutral plane. As a result, nanomembrane devices with an ultra-thin layout contribute to significantly reduced strain when they are strategically positioned at the neutral plane location.

According to Equation 4.1, the neutral plane design requires the photonic elements to be embedded inside the multi-layer structure. While such a configuration is generally compatible with electronic circuits, it may not meet the fabrication requirements or application needs of integrated photonics. For example, encapsulating the photonic components deep underneath a thick top cladding layer prohibits evanescent wave interactions with the external environment which is essential for chem-bio sensing and evanescent optical coupling.

One solution to this challenge is to fabricate photonic devices on the top surface of a relatively thin (< 50 μm) flexible substrate with low elastic modulus, which reduces the strain level in the device layer according to the multi-layer bending theory despite that the device layer is not aligned with the neutral plane [83]. This approach has been

most frequently implemented in conjunction with transfer printing of semiconductor NMs [9, 17, 58] and typically allows bending with > 10 mm radius.

4.1.2 Multi-neutral Axis Mechanical Design

Another solution is to make a new mechanical design to shift neutral plane from the center of bending beam to the surface of the substrate. This is the reason why we would like to develop a multi-neutral axis mechanical design so that one of the neutral plane would be close to the substrate surface. It is worth noting that Equation 4.1 may become invalid due to the elastic modulus mismatch between layers in the case of large bending (i.e. small bending radius). For example, when an elastomer layer with low Young's modulus (~ MPa) is sandwiched between two glassy polymer layers with much higher moduli (~ GPa), large shear deformation takes place in the elastomer layer to minimize elastic deformation energy in the two rigid glassy polymer layers, similar to the strain decoupling effect discussed in the tension case [84]. The large modulus mismatch here makes the classic bending theory fail in our case. Figure 4.1b illustrates such an example where a 50 μm thick silicone elastomer layer (E = 2 MPa) is sandwiched between two polyimide (PI) layers (E = 2.5 GPa) of 10 μm thickness each to form a tri-layer structure. When bent, the silicone layer practically decouples the in-plane strain in the two PI layers and serves as an effective strain relieving agent which reduces the strain in on the multi-layer stack surface by a factor of 6 compared to that in a single PI layer of the same thickness (Figure 4.1b). We have employed this mechanical design to demonstrate highly flexible (minimum bending radius < 0.5 mm) photonic devices made of chalcogenide glasses, despite the poor mechanical strength of the glass materials.

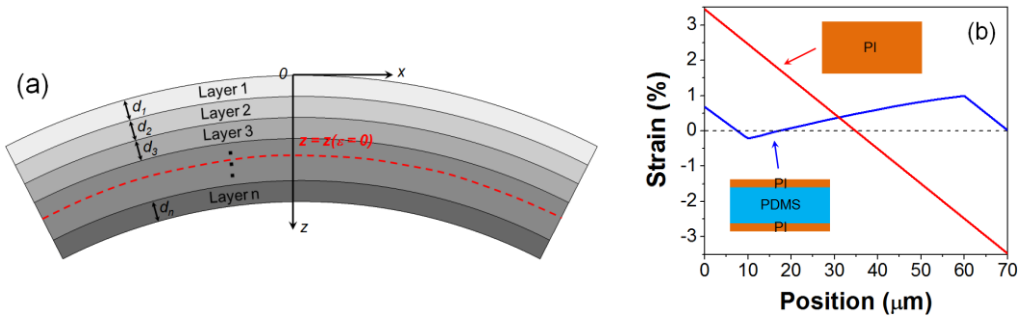

Figure 4.1 (a) Pure bending of a multi-layer structure, whose the top and bottom surfaces undergo tensile and compressive strain, respectively. The neutral plane position is specified by Equation 4.1. Strains vanishes at the neutral plane, and thus maximum bending flexibility is achieved when the photonic devices are located at the plane; (b) Finite element simulated through-thickness strain distribution in structures bent to a radius of 1 mm: the blue curve corresponds to strain in a polyimide (10 μm)-silicone (50 μm)-polyimide (10 μm) tri-layer structure, and the red curve plots strain in a single polyimide layer of the same total thickness (70 μm). The large, three-orders-of-magnitude modulus mismatch between silicone and polyimide results in significant shear strain in silicone which invalidates Equation 4.1 and effectively relieves the strain on the multi-layer stack surfaces.

4.1.2.1 Device Structure

Shown here in Figure 4.2a is the cross section structure of our fabricated flexible device. It consists of three layer structure, the bottom layer is our device layer, in which the photonic chip is embedded in an epoxy (Su-8) film; The top two layers are polyimide and silicone adhesive, which has a much lower young's modulus, 3 orders of magnitude lower compared to those of polyimide and su-8.

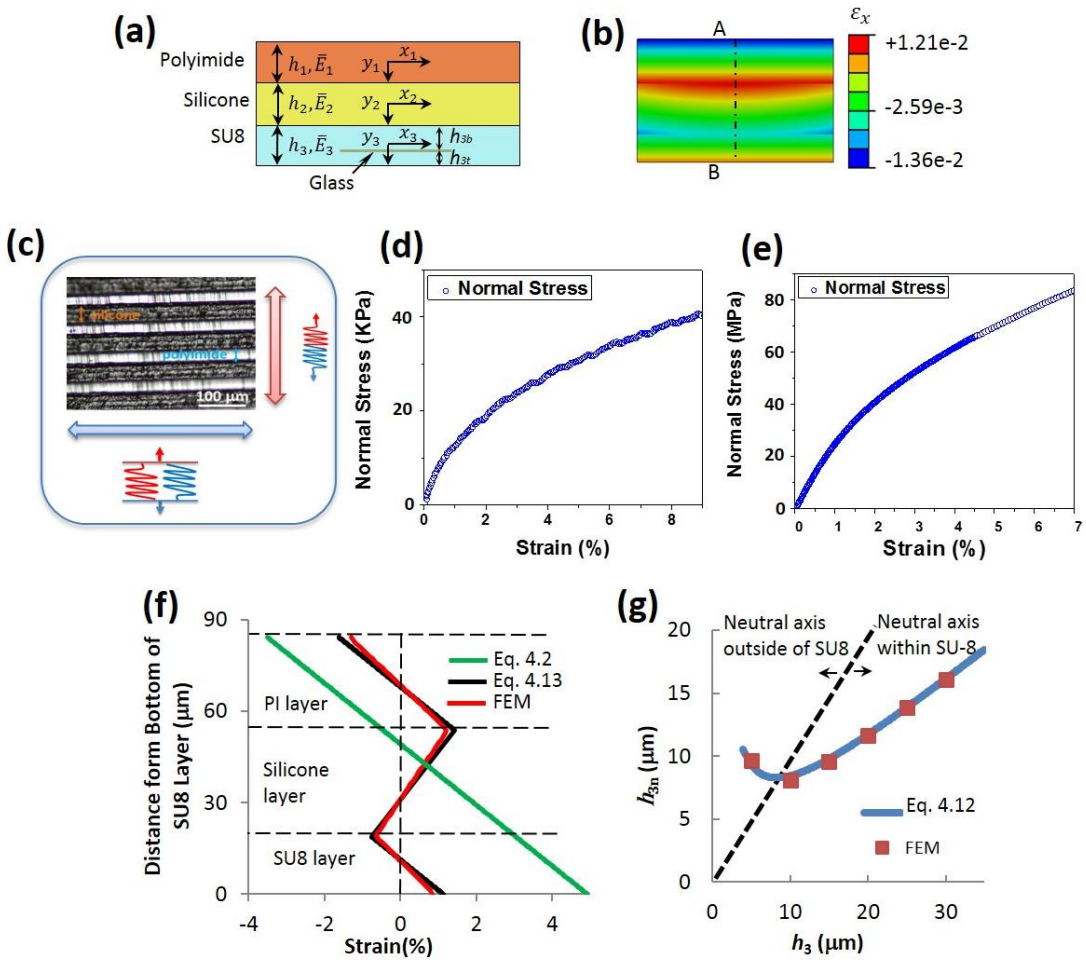
(a)
Polyimide
Silicone
SU8
Glass
(b)
A
B
+1.21e-2
-2.59e-3
-1.36e-2
(c)
100 μm
(d)
Normal Stress
Normal Stress (KPa)
Strain (%)
(e)
Normal Stress
Normal Stress (MPa)
Strain (%)
(f)
Distance form Bottom of SU8 Layer (μm)
Eq. 4.2
Eq. 4.13
FEM
PI layer
Silicone layer
SU8 layer
Strain(%)
(g)
Neutral axis outside of SU8
Neutral axis within SU-8
Eq. 4.12
FEM

Figure 4.2 Young's Modulus measurement and Multi-neutral-axis theory. (a) Cross-sectional schematic of the flexible photonic chip, with a PI-silicone-SU8 three-layer structure (not drawn to scale), thickness and plane strain Young's modulus are as labelled, and the local coordinate originates from the median plane of each layer; (b) Contour plot of bending strain distribution obtained from FEM when the structure in Fig 4.2a is bent; (c) Cross-sectional optical microscope image of a Kapton tape stack; (d) Typical stress-strain curve of the silicone layer.; (e) Typical stress-strain curve of the polyimide layer; (f) Through-stack strain distribution in the flexible chip with an SU-8 layer thickness of 18.9 μm when bent to a radius of 1 mm: the green line represents results calculated using the conventional theory (Eq. 4.2), the black curve is derived using our multiple neutral-axes theory (Eq. 4.13), and the red curve are FEM simulations; (g) the position of SU-8 neutral axis from SU-8 surface as a function of SU-8 thickness. The blue curve comes from Eq. 4.12 and the solid markers are FEM results. Dash line denotes the boundary of SU-8. When the h_3 is smaller than the critical value of 8.28 μm, the neutral axis will shift outside SU-8 to the left hand side of the dash line and hence is not accessible to the device.

4.1.2.2 Measurements of Material Mechanical Properties

Before we conduct any analytical modeling or FEM simulation, the material mechanical properties in each layer should be obtained. Figure 4.2a schematically illustrates the thickness profile of the fabricated flexible photonic chip from top to bottom comprising the polyimide (PI) substrate, the silicone adhesive, and the SU-8 cladding layer in which the devices are encapsulated. We experimentally measured the Young's moduli of thin film PI, silicone, and SU-8 to be E_1 = 2.5 GPa, E_2 = 1.5 MPa, and E_3 = 2 GPa, respectively (Figure 4.2c-e).

The Young's moduli of the constituent materials were experimentally extracted from uniaxial tensile tests performed on an RSA3 dynamic mechanical analyser (TA instruments) with a Hencky strain rate of 0.01 s^{-1}. The layer thicknesses were measured by optical microscopy (Figure 4.2c). The uniaxial strain-stress characteristics of the

silicone adhesive layer and the polyimide layer were measured on the Kapton tapes. Specifically, two sets of experiments were performed: a double-layer Kapton tape was stretched in-plane to determine the modulus of polyimide, and a stack of Kapton tapes (Figure 4.2c) underwent out-of-plane tensile tests to extract the strain-stress behaviour of the silicone adhesive layer. In the former case, since the modulus of polyimide is over three orders of magnitude higher than that of silicone, the in-plane stress is predominantly sustained by the polyimide layer. In the latter case, the strain primarily occurred in the silicone layer given its much lower modulus. The two measurements are analogous to the parallel and series connection of two elastic springs with vastly different spring constants (inset of Figure 4.2c). Both types of experiments were repeated on multiple (> 6) samples for statistical averaging. The statistically averaged strain-stress curves of polyimide and silicone calculated from the measurement results are plotted in Figure 4.2d-e.

4.1.2.3 FEM Validation for Multi-neutral Axis Mechanical Design

We validated this multi-neutral axis design using both finite element modelling (FEM) modelling. Finite element simulations were applied by ABAQUS 6.10 using plane strain elements (CPE4R) for the multilayer structure. In experiment, the concave bending of PI-silicone-SU-8 three-layer structure was actually induced through buckling mode (Figure 3.4c) instead of pure bending. For this concave bending, PI layer which has larger bending rigidity compared with other two layers shares the most part of bending moment such that the bending of other two layers can be considered as being dragged by PI layer. We applied rotation boundary conditions on the two ends of PI

layer which can generate curvatures the same with experiments at middle point of the structure to simulate this buckling induced bending.

Figure 4.2b shows the strain distribution in a bent flexible photonic chip simulated using FEM: when the multilayer is subject to concave bending, FEM results clearly show that the strain distribution is not monotonic across the stack thickness. Both compressive and tensile strains are present in the PI and SU-8 layers, which is contradictory to Equation 4.1 where only one neutral axis exists in the structure. Because of the soft silicone interlayer, the location of the neutral axis can be shifted away from near the centre of the multilayer stack to within SU-8, a salient feature which enables photonic designs capitalizing on and enabling evanescent interactions while claiming extraordinary mechanical flexibility.

4.1.2.4 Analytical Modeling for Multi-neutral Axis Mechanical Design

To accurately predict the strain distribution in each layer analytically, we assume that the cross-sectional planes in PI and those in SU-8 remain planar during bending. Therefore, linear relation between strain and curvature (Equation 4.2) is still valid.

The coordinate system we adopt is depicted in Figure 4.2a, with notations given in Table 4.1.

Table 4.1 Notations used in the mechanical modelling

Layer	Young's Modulus	Thickness	Strain distribution	Distance from neutral axis to median plane	Distance from neutral axis to bending centre
PI	$\bar{E}_1$	h_1	$\epsilon_1(y_1)$	d_1	ρ_1
silicone	$\bar{E}_2$	h_2	$\epsilon_2(y_2)$	--	--
SU-8	$\bar{E}_3$	h_3	$\epsilon_3(y_3)$	d_3	ρ_3

Our goal is to find an analytical solution for d_3 so that we know where to place the photonic devices for minimum strain.

Using the local coordinate systems, strain in PI can be written as:

$$\epsilon_1(y_1) = \frac{y_1 - d_1}{\rho_1} \ \left(-\frac{h_1}{2} < y_1 < \frac{h_1}{2}\right) \qquad (4.3)$$

Strain in the SU-8 layer is

$$\epsilon_3(y_3) = \frac{y_3 - d_3}{\rho_3} \ \left(-\frac{h_3}{2} < y_3 < \frac{h_3}{2}\right) \qquad (4.4)$$

We suppose that strain in silicone layer is a linear function of y_2 as inspired by our FEM results:

$$\epsilon_2(y_2) = ay_2 + b \ \left(-\frac{h_2}{2} < y_2 < \frac{h_2}{2}\right) \quad (4.5)$$

where *a* and *b* are coefficients to be determined by continuity conditions at PI/silicone and silicone/SU-8 interfaces.

Continuity at layer interfaces imposes:

$$\begin{cases} \epsilon_2\left(-\frac{h_2}{2}\right) = \epsilon_1\left(\frac{h_1}{2}\right) \\ \epsilon_2\left(\frac{h_2}{2}\right) = \epsilon_3\left(-\frac{h_3}{2}\right) \end{cases} \qquad (4.6)$$

Force equilibrium in *x* direction imposes:

$$\bar{E}_1 \int_{-\frac{h_1}{2}}^{\frac{h_1}{2}} \frac{y_1 - d_1}{\rho_1} dy + \bar{E}_3 \int_{-\frac{h_3}{2}}^{\frac{h_3}{2}} \frac{y_3 - d_3}{\rho_3} dy_3 + \bar{E}_2 \int_{-\frac{h_2}{2}}^{\frac{h_2}{2}} (ay_2 + b) dy_2 = 0$$

(4.7),

Combing Equation 4.6 and 4.7 yields a relation between d_1 and d_3:

$$2\left(\frac{\bar{E}_1 h_1 d_1}{\rho_1} + \frac{\bar{E}_3 h_3 d_3}{\rho_3}\right) = \bar{E}_2 h_2 \left(\frac{\frac{h_1}{2} - d_1}{\rho_1} - \frac{\frac{h_3}{2} + d_3}{\rho_3}\right) \qquad (4.8)$$

which satisfies the following two extreme cases: (i) When E_2=0, i.e. there is no material layer between PI and SU-8, both d_1 and d_3 should go to zero. (ii) When $\bar{E}_1 = \bar{E}_2 = \bar{E}_3$, i.e. the composite beam decays to a beam of uniform material, there should be only one neutral axis, i.e. $d_1 = \frac{h_2 + h_3}{2}$ and $d_3 = -\frac{h_1 + h_2}{2}$.

Assuming PI and SU-8 have the same original length and the same bending angle, the bending radius from each layer's neutral axis to its bending center should also be the same, which means

$$\rho_1 = \rho_3 \qquad (4.9)$$

Substituting Equation 4.9 into Equation 4.8 yields:

$$2(\bar{E}_1 h_1 d_1 + \bar{E}_3 h_3 d_3) = \bar{E}_2 h_2 \left((\frac{h_1}{2} - d_1) - (\frac{h_3}{2} + d_3) \right) \qquad (4.10)$$

As shown in Table 4.1, $\bar{E}_2 \ll \bar{E}_1$ and $\bar{E}_2 \ll \bar{E}_3$, which implies that the right hand side of Equation 4.10 is much smaller than the left hand side and can be approximated as zero, hence

$$d_3 = -d_1 \frac{\bar{E}_1 h_1}{\bar{E}_3 h_3} \qquad (4.11)$$

For a constant PI thickness, our FEM results have validated a hypothesis that due to the soft silicone interlayer, the thickness of SU-8 has little effect on the position of the neutral axis of PI layer as long as SU-8 is thinner or of comparable thickness to the PI. We may then take d_1 as a constant and by fitting the FEM results, we obtain $d_1 = 0.836$ μm.

The distance from SU-8 surface to SU-8 neutral axis h_{3n} is thus given by:

$$h_{3n} = \frac{h_3}{2} + d_1 \frac{\bar{E}_1 h_1}{\bar{E}_3 h_3} \qquad (4.12)$$

where d_1 = 0.836 μm is the distance from the PI neutral axis to the PI median plane, which is found to be a constant when silicone thickness is fixed. In a single free-standing SU-8 layer, $h_{3n} = h_3/2$. When SU-8 is bonded to PI via silicone adhesive, the effect of PI is captured by the second term in Equation 4.12: the thicker the PI layer (i.e. the larger h_1), the further away the neutral axis of SU-8 from its median plane.

Once the neutral axes are determined, strain distribution across the stack thickness is given by

$$\varepsilon = \begin{cases} \frac{y_1 - d_1}{\rho} & \left(-\frac{h_1}{2} \le y_1 < \frac{h_1}{2}\right) \\ \frac{(\frac{h_2}{2} - y_1)(\frac{h_1}{2} - d_1) - (\frac{h_2}{2} + y_1)(\frac{h_3}{2} + d_3)}{\rho h_2} & \left(-\frac{h_2}{2} \le y_2 < \frac{h_2}{2}\right) \\ \frac{y_3 - d_3}{\rho} & \left(-\frac{h_3}{2} \le y_3 \le \frac{h_3}{2}\right) \end{cases}$$

(4.13)

where ρ represents the average radius of the multilayer. Results from the conventional bending theory (Equation 4.2), FEM, and our new multi-neutral-axis model (Equation 4.13) are compared in Figure 4.2f. Conventional bending theory predicts monotonic linear strain distribution whereas both FEM and Equation 4.13 capture non-monotonic strain distribution in the multilayer stack. Linear strain distribution in each layer obtained from FEM further corroborates our basic assumptions. The locations of zero strain plane for different SU-8 thicknesses calculated using Equation 4.12 are plotted in Figure 4.2g. The dashed curve in Figure 4.2g represents the equation $h_{3\mathrm{n}} = h_3$. When h_3 < 8.28 μm, the neutral axis will locate outside the SU-8 layer and hence no longer accessible for device placement.

4.2 Strain-optical Coupling [70]

To experimentally validate the new theory, we performed strain-optical coupling measurements, where the optical resonant wavelengths of glass micro-disk resonators were monitored *in-situ* while the samples were bent. A block diagram of the home-built measurement setup is illustrated in Figure 3.4a. Light from a tuneable laser was coupled into the bus waveguides via fibre end-fire coupling, and the transmittance through the chip was monitored *in-situ* as the samples were bent using linear motion stages. Figure 3.4c shows a flexible chip under testing on the setup. Further details regarding the measurement are provided in Chapter 3.3.

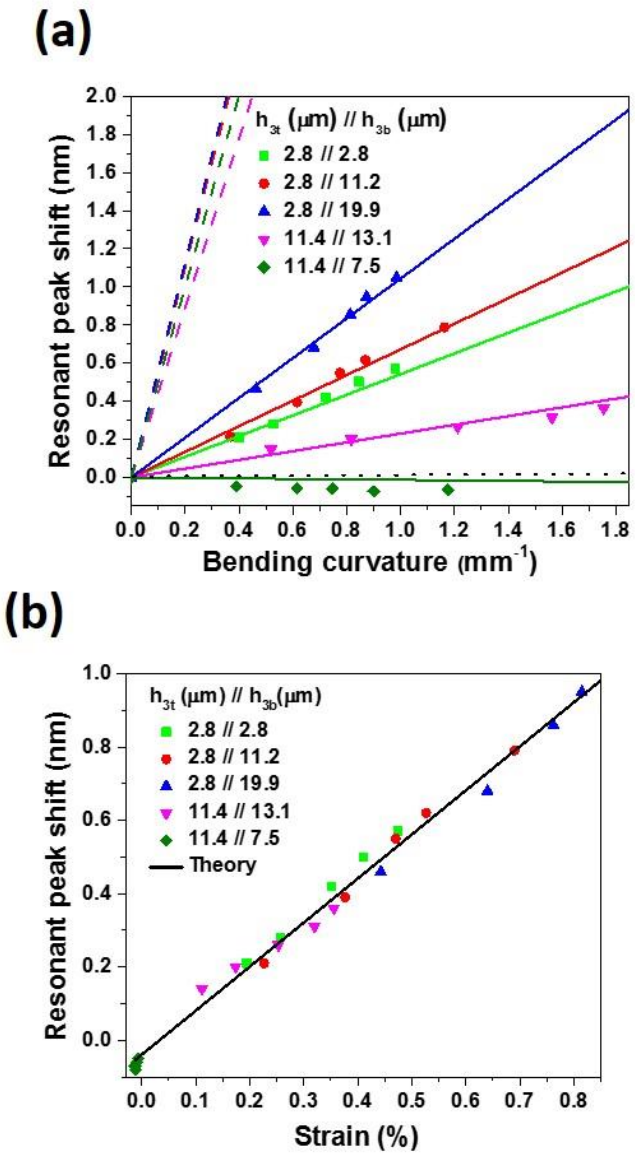

Figure 4.3 Strain-optical coupling in flexible photonic devices. (a) Resonance wavelength shift plotted as a function of bending curvature: each colour represents an SU-8 top/bottom cladding thickness combination. h_{3t} and h_{3b} denote the SU-8 top and bottom cladding thicknesses, as labelled in Figure 4.2a, dots are experimentally measured data, the solid lines are predictions made using our analytical theory, and the dashed lines are classical bending theory results. (b) Resonance wavelength shift plotted as a function of bending strain, which can be calculated from bending curvature using Equation 4.13. All data in Figure 4.2b collapse to one curve as predicted by Equation 4.14.

The resonant wavelength shift $d\lambda$ can be expressed as a function of the local strain at the resonator $d\varepsilon$:

$$\frac{d\lambda}{d\varepsilon} = \sum_i \left[\frac{\lambda}{n_g} \cdot \Gamma_i \cdot \left(\frac{dn}{d\varepsilon} \right)_i \right] + \frac{n_{eff}}{n_g} \cdot \frac{\lambda}{L} \cdot \frac{dL}{d\varepsilon} + \frac{\lambda}{n_g} \cdot \frac{dn_{eff}}{d\varepsilon} \quad (4.14)$$

where Γ_i and $(dn/d\varepsilon)_i$ are the optical confinement factor and strain-optic coefficient in the i th cavity material, L is the cavity length, and n_g and n_{eff} denote the group index and effective indices, respectively. In Equation 4.14, the first term on the right hand side (RHS) represents the optoelastic (i.e. strain-optic) *material* response, the second term manifests the cavity *length* change, and the third term results from the cavity *cross-sectional geometry* modification. Derivation of the equation follows Ref. [85]. Since the resonant wavelength of a high-Q resonator can be accurately measured down to the pico-metre level, strain-optical coupling provides a sensitive measure of local strain in the multilayer structure. A series of flexible $Ge_{23}Sb_7S_{70}$ glass micro-disk resonator samples with different SU-8 top and bottom cladding layer thickness combinations were fabricated and tested. By varying the cladding thickness, local strain at the micro-disk resonators is modified when the samples are bent. This is apparent from Figure 4.3a, where the resonant wavelength shift as a function of chip bending curvature is plotted for 5 different samples. The resonant wavelength shift was highly repeatable after several bending cycles and little hysteresis was observed. Theoretical predictions based on the classical multilayer bending theory as well as those made using our new multi-neutral-axis analysis are plotted in the same figure for comparison.

To complete the calculations, we discussed the methods to experimentally measure the materials modulus in Chapter 4.1. In addition to elastic moduli, the strain-optical coefficients are also essential parameters for calculating the strain-optical coupling strength in the flexible resonators, as suggested by Equation 4.14. However, measuring strain-optical coefficients, in particular those of thin films (which can be significantly different from those of bulk amorphous glasses), was regarded as extremely challenging task. Here we leverage the flexible resonator devices as a new measurement platform for accurate quantification of strain-optical coefficients of thin film materials. For resonators made of the same material and of the identical dimensions, Equation 4.14 suggests the same $d\lambda/d\varepsilon$ coefficient regardless of the flexible device configuration. This conclusion is supported by our experimental results: if we re-plot the strain-induced resonant wavelength shift data (Figure 4.3a) as a function of local strain at the resonators, it is clear that all data points fall on a single straight line (Figure 4.3b), indicating the same $d\lambda/d\varepsilon$ coefficient (i.e. slope of the line). Since the second and third terms in Equation 4.14 (resonator geometry change) can be readily inferred from mechanical simulations, the material strain-optical response can be calculated by subtracting the contributions from the two terms. The calculation was used to generate the theoretical results in Figure 4.3a.

It is apparent that the classical theory fails to reproduce the experimentally observed trend while our new theory successfully accounts for the strain-optical coupling behaviour. The dramatic change of both magnitude and sign of the resonance shift in different samples provides an effective method to control strain-optical coupling in flexible photonic devices and also bears important practical implications: for applications where strain-optical coupling is undesirable such as resonator

refractometry sensing, the coupling can be nullified by strategically placing the device at the zero strain points. On the other hand, the coupling can be maximized when applied to photonic tuning or strain sensing.

The local neutral axis design imparts extreme mechanical flexibility to our devices. To test the mechanical reliability of the flexible devices, micro-disk resonators were fabricated and their optical characteristics were measured after repeated bending cycles at 0.5 mm bending radius. As shown in Figure 3.7d that there were minimal variations of both the quality factor and extinction ratio after multiple bending cycles, indicating superior mechanical robustness of the flexible devices. Our fatigue test consisting of up to 5,000 bending cycles at 0.8 mm radius resulted in 0.5 dB/cm increase of waveguide propagation loss and a 23% decrease of the resonator intrinsic Q-factor (Chapter 3.4).

4.3 Summary

Noting that the conventional multilayer bending theory fails when laminates have large elastic mismatch, we derived a mechanics theory accounting for multiple neutral axes in one laminated structure to accurately predict its strain-optical coupling behavior. This chapter includes all of the details about the FEM simulation and analytical modeling. A series of experiments were also designed to validate the developed multi-neutral axis mechanical theory. And the experimental results finally agree well with the theory and simulation.

Chapter 5

3-D FLEXIBLE INTEGRATED CHALCOGENIDE GLASS PHOTONICS [70]

5.1 Fabrication Approaches for 3-D Photonic Devices

Since our technology utilizes high-index ChGs as the backbone photonic materials, their amorphous nature further enables us to scale the fabrication method to 3-D monolithic photonic integration on plastic substrates using multilayer deposition and patterning. The excellent planarization capability of ultra-thin SU-8 resin ensures pattern fidelity in the multilayer process. As shown in Figure 5.1, the glass deposition, lift-off process, Su-8 planarization can be repeated several times to complete the fabrication of multi-layer 3-D photonic devices. More details related to the process have been discussed in Chapter 3.2. This approach offers a facile and simple alternative for 3-D photonic structure fabrication to conventional methods involving ion implantation [40], wafer bonding [38], or pick-and-place nanomanipulation [39].

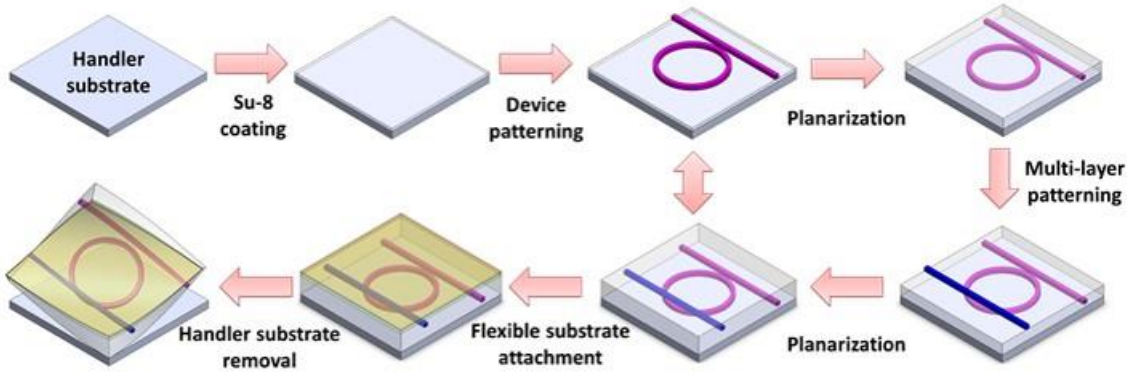

Figure 5.1 Schematic overview of the monolithic 3-D flexible photonic device fabrication process.

5.2 Ultra-thin SU-8 Planarization Capability

Planarization is the key to our multilayer 3-D fabrication process. We choose SU-8, an epoxy-based negative photoresist, as the planarizing agent. Unexposed SU-8 is a thermoplastic with a glass transition temperature (Tg) of 50 °C [86], which is amenable to thermal reflow processing at a relatively low temperature to create a smooth surface finish through the action of surface tension. Once cured or UV cross-linked, SU-8 transforms to a thermosetting polymer with a high Tg > 200 °C and stable thermal/mechanical/chemical properties. To validate the planarization behaviour of SU-8 on glass devices, a layer of 460 nm thick SU-8 epoxy was spin coated on gratings patterned in a 360 nm thick Ge23Sb7S70 film (i.e. 100 nm overcoating layer thickness). Figure 5.2a shows top-view optical micrographs of the grating patterns after SU-8 spin coating. The gratings have a fixed duty cycle of 0.5 and their periods are varied from 1.2 μm to 120 μm. The SU-8 layer topography after heat treatment was examined using cross-sectional SEM, and Figure 5.2b(bottom) shows an exemplary SEM image of the grating structure after planarization. Transfer function of the planarization process was

plotted as a function of spatial frequency (reciprocal of grating pitch) in Fig. S1c. Top panel of Figure 5.2b schematically illustrated the definition of degree of planarization (DOP) and planarization angle (θ). The degree of planarization (DOP) is given by: $DOP = 100\% * \frac{t_1 - t_2}{t_2}$, and the planarization angle (θ) by $\theta = \arctan(\frac{t_1 - t_2}{W})$, where W is width of the grating line (i.e. half of the grating pitch). The ultra-thin (100 nm thickness) SU-8 overcoating layer produces DOP consistently larger than 98% for patterns with micron-sized pitch. Such planarization performance is considerably better than previous reports using BCB, PMMA or polyimide as the planarization agent, as shown by the comparison in Table 5.1.

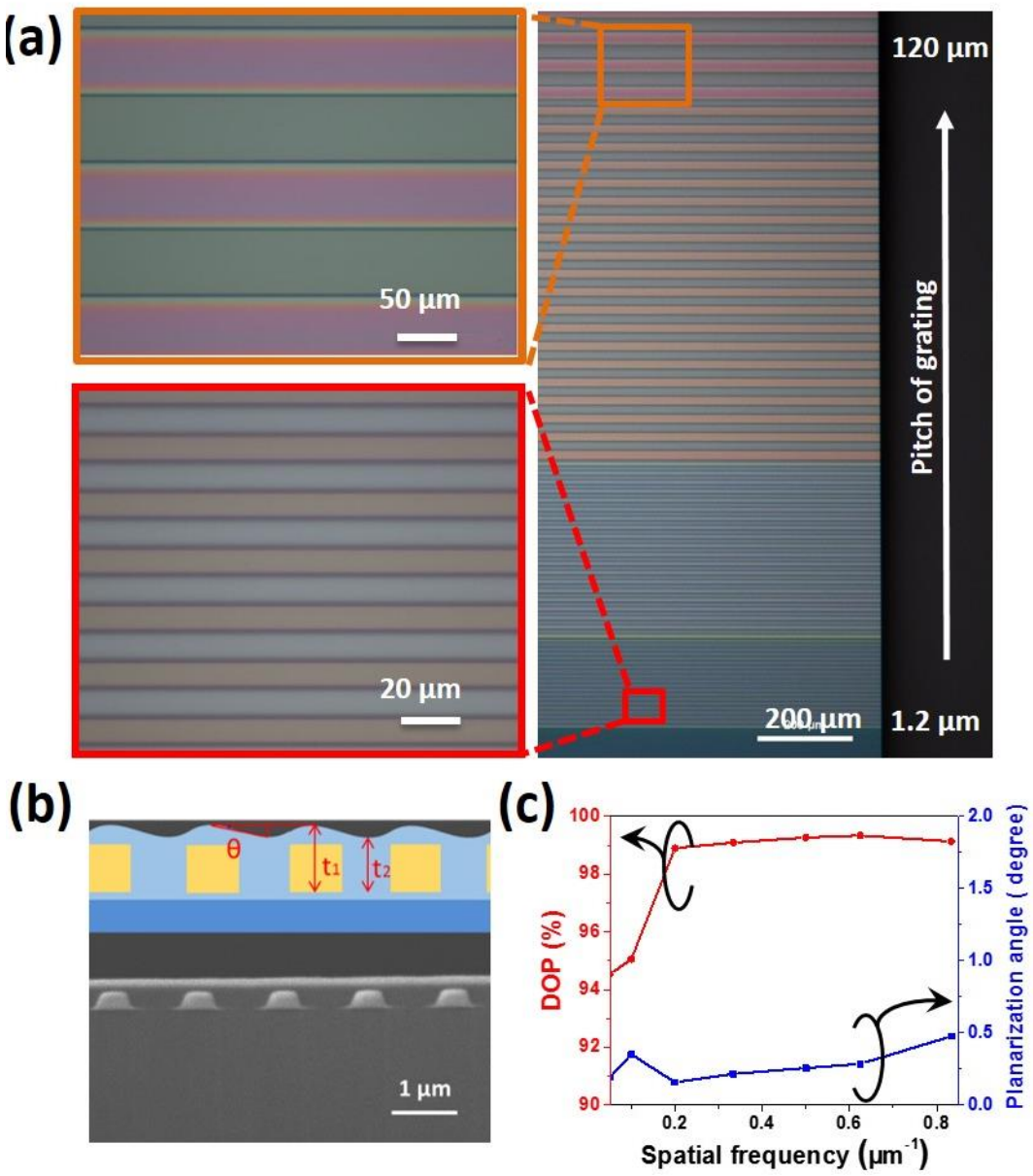

Figure 5.2 Ultra-thin SU-8 planarization characterizations. (a) Optical microscope images of glass grating patterns after single-layer SU-8 planarization; (b) SEM cross-sectional image of planarized gratings; the top inset illustrates the definition of DOP and planarization angle; (c) Plot of degree of planarization and planarization angle as functions of spatial frequency. The SU-8 planarization process consistently shows a DOP above 98% over micron-sized features and a small planarization angle < 1°.

Table 5.1 Degree of planarization (DOP) of thin SU-8 compared to literature values using Polybenzocyclobutene (PBCB), Poly(methyl methacrylate) (PMMA) and polyimide (PI). The overcoating layer thickness is defined as the thickness of the planarization coating minus that of the underlying features to be planarized.

Materials	Overcoating thickness (μm)	Planarized topography	DOP
SU-8 (this report)	0.1	5 μm pitch grating (duty cycle 0.5)	99%
	0.1	20 μm pitch grating (duty cycle 0.5)	95%
BCB[87]	0.3	10 μm wide trenches on a pitch of 30 μm	90%
	0.3	10 μm wide trenches on a pitch of 120 μm	70%
PBCB[88]	4.5	20 μm pitch grating (duty cycle 0.5)	85%
PI2555[88]	1	20 μm pitch grating (duty cycle 0.5)	50%
PMMA[88]	0.5	20 μm pitch grating (duty cycle 0.5)	18%

5.3 Demonstration of Several Fabricated 3-D Flexible ChG Photonic Devices

Here we demonstrate the fabrication of several important device building blocks including broadband interlayer waveguide couplers, vertically coupled resonators, and woodpile photonic crystals using our approach. It is worth noting that all devices presented here were fabricated using simple, low-cost UV contact lithography without resorting to fine-line patterning tools such as electron beam lithography or deep-UV lithography, and we expect significant device performance improvement through further optimization of processing steps.

5.3.1 Adiabatic Interlayer Waveguide Couplers

Waveguide coupler is one of the fundamental and important components in photonic integrated circuits. It is commonly used to couple light between different waveguides. Three types of waveguides couplers such as directional couplers, multimode interference (MMI) couplers and adiabatic couplers have been studied a lot. We want to demonstrate adiabatic couplers using the developed fabrication technique considering that both directional couplers and MMI couplers are sensitive to wavelength [89]. It is believed that there is no heat or matter transfer in an adiabatic process within a thermodynamic system. Here adiabatic waveguide couplers mean that there is no energy change between different modes in the coupler structure [89], which requires a super waveguide taper design to obtain an efficient coupling between two different waveguides. Figure 5.3a schematically shows the structure of the interlayer adiabatic waveguide coupler. The coupler consists of a pair of vertically overlapping inverse taper structures made of $Ge_{23}Sb_7S_{70}$ glass. The width of the taper sections varies gradually

from 0.9 μm to 0.6 μm in each layer. The size of the taper cross-section decrease/increase very slowly so that the local first-order mode of the waveguide can propagate from one layer to the other adiabatically [90]. The non-tapered waveguide sections are 0.9 μm wide and 0.4 μm high, designed for single quasi-TE mode operation at 1550 nm wavelength. The thickness of the interlayer SU-8 can be tuned for different coupling condition of the top and bottom layer waveguides. According to the coupled-mode theory, the whole two layer waveguides should be regarded as a superstructure if the thickness of interlayer SU-8 is small enough. Supermodes were generated due to the strong overlap of the individual waveguide modes in each layer. The device operates on the supermode adiabatic transformation principle [91, 92], where light entering the coupler pre-dominantly remains in the coupled waveguide system's fundamental mode. The simulated field mode intensity profiles of the coupled waveguides in the taper section were plotted in Figure 5.3c insets. The effective indices of the even mode and odd mode were also plotted along the taper length and change slowly with the increasing/decreasing size of the cross-section superstructure. As shown in the figure, the even supermode, which has a larger overlap with the coupled waveguide system and is the fundamental mode, transitions adiabatically from the top waveguide to the bottom waveguide as the waveguide width changes in the taper section. Figure 5.3b shows a side view of finite-difference time domain (FDTD) simulated steady-state optical field intensity distribution in the coupler, which illustrates the power transfer process from the top waveguide to the bottom one. Unlike traditional directional couplers based on phase-matched evanescent coupling, the adiabatic mode transformer coupler design is robust against fabrication error and wavelength dispersion. The adiabatic interlayer coupler exhibited broadband operation with 1.1 dB (single coupler) and 2.0 dB (double

couplers) insertion loss (both averaged over a 50 nm band), comparable to the simulation results (0.5 dB loss per coupler) given the limited alignment accuracy of contact lithography and waveguide sidewall roughness scattering loss (Figure 5. 3d).

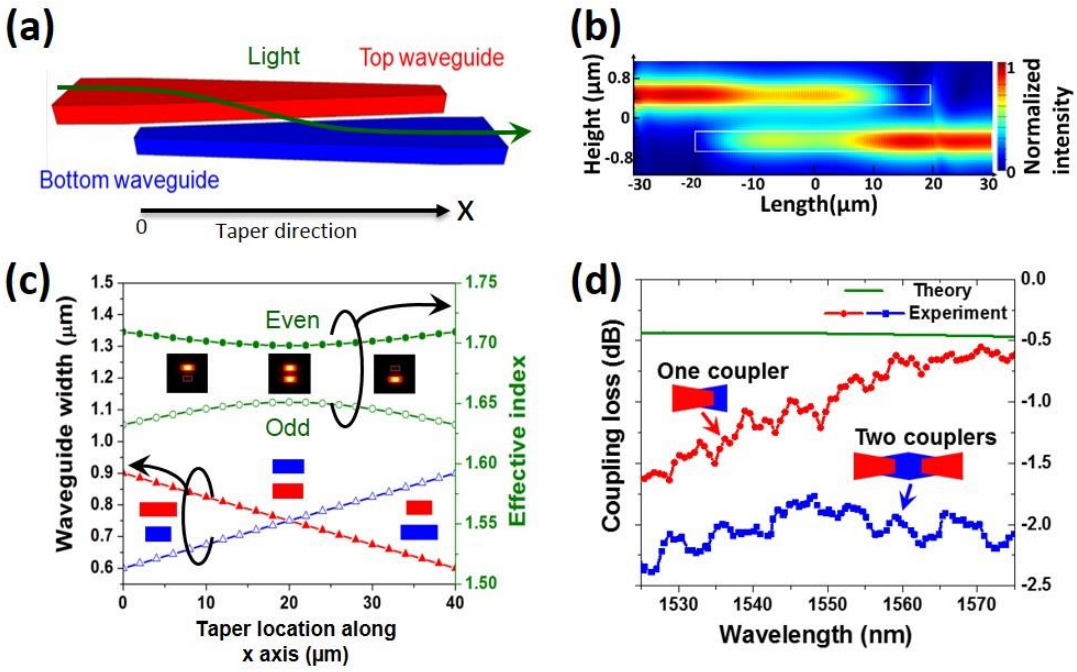

Figure 5.3 Adiabatic interlayer waveguide couplers. (a) Schematic structure of the interlayer waveguide coupler; (b) Side view of steady-state optical field intensity distribution in the coupler, showing adiabatic power transfer from the top waveguide to the bottom one; (c) Top (red curve) and bottom (blue curve) waveguide widths and simulated supermode effective indices (green curves) in the taper section of the interlayer coupler, x axis is denoted in Fig. 5.3a; the three insets show the cross-sectional even supermode intensity profile evolution along the taper; (d) FDTD simulated (green line) and measured (red and blue lines) transmission spectra of the interlayer coupler(s).

5.3.2 Vertically Coupled Add-drop Resonator Filter

Vertically-coupled resonator add-drop filters were fabricated using the same approach on plastic substrates (Figure 5.4a). The device consists of a micro-disk resonator co-planar with the add waveguide, and a through-port waveguide in a second layer separated from the micro-disk by a 550 nm thick SU-8 layer. Unlike co-planar add-drop filters where coupling strength has to be adjusted by changing the narrow gap width between bus waveguides and the resonator, critical coupling regime in vertical resonators is readily achieved via fine tuning the SU-8 separation layer thickness.

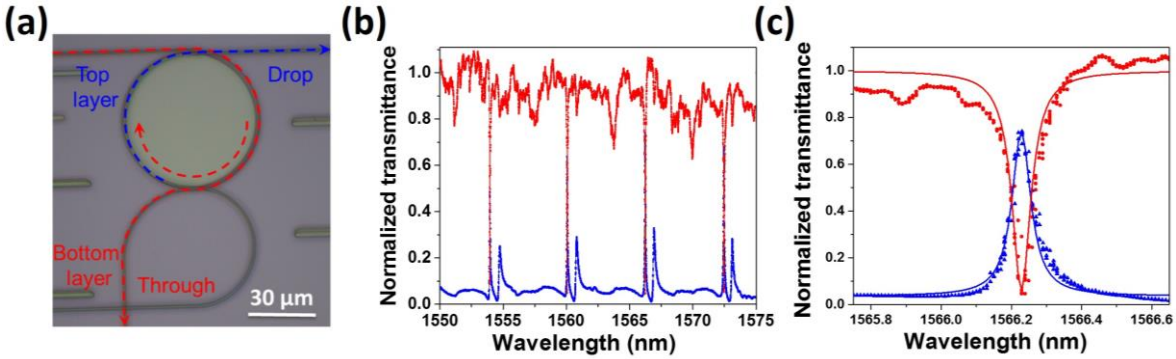

Figure 5.4 Vertically coupled add-drop resonator filter. (a) Optical microscope image of a two-layer vertically coupled resonator; (b)-(c), Normalized transmission spectra of a vertically coupled resonator at its through (red) and drop (blue) ports. The device is designed to operate at the critical coupling regime near 1550 nm wavelength. The dots represent experimental data and the lines are the theoretical results calculated using a scattering matrix formalism.

5.3.2.1 Theoretical Prediction

The vertically coupled add-drop filter can be treated using a circuit model [93] shown in Figure 5.5. The power coupling coefficients between the resonator and the add and drop port waveguides are given by K_1 and K_2, respectively. Power loss due to

coupling is neglected in the calculation. L is the resonator circumference and α is the optical loss in the micro-disk resonator. Using the scattering matrix method, loaded quality factor Q_{load}, maximum power at the drop port and minimum power at the through port at resonance can be obtained by the equations:

$$Q_{load} = \frac{2\,\pi n_g L}{\lambda_r (K_1 + K_2 + (1-\sigma^2))} \tag{5.1}$$

$$I_{drop-max} = I_{in} \frac{K_1 K_2 \sigma^2}{(1-\sigma\sqrt{1-K_1}\sqrt{1-K_2})^2} \tag{5.2}$$

$$I_{through-min} = I_{in} \frac{(\sqrt{1-K_1}-\sigma\sqrt{1-K_2})^2}{(1-\sigma\sqrt{1-K_1}\sqrt{1-K_2})^2} \tag{5.3}$$

where λ is the resonant wavelength, I_{in} is the input power, σ is the intrinsic amplitude loss in one round trip and is expressed as

$$\sigma = \exp(-1/2\ \alpha L) \tag{5.4}$$

n_g is the group index of the resonator and can be defined as follows:

$$n_g = c_0/(FSR \cdot L) \tag{5.5}$$

Here, c_0 is the light speed in vacuum, and FSR is the free spectral range (FSR) of the resonator in the frequency domain. Based on the measured transmission spectrum (Figure 5.4b) and the equations above, the coupling coefficients can be fitted, which in turn allows the prediction of the resonator transmission spectrum. The parameters used in the calculation are listed in Table 5.2.

The intrinsic quality factor (Q_{in}) of the micro-disk resonator is 1.9×10^5 calculated using [94]

$$Q_{in} = \frac{2\pi n_g}{\alpha\lambda}$$

(5.6)

which is consistent with that of all-pass resonators we fabricated using the same method.

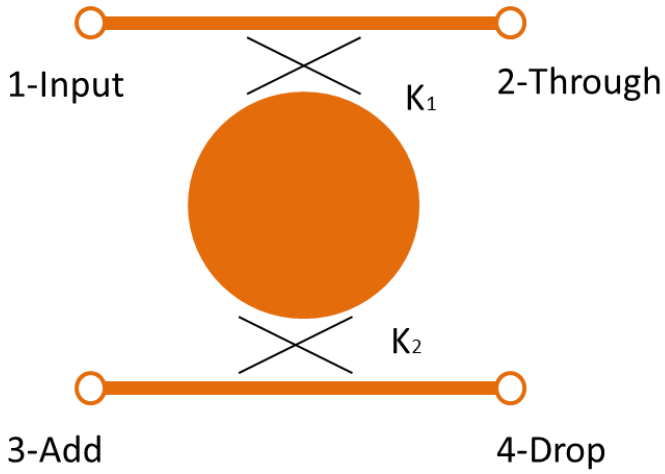

Figure 5.5 Schematic illustration of a circuit model of the vertically coupled add/drop filter.

Table 5.2 Parameters used to calculate the transmission spectrum of the vertically coupled add/drop resonator filter shown in Figure 5.4c.

L(um)	λ_r(nm)	I_{in} (nW)	I_0 (nW)	I_{thmin} (nW)	I_{drmax} (nW)	Q_{load}
188.5	1566.228	87.7	3.2	4.4	67.3	2.2×10^4
FSR(GHZ)	n_g	K_1	K_2	σ	α(dB/cm)	Q_{in}
757	2.10	0.041	0.024	0.996	2.0	1.9×10^5

5.3.2.2 Experimental Result

Figure 5.4c shows the normalized transmission spectrum of a resonator designed for critical coupling operation. The filter exhibited an insertion loss of 1.2 dB and a loaded Q-factor of 2.5×10^4 at both it's through and drop port. These results agree well with our theoretical predictions made using a scattering matrix formalism [93].

5.3.3 3-D Woodpile Photonic Crystals

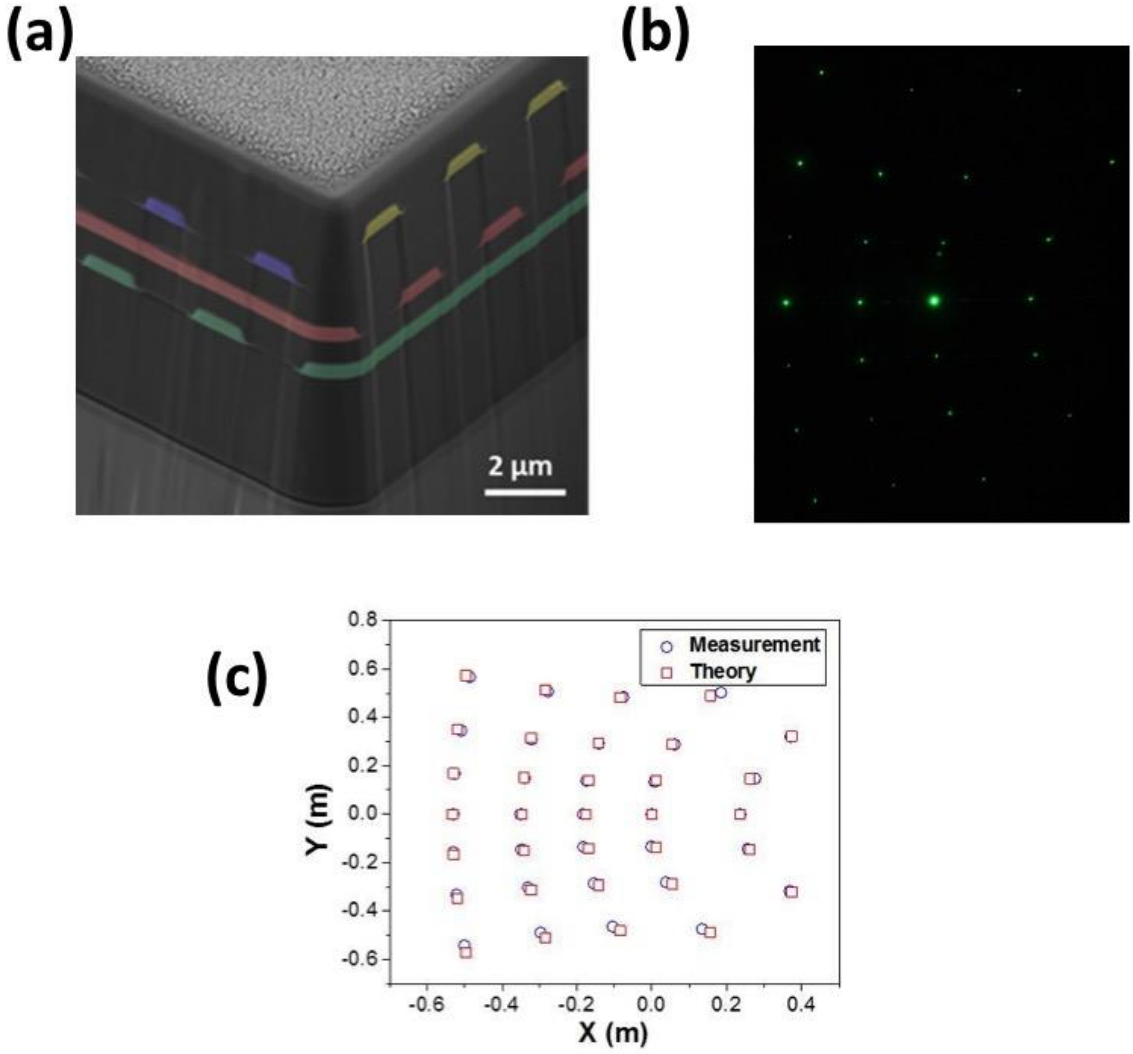

Figure 5.6 3-D woodpile photonic crystals. (a) Tilted FIB-SEM view of a 3-D woodpile photonic crystal (prior to delamination from the Si handler substrate) showing excellent structural integrity; (b) Photo of the diffraction patterns of a collimated 532 nm green laser beam from the PhC an incident angle of 45 degree; (c) The red dots are diffraction patterns simulated using the Bragg diffraction equation, the blue dots are diffraction patterns form the experimental results.

Besides two-layer devices such as interlayer couplers and vertical coupled resonators filters, our technique can be readily extended to the fabrication of multilayer structures which often present major challenges to conventional fabrication methods. As an example, Figure 5.6a shows a tilted anatomy view of a four-layer woodpile photonic crystal (PhC) fabricated using the method shown in Figure 5.1 prior to delamination from the handler substrate.

5.3.3.1 Woodpile Photonic Crystal Diffraction Experiment Configurations

Figure 5.7 illustrates the diffraction experiment setup. Monochromatic green light from a collimated 532 nm diode-pumped solid state green laser was incident at an angle θ = 45 degrees upon the surface of the PhC sample, and the diffraction patterns were projected onto a white board perpendicular to the (0 0) specular order reflection. To calculate the projected positions of different diffraction orders, the wave vector can be decomposed in the coordinate system shown in Figure 5.7, where the x and z axes are in-plane with the woodpile PhC structure while the y axis is perpendicular to the PhC sample surface. For the (0 0) specular order, the wave vector is:

$$\vec{k}_{(0\,0)} = \left(k_{x0}, k_{y0}, 0\right) = (k_0 cos\theta, k_0 sin\theta, 0) \tag{5.7}$$

where k_0 is the wave vector in vacuum. For a diffraction spot of the (n m) order, its wave vector is:

$$\overleftarrow{k}_{(n\,m)} = \left(k_x, k_y, k_z\right) = (k_{x0} + \mathrm{n}\, G_x, \sqrt{k_0^2 - k_x^2 - k_z^2}, \mathrm{m}\, G_z\,) \tag{5.8}$$

according to the Bragg diffraction equation, where G_x, G_z are the PhC in-plane reciprocal lattice vectors. Thus the diffraction angle of the (n m) order light with respect to the (0 0) order can be calculated using:

$$\alpha = \arctan\left(\frac{k_x}{k_y}\right) - \theta \tag{5.9}$$

$$\beta = \arctan\left(\frac{k_z}{\sqrt{k_x^2 + k_y^2}}\right) \tag{5.10}$$

and the position of the (n m) order pattern in the x'-y' plane (on the white board) is written as:

$$(\mathrm{D}\tan\alpha\ ,\ \mathrm{D}\ \tan\beta\ /\cos\alpha)$$

Diffraction patterns predicted using the approach agree well with the experimental results, as shown in Figure 5.6b.

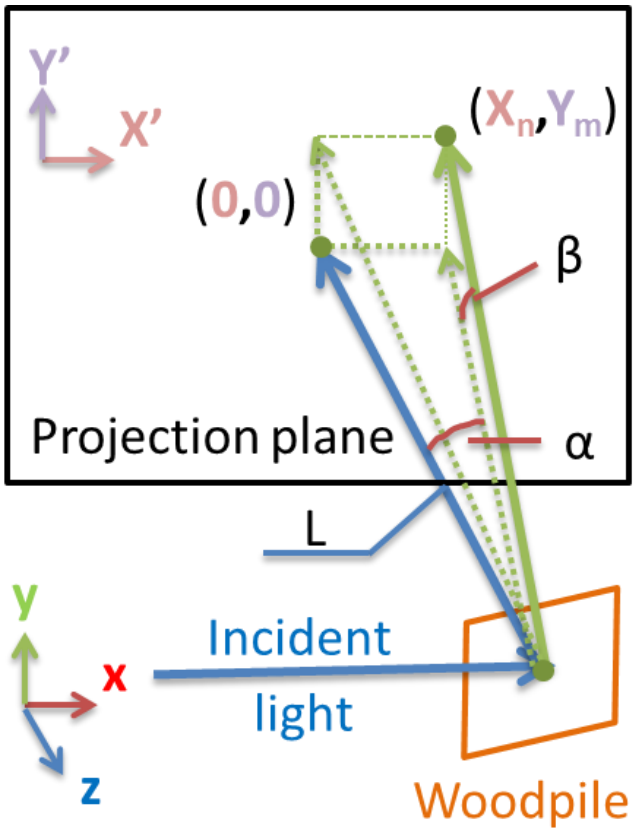

Figure 5.7 Schematic diagram illustrating the experimental setup used to map the diffracting patterns from the woodpile photonic crystal structure.

5.3.3.2 Experiment result

The PhC structure integrity and pattern fidelity were examined using optical diffraction. Figure 5.6b shows the diffraction spots from a collimated 532 nm green laser beam. The red dots in Figure 5.6b represent the diffraction pattern calculated using Bragg equations, which matches nicely with the experimental results. The well-defined diffraction pattern indicates excellent long-range structural order of the PhC.

5.4 Optimized 3-D Photonic Device Design Parameters

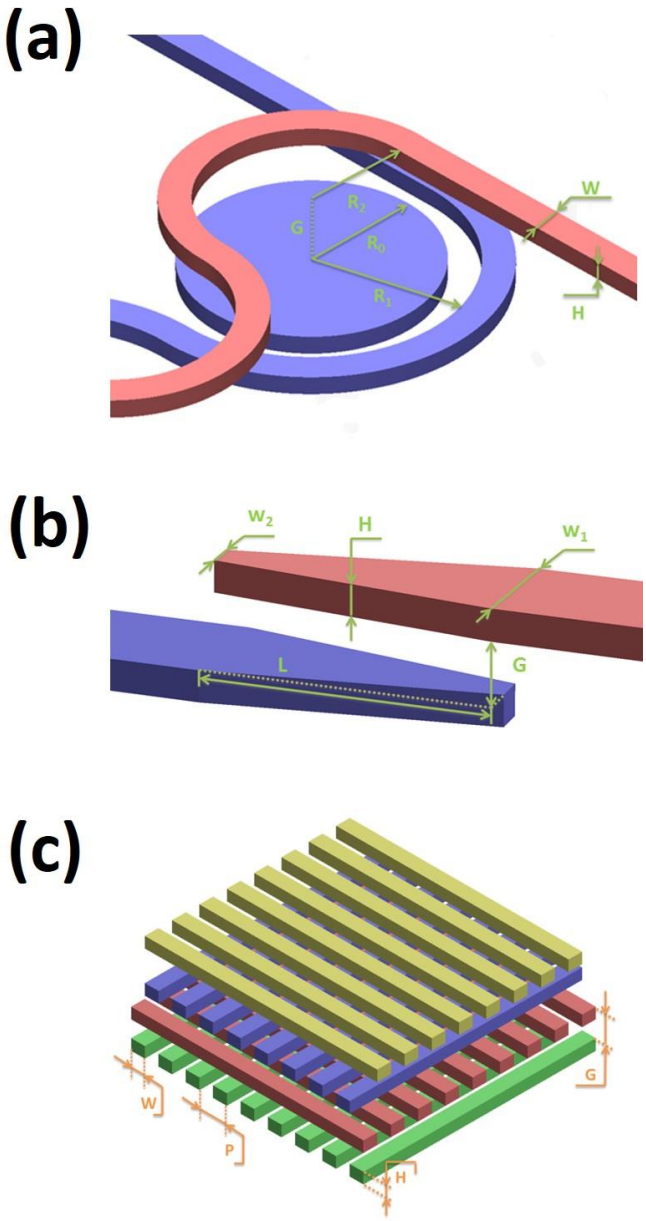

Figure 5.8 Schematic structures of 3-D photonic devices. (a) a two-layer vertically coupled resonator; (b) An interlayer waveguide couplers; (c) A woodpile photonic crystal. The key geometric parameters are labelled in the figures.

A set of 3-D photonic devices with varied design parameters were fabricated and tested. Table 5.3 summarizes the experimentally determined geometric parameter combinations that yield the optimized performance presented in this study. The denotations indicating the structure design were shown in Figure 5.8.

Table 5.3 Optimized 3-D photonic device geometric parameters.

Fig. S8a	W	H	R_0	R_1	R_2	G
(μm)	0.8	0.4	30	30.8	29.4	0.9
Fig. S8b	W_1	W_2	L	H	G	
(μm)	0.9	0.6	40	0.4	0.55	
Fig. S8c	W	P	H	G		
(μm)	1.5	3	0.36	0.8		

5.5 Summary

In conclusion, we have experimentally demonstrated a simple and versatile method to fabricate high-index-contrast 3-D photonic devices on flexible substrates. The method leverages the amorphous nature and low deposition temperature of novel Chalcogenide glass alloys to pioneer a 3-D multilayer monolithic integration approach with dramatically improved device performance, processing throughput and yield. A new mechanical theory was developed and experimentally validated to accurately predict and control the strain-optical coupling mechanisms in the device. Guided by the multi-neutral axis theory, we demonstrated mechanically robust devices with extreme flexibility despite the inherent mechanical fragility of the glass film, and the devices can be twisted and bent to sub-millimetre radius without compromising their optical performance. The 3-D monolithic integration technique, which is applicable to photonic

integration on both traditional rigid substrates and non-conventional plastic substrates, is expected to open up new application venues such as high bandwidth density optical interconnects [95], conformal wearable sensors, and ultra-sensitive strain gauges.

Chapter 6

FOLDABLE AND CYTOCOMPATIBLE SOL-GEL TiO_2 PHOTONICS [42]

6.1 Choice of TiO_2 as Photonic Materials

In this thesis work, we also investigate amorphous TiO_2 thin films deposited using a low-temperature sol-gel process as a new material for integrated biophotonic components. TiO_2 is an ideal material for integrated biophotonics for several reasons. First, it can be deposited and processed in a monolithic manner to form thin film devices at reduced temperatures compatible with flexible substrate integration. Second, TiO_2 exhibits a broad optical transparency window stretching from approximately 400 nm to 5.5 μm in wavelength [96], which covers most important wave bands for biophotonic applications including fluorescence imaging, optogenetic excitation, Raman and infrared spectroscopy. Third, TiO_2 is known as a biocompatible material, which justifies their use in cosmetic products [97], dental fillers [98, 99] and artificial bones [99] (it is, however, worth noting that while TiO_2 itself is biocompatible, chemicals or processing steps involved in deposition and microfabrication of TiO_2 devices may introduce toxic molecules). Forth, the material is no stranger to the silicon microelectronics industry, as it has been employed as a high-k dielectric material [100] which qualifies it as CMOS-compatible and potentially opens up opportunities to leverage existing foundry facilities and knowledge base in device processing. Finally, TiO_2 exhibits superior chemical and thermal stability essential for multi-step microfabrication.

While TiO_2 thin films have been widely used in photocatalysis, dye-sensitized solar cells, and as anti-reflective and/or antibacterial coatings [101-104], their

application in integrated photonics has only been explored in a few recent reports. Zhang *et al.* fabricated a high sensitivity photonic crystal biosensor with TiO_2 nanorod structure [105, 106]. Furuhashi *et al.* showed a propagation loss of 9.7 dB/cm at 632 nm wavelength for 10 μm wide TiO_2 waveguides made of reactive sputtered films. The authors suggested that the present loss was mainly due to partial crystallization of the sputtered films [107]. Hayrinen *et al.* used atomic layer deposition (ALD) to fabricate TiO_2 waveguides and reported a loss of 5.0 dB/cm at 1550 nm wavelength [108]. Bradley *et al.* and Choy *et al.* demonstrated waveguides and micro-ring resonators made of reactive sputtered TiO_2 films in both amorphous and polycrystalline (anatase) states, and they achieved a Q-factor of 22,000 near 632 nm wavelength [109]. More recently, Park *et al.* reported fabrication of whispering gallery mode (WGM) resonators in sol-gel TiO_2 by HF wet etch and claimed a high Q-factor of 10^5 at 980 nm wavelength [110]. In general, amorphous TiO_2 films exhibit lower loss than their polycrystalline counterpart. For sputtered films, the propagation loss reduces at longer wavelengths, which indicates that scattering is the likely loss mechanism. On the other hand, loss reaches a minimum at 980 nm wavelength in sol-gel films and rises to 15 dB/cm at 1550 nm, possibly suggesting the presence of residual organics that cause optical attenuation at longer wavelengths. In the prior reports the devices are exclusively integrated on silicon or glass substrates.

6.2 TiO_2 Thin Film Preparation

Here, we choose to pursue a sol-gel synthetic route free of organic species to enable flexible substrate integration since TiO_2 films deposited by traditional evaporation or sputtering processes are not suitable for photonic integration on flexible

substrates. TiO_2 films evaporated in vacuum or sputtering in a pure argon ambient are oxygen deficient and therefore exhibit high optical losses not suitable for guided wave photonic applications. The oxygen loss issue can be mitigated by plasma-assisted reactive deposition in an oxygen environment, although the process leads to severe thermal and plasma damage to polymer substrates due to a combined effect of plasma ashing and the $Ti + O_2 \rightarrow TiO_2$ exothermic reaction (ΔH = -945 kJ/mol), a unique challenge associated with flexible substrate integration. The conclusions are supported by our own experimental results on sputtered deposited TiO_2 films presented in the Additional Information. Structural and optical properties of sol-gel films were systematically characterized to define the optimal film deposition conditions with minimal optical loss. Single-mode waveguides and resonator devices were patterned on flexible substrates using reactive ion etching (RIE), and their mechanical and optical performance was tested and quantitatively accounted for using finite element mechanical modeling. We further performed cell culture experiments to confirm the cytocompatibility of the flexible TiO_2 devices.

6.2.1 Sputtering Deposited TiO_2 Thin Films

RF reactive sputtering method was first practiced to deposit TiO_2 thin films on both rigid and flexible substrates. A TiO_2 (99.9%, 2 inch in diameter, 0.125 inch in thickness, Plasmaterials Inc.) target was sputtered in an $Ar:O_2$ ambient (at flow rate ratios of 90:10 or 80:20) at a working pressure of 2.5 mTorr. Before deposition, the chamber was pumped down to a base pressure of less than 10^{-6} Torr. The TiO_2 target was pre-sputtered for 5 minutes to remove any possible surface contamination of the

target prior to initiating deposition on the substrates. The deposition rate of the film was 38 nm/hour at an RF power of 190 W.

Figure 6.1a shows XRD patterns of TiO_2 thin films on glass slides deposited at different sputtering conditions. In general, increasing oxygen partial pressure or increasing sputtering time leads to higher crystallinity in the resulting films. Figure 6.1b gives surface top-view and cross-section images of the film deposited at 10% oxygen flow ratio and 190 W for 14 hours, where the crystal grains are clearly visible. We also observed severe polymer substrate damage during sputtering deposition due to oxygen plasma ashing. The substrate etching effect is evident from Figure 6.1c and 6.1d, which show the cross-section of a TiO_2 film sputtered deposited onto an SU-8 substrate on which a trench is lithographically defined in NR9 photoresist (Futurrex Inc.). The SU-8 substrate maintains a smooth surface in the NR9 protected regions whereas significant SU-8 surface etching and roughening is observed inside the trench. Based on the results, we conclude that sputtering is not applicable to TiO_2 photonic fabrication on flexible substrates.

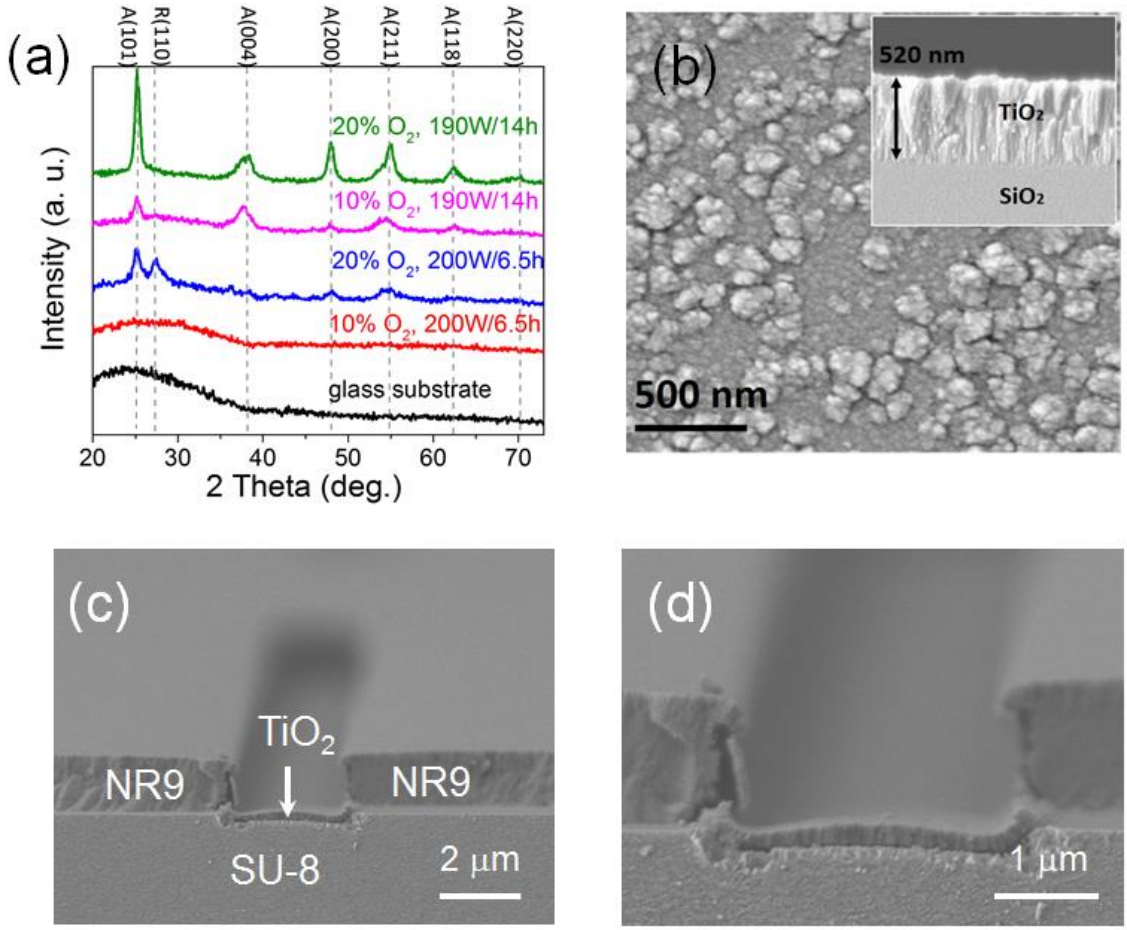

Figure 6.1 (a) X-ray diffraction spectra of TiO_2 thin films sputter deposited at different conditions. Diffraction peak positions of the anatase phase (labeled as "A") and the rutile phase (labeled as "R") quoted from JCPDS 84-1286 are also marked for comparison. (b) Top-view surface and cross-section SEM images of TiO_2 film sputtered at 10% oxygen flow ratio and 190 W for 14 hours. (c, d) SEM images of a sputtered TiO_2 film on an SU-8 substrate. A trench is lithographically defined in NR9 photoresist which serves as a resist mask. Substrate damage due to oxygen plasma is clearly visible in (d).

6.2.2 Spin-coated TiO_2 Thin films from Sol-gel Solution

Sol-gel solution process is another method we used to obtain TiO_2 thin film on the flexible substrate. Here are two major factors that may influence the quality of spin coated TiO_2 thin film using sol-gel method. The first one is remaining solvent in thin films that would contribute to the additional absorption loss; the second problem is the optimization of annealing temperature for the spin-coated sol-gel thin film. If the annealing temperature is too high, the increasing crystallinity in the thin film will lead to more scattering loss. Besides, high temperature processing techniques is not thermally compatible to the polymer substrate; while if the annealing temperature is too low, solvent will remain a lot in the thin film. To overcome these difficulties, an approach to prepare TiO_2 sol-gel using all inorganic system was developed in this thesis work, and the optimal annealing temperature around 250 ° was determined through a series of characterization experiments.

6.2.2.1 Sol-gel synthesis process

To prepare the sol, Titanium (IV) oxysulfate-sulfuric acid hydrate ($TiOSO_4 \cdot xH_2SO_4 \cdot xH_2O$) (Sigma-Aldrich, 99.99%) was first dissolved in distilled water at room temperature to form 0.05 mol/L $TiOSO_4$ solution. The solution was then precipitated by adding ammonia solution ($NH_3 \cdot H_2O$, 3 mol/L) drop by drop during magnetic stirring until the pH value of the solution increased to 7-8. White titanium hydroxide ($Ti(OH)_4$) powders precipitated in the solution and were subsequently filtered. To fully remove the NH_4^+ and SO_4^{2-} ions, the titanium hydroxide precipitate was rinsed four times in DI water prior to re-dispersing the precipitates in DI water. Hydrogen peroxide (H_2O_2, 30%) was then added slowly to the suspension solution to obtain a yellow, translucent peroxo titanic acid (PTA, $[Ti(O_2)(OH)_2]$) complex sol [111, 112].

The sol was stirred continuously for 6 to 10 hours to complete the gelation process. Lastly, the PTA sol was filtered and spin coated onto target substrates to form amorphous TiO_2 thin films.

6.2.2.2 Thin Film Characterization

During film deposition, 0.4 mol/L peroxo titanic acid (PTA) sol was spin-coated on soda-lime glass or silicon substrates at a spin speed of 1500 rpm for 0.5 seconds. The spin process was repeated 3 times to obtain a target film thickness of 380 nm. Between the spin cycles, the film was baked at 150 °C for one minute to remove residual water in the layer deposited in the previous cycle. Post-deposition annealing followed after the entire coating process to stabilize the resulting film structure.

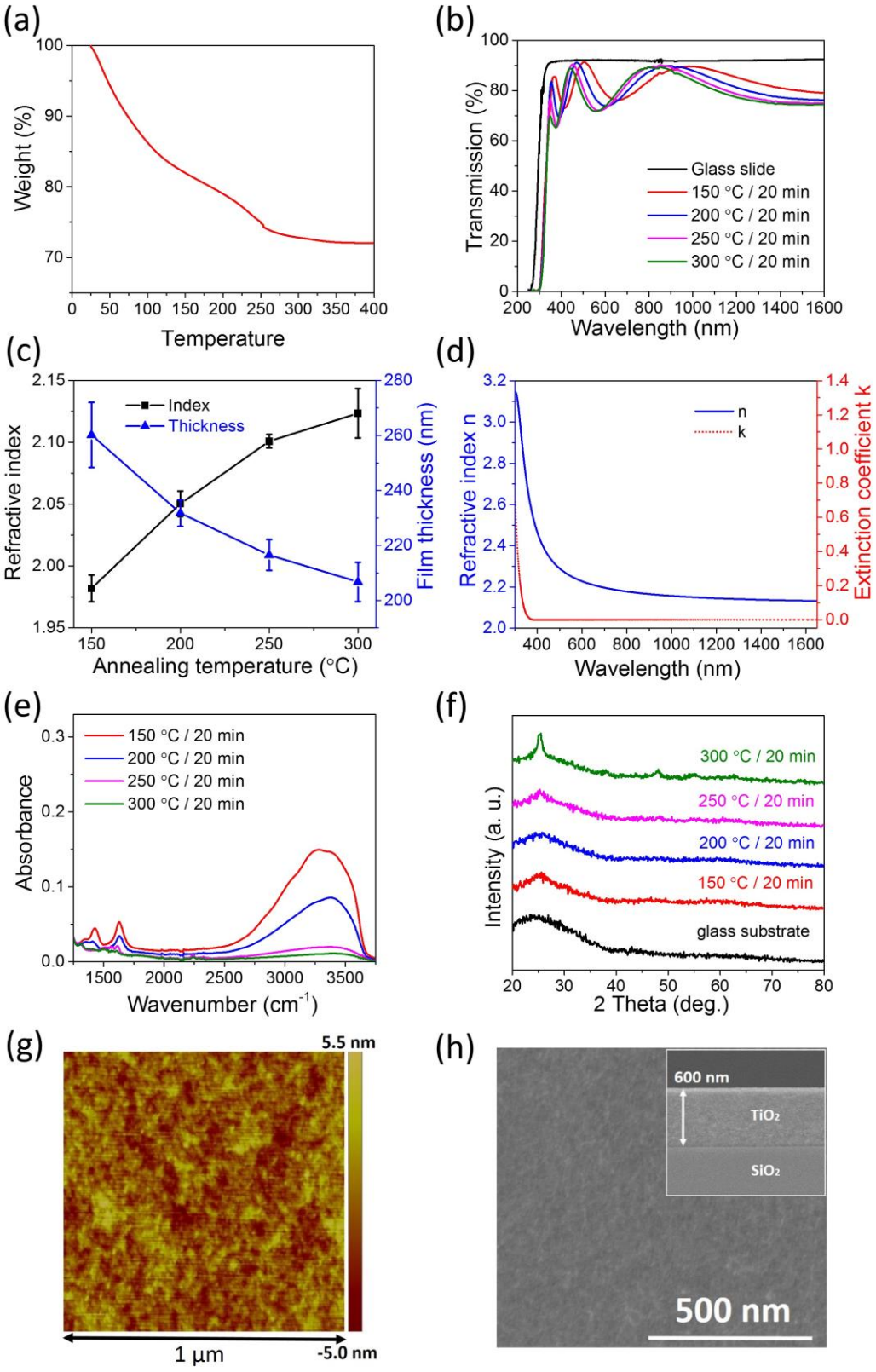
(a)
Weight (%)
Temperature
(b)
Transmission (%)
Wavelength (nm)
Glass slide
150 °C / 20 min
200 °C / 20 min
250 °C / 20 min
300 °C / 20 min
(c)
Refractive index
Film thickness (nm)
Index
Thickness
Annealing temperature (°C)
(d)
Refractive index n
Extinction coefficient k
n
k
Wavelength (nm)
(e)
Absorbance
Wavenumber (cm-1)
150 °C / 20 min
200 °C / 20 min
250 °C / 20 min
300 °C / 20 min
(f)
Intensity (a. u.)
2 Theta (deg.)
300 °C / 20 min
250 °C / 20 min
200 °C / 20 min
150 °C / 20 min
glass substrate
(g)
5.5 nm
1 µm
-5.0 nm
(h)
600 nm
TiO2
SiO2
500 nm

Figure 6.2 Characterization of sol-gel prepared TiO2 thin films annealed at different temperatures. (a) thermogravimetric analysis (TGA) curve of pre-dried PTA sol; (b) UV-Vis transmission spectra of the films on glass substrates; (c) refractive indices at 1550 nm wavelength and film thickness, both fitted from the UV-Vis spectra using the Swanepoel method; (d) refractive indices n and extinction coefficients k of TiO2 thin film annealed at 250 °C measured using ellipsometry; (e) FTIR spectra; (f) X-ray diffraction spectra; (g) AFM surface profile (1 μm × 1 μm); (h) top-view SEM image of film annealed at 250 °C; inset: film cross-section.

To identify the optimal annealing condition, thermogravimetric analysis (TGA) was performed on the pre-dried PTA sol (baked in vacuum oven at 80 °C for 24 hours). TGA results shown in Figure 6.2a suggest that the weight loss of PTA sol occurs primarily from 50 °C to 250 °C, which is attributed to loss of coordinated water and decomposition of peroxo groups. The conclusion is further supported by optical characterizations of the films. Figure 6.2b shows the UV-Vis transmittance spectra of TiO_2 thin film annealed at different temperatures. Refractive indices and thicknesses of the films were calculated from the spectra using the Swanepoel method [113] and plotted in Figure 6.2c. The fitted indices also agree well with our ellipsometry measurements (Figure 6.2d), showing the index and absorption dispersion of film annealed at 250 °C. As the annealing temperature increases, removal of water and NH_3 leads to denser film microstructures, which accounts for the film thickness reduction and index increase. We used infrared spectroscopy to monitor water and NH_3 removal in annealed films. Infrared transmission spectra of the films were measured with a Perkin-Elmer Spectrum 100 series spectrometer with a Universal diamond ATR attachment. Figure 6.2e plots the Fourier Transform InfraRed (FTIR) absorption spectra of the films. The peaks located at 1420 cm^{-1} and 1620 cm^{-1} are attributed to N-H stretching and -OH bending vibration, respectively [112], and the broad absorption band

from 3000 cm^{-1} to 3600 cm^{-1} is assigned to the stretching vibration of the hydrogen-bonded OH groups of the adsorbed water [112]. All absorption peaks progressively diminish as the annealing temperature increases, with the most significant peak height reduction occurring between 150 °C to 250 °C. While raising the annealing temperature to 300 °C does contribute to further removal of -OH and -NH species, X-ray diffraction analysis shows partial crystallization in films annealed at 300 °C, evidenced by the anatase phase [101] diffraction peak at 26° (Figure 6.2f). Therefore, we choose to a post-deposition annealing temperature of 250 °C based on these results. TiO_2 films prepared under this optimal annealing condition also exhibit a dense, defect-free microstructure and a low surface RMS roughness of (1.2 ± 0.2) nm confirmed by atomic force microscopy (AFM) surface morphology measurement (Figure 6.2g) and SEM cross-sectional imaging (Figure 6.2h). The high optical and structural quality of the films facilitates low-loss photonic device fabrication.

6.3 Flexible TiO_2 Photonic Devices

6.3.1 Fabrication Methods of Flexible TiO_2 Photonic Devices

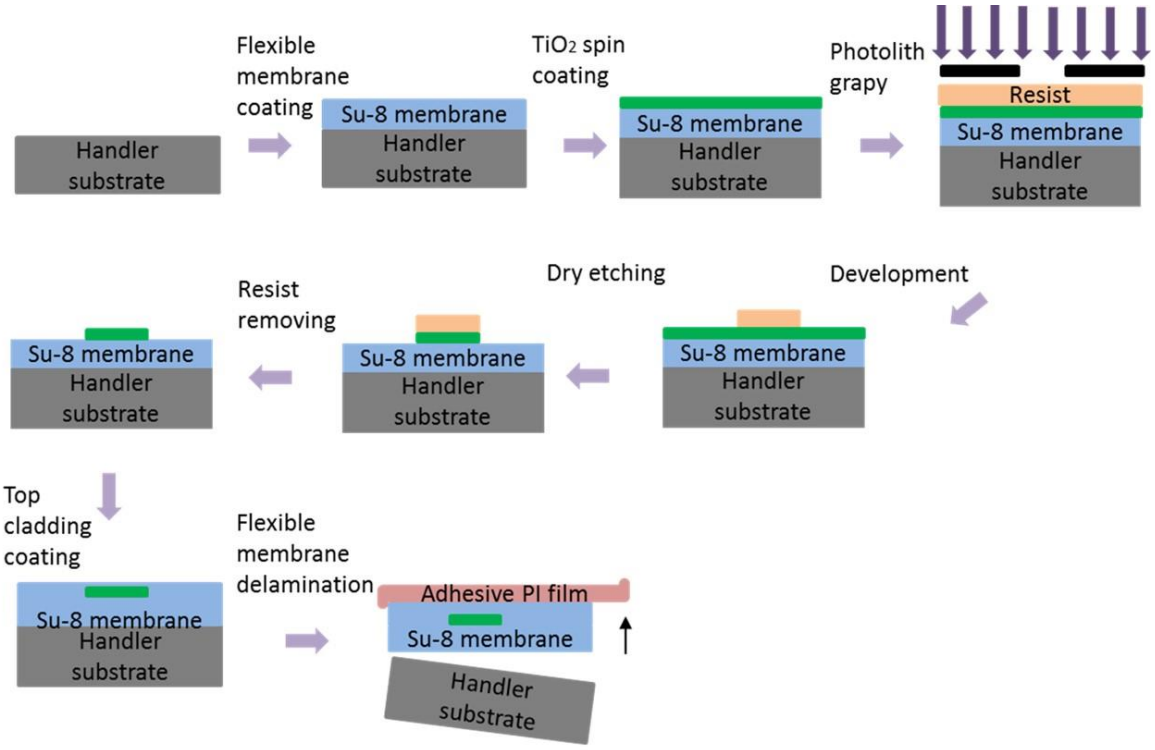

Figure 6.3 Schematic overview of the monolithic flexible photonic device fabrication process using dry-etching method.

We fabricated TiO_2 photonic devices following protocols illustrated in Figure 6.3, where we leverage established planar microfabrication technologies to monolithically integrate devices on unconventional flexible substrates. In the process, an oxidized silicon wafer serves as a handler substrate to provide mechanical support during device processing. The wafer is coated with a layer of SU-8 epoxy, on which the TiO_2 films are deposited using the sol-gel method described in the preceding section

and patterned into photonic structures. The lithography was performed on an i-line mask aligner with a negative photoresist (NR9-1000PY, Futurrex). The resist pattern was reflowed at 135 °C for 4 s on a hot plate after development to remove line edge roughness. Device patterns were transferred to the TiO_2 layer using Inductively Coupled Plasma (ICP) RIE in mixed CF_4, Ar and O_2 gases (volume ratio 16:4:3, total pressure 2 Pa) and at a microwave power of 500 W with 150 W bias. The etch rates of the resist and TiO_2 are 300 nm/min and 100 nm/min under the etching condition, respectively. This low etch selectivity, although sufficient for defining our rib waveguide geometry (Figure 6.4a), can be improved by using a hard mask when deep etch is required [114]. After etching, each the sample was sonicated in acetone to remove the remaining resist mask followed by another layer of SU-8 top cladding coating. Finally, the sample was cleaved along with the handler substrate to prepare waveguide facets and subsequently delaminated from the handler substrate using a Kapton tape to form free-standing flexible membrane devices. Figure 6.4a shows a top-view optical micrograph and an SEM cross-sectional image of a fabricated racetrack resonator.

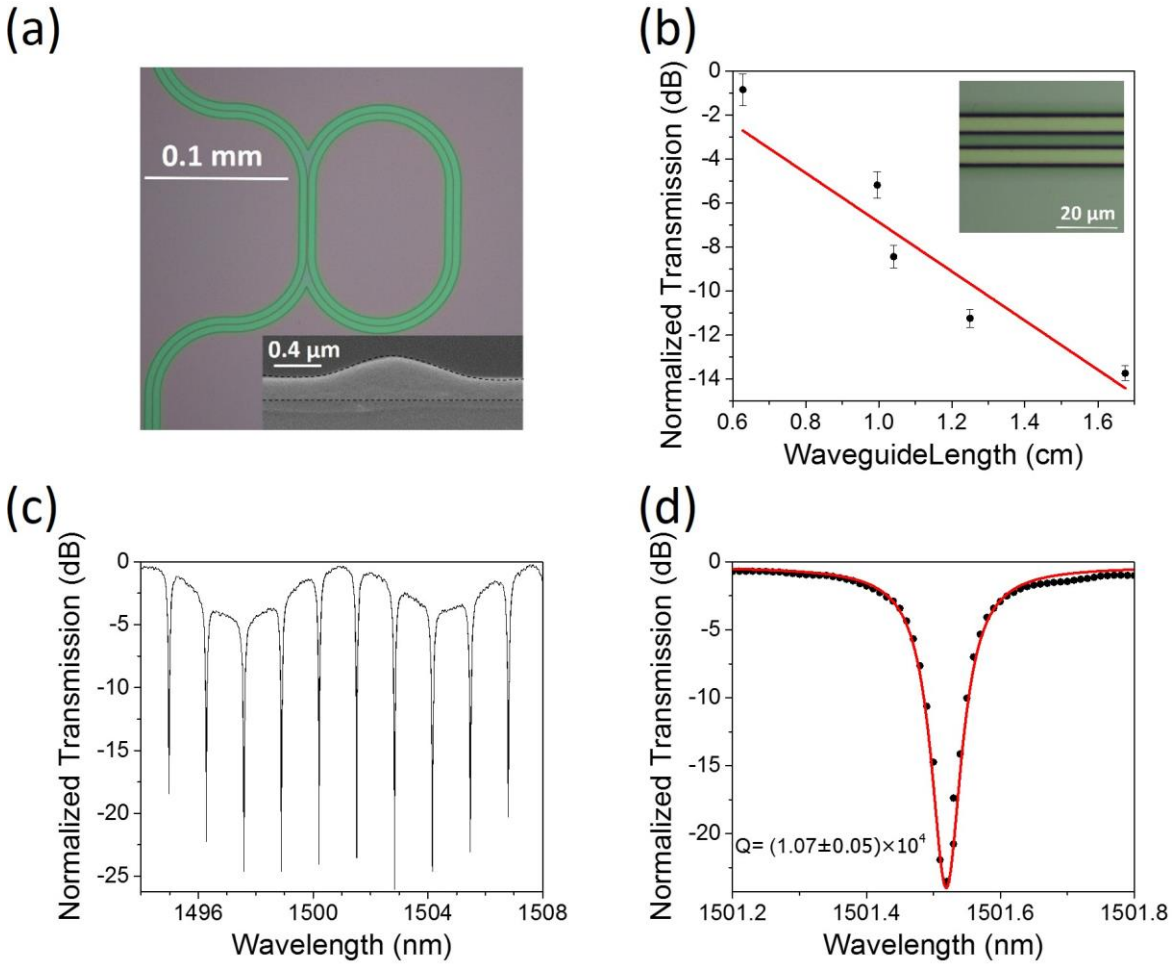

Figure 6.4 Flexible TiO_2 photonic device optical characterization. (a) Optical microscope top-view image of a TiO2 rib racetrack resonator. The inset shows the cross-sectional SEM image of the bus waveguide; (b) Cut-back loss measurement: transmitted optical power as a function of waveguide length at 1550 nm wavelength. The channel waveguide width is 4.7 µm and height is 0.2 µm. Inset shows an optical microscope image of a fabricated TiO_2 channel waveguide; (c, d) normalized optical transmission spectra of a TiO_2 rib racetrack resonator with a loaded Q-factor of $(1.07 \pm 0.05) \times 10^4$.

6.3.2 Optical Performance

The flexible TiO_2 waveguides and resonators were mounted on motion stages and characterized using the fiber end fire coupling method *in-situ* both in a "flat", undeformed state and when subjected to bending. The testing protocols are similar to what we used to characterize chalcogenide glass based flexible photonic devices. Propagation loss of the buried flat channel waveguides near 1550 nm wavelength was measured using the standard cut back method prior to delamination from the handler substrate. Insertion loss of waveguides of different lengths is plotted in Figure 6.4b, and the propagation loss is inferred from the slope to be (11 ± 2) dB/cm. Figure 6.4c and Figure 6.4d present a typical transmission spectrum of a flexible TiO_2 resonator. Using the coupled mode theory, an intrinsic Q-factor of 2×10^4 is fitted from the spectrum. The loss number and Q-factor are comparable to previously reported values in sol-gel devices: Park *et al.* measured a propagation loss of 15 dB/cm and an intrinsic Q-factor of 2×10^4 in TiO_2 WGM resonators near 1550 nm wavelength [110].

The losses result from both intrinsic and extrinsic contributions. Intrinsic losses are due to the absorption of NH and OH vibrations overtones in the NIR region and the Rayleigh scattering of possible micro-voids remaining in the sol-gel TiO_2 thin films [115]. Intrinsic material loss in the films was evaluated to be (3 ± 1) dB/cm at 1550 nm wavelength by slab mode propagation loss measurement on a Metricon 2010 prism coupler with a fiber bundle attachment. Therefore, extrinsic losses originating from scattering by discrete defects such as resist residue account for a large fraction of the observed waveguide loss, which can be mitigated through further lithography and etching process optimization. RMS surface roughness on the waveguides was quantified using AFM to be (1.4 ± 0.3) nm (Figure 6.5a) prior to top SU-8 cladding coating.

However, we also found scattered resist residues along the waveguides (Figure 6.5b), which likely account for the observed scattering loss.

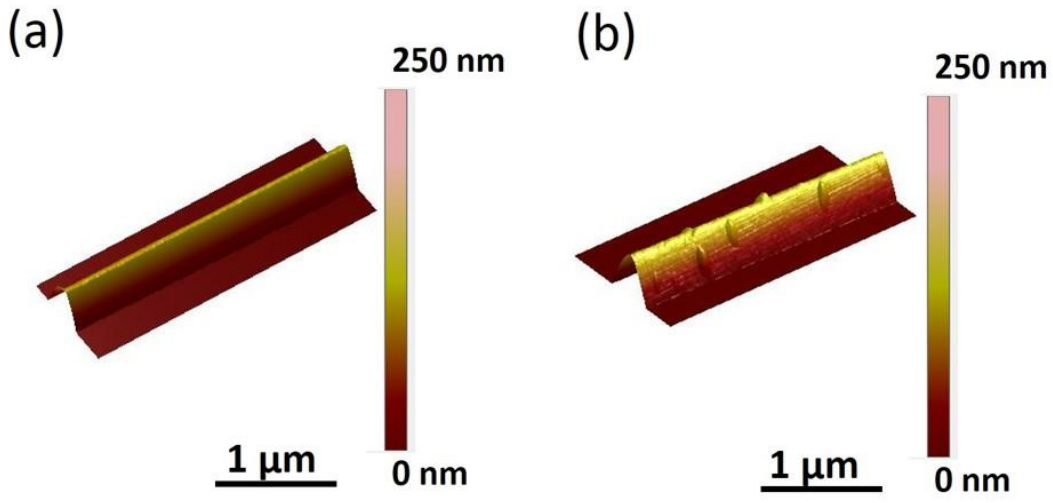

Figure 6.5 Surface morphology of TiO_2 rib waveguides by AFM: (a) A waveguide without resist residue; and (b) a waveguide with resist residue.

6.3.3 Mechanical Modeling and Testing

We have pioneered a multi-neutral-axis configurational design (in Chapter 4) that enables robust flexible photonic devices. This novel configuration leads to the emergence of multiple neutral axes in the laminates where the strains vanish. If photonic components are placed at these neutral axes then they can sustain large mechanical deformation without breaking or degradation. By adjusting the modulus and thickness of the layers, the locations of the neutral axes can be flexibly tuned across the stack to meet diverse application needs, a major advantage of our approach. Here we extend the basic design principle to demonstrate foldable photonics that can sustain repeated

bending with extremely small radius (R = 0.25 mm) on substrates approximately 0.1 mm thick. However, rather than using the multi-neutral-axis analytical theory we developed to model our devices, we resort to the finite element method (FEM) to compute strain distribution during mechanical deformation of the devices for two reasons. First, the extraordinary mechanical flexibility of our devices demonstrated here enables large deformation (R is only 2.5 times of d), and the assumptions underlying our prior analytical model do not necessarily hold in this large deformation regime. Second, the multi-neutral-axis theory does not take into account the embedded photonic device layer in the analysis. This assumption is valid when the devices consist of channel waveguides as shown in our previous report; nevertheless, rib waveguide structures introduce a continuous TiO_2 slab layer with much higher modulus compared to the surrounding polymers, which warrants further inspection of the analytical model.

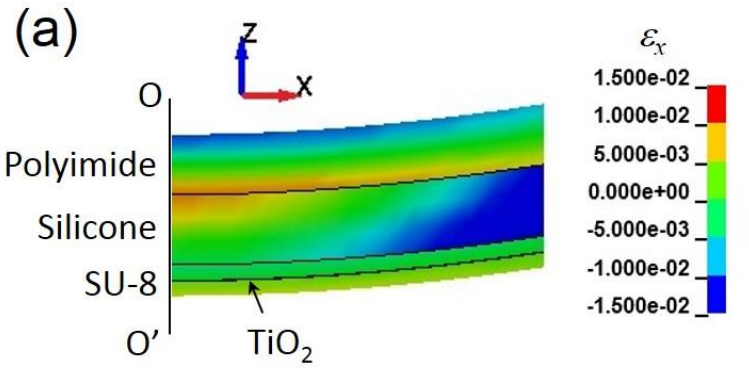
(a)
z
x
O
Polyimide
Silicone
SU-8
O'
TiO2
εx
1.500e-02
1.000e-02
5.000e-03
0.000e+00
-5.000e-03
-1.000e-02
-1.500e-02

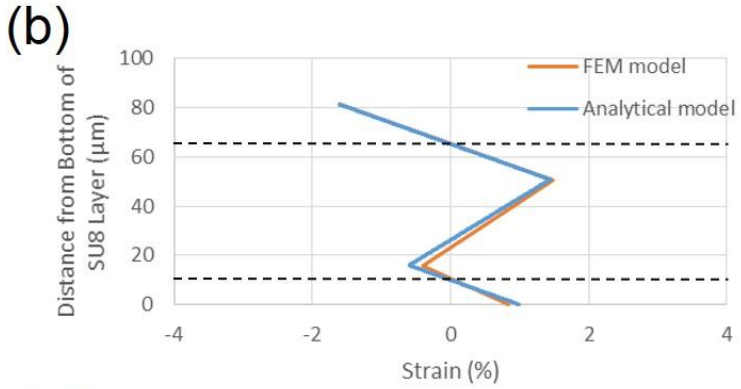
(b)
Distance from Bottom of SU8 Layer (μm)
FEM model
Analytical model
Strain (%)

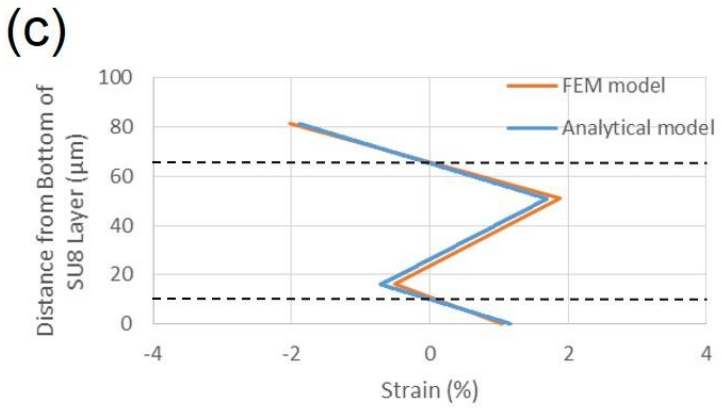
(c)
Distance from Bottom of SU8 Layer (μm)
FEM model
Analytical model
Strain (%)

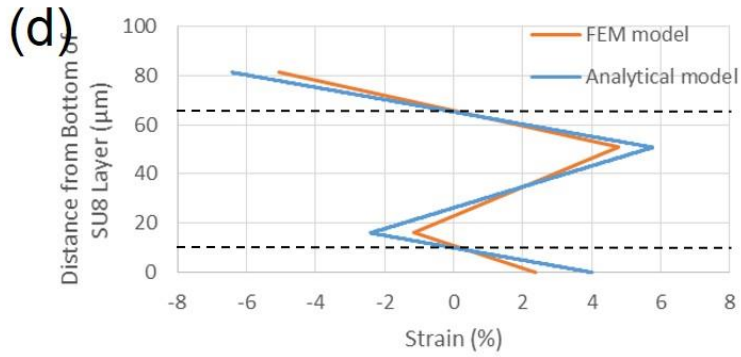
(d)
Distance from Bottom of SU8 Layer (μm)
FEM model
Analytical model
Strain (%)

Figure 6.6 Mechanical simulation. (a) Strain distribution in the laminated photonic chip structure during bending at R = 1 mm; (b)-(d) strain ε_x along the structure's center axis OO' calculated using FEM and the analytical multi-neutral-axis model: (b) R = 1 mm, (c) R = 0.85 mm, and (d) R = 0.25 mm. The black dotted lines mark the locations of the neutral axes in the polyimide and SU-8 layers.

The FEM model was created using the LS-DYNA solver. Details of the FEM model settings and the impact of the TiO_2 layer on strain distribution will be discussed later. Figure 6.6a plots the distribution of strain component ε_x when the flexible photonic chip is bent simulated by FEM, and Figures 6.6b-d compare the strain component ε_x along the center axis OO' calculated using FEM and the multi-neutral-axis analytical model [70] under bending radii of 1 mm, 0.85 mm, and 0.25 mm, respectively. For the relatively large bending radii (R) of 1 mm and 0.85 mm, the results from FEM and analytical methods are consistent. However, at R = 0.25 mm, the analytical model over-predicted the strain by up to 100% since the thickness reduction of each layer was not considered in the analytical model. Despite the large deviation of strain, we note that the analytical model still captures two critical features: strain distribution in the SU-8, polyimide and silicone layers remains linear across the thickness direction, an assumption of the multi-neutral-axis theory; and, more importantly, the laminated structures still exhibit neutral axes in the SU-8 and polyimide layers at locations coinciding with the analytical model predictions and independent of the bending radius. This interesting observation suggests that while our multi-neutral-axis theory overestimates strains inside a laminate under large deformation, it can still be practically applied to design compliant photonic and electronic devices with extraordinary flexibility by placing the device layer at the model-predicted neutral axis location, since

the zero strain condition at the device layer is not compromised even under large deformation.

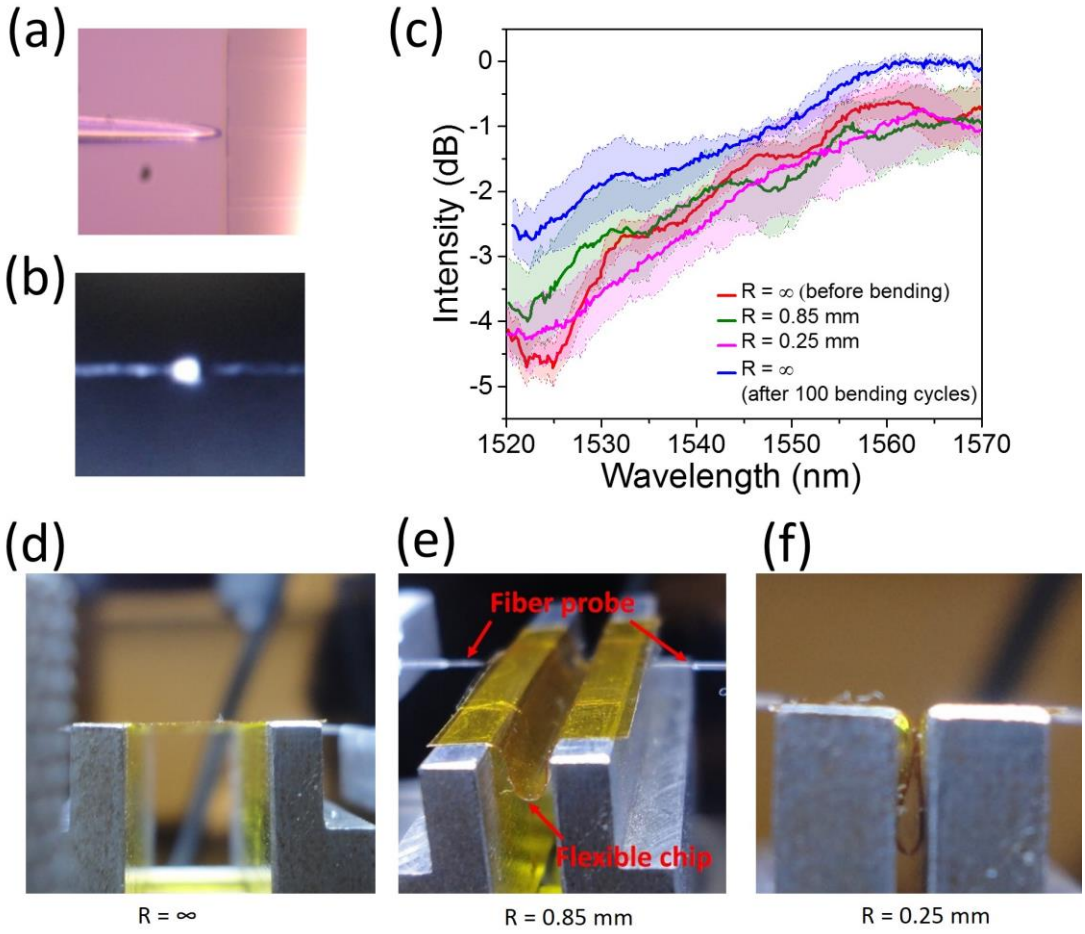

Figure 6.7 Mechanical tests of foldable TiO2 waveguides. (a) Optical microscope image of the input fiber coupled to a waveguide; (b) Far-field image of TE polarized mode output from a flexible TiO_2 waveguide; (c) Normalized optical transmission spectra of a flexible waveguide after bending at different radii; (d, e, f) Photos of the fiber butt coupling testing set-up for in-situ measurement of optical transmission characteristics at different bending radii.

Based on the modeling results, we fabricated flexible TiO_2 photonic devices by aligning the device layer with the model-predicted neutral axis locations. Figure 6.7a shows an optical image of the fiber coupled to an end facet of the flexible waveguides and Figure 6.7b presents a far-field image of the TE mode output from the waveguide. Figure 6.7c shows the transmission spectra of a flexible TiO_2 waveguide following the multi-neutral-axis configuration design. The solid lines correspond to average transmittance through the waveguide when it is undeformed, bent to different radii, and after 100 bending cycles at 0.25 mm radius. The shaded regions denote the standard deviation of waveguide transmittance due to coupling variation. The different colored shaded regions overlap, indicating minimal optical loss variation of the devices after the bending cycles. Structural integrity of the devices after bending was also confirmed via optical microscope inspection, and no cracks or delamination of the layers were observed. The result represents the best-in-class performance for flexible waveguide-based devices.

6.3.4 FEM Modelling Parameter Setting

In order to map strain distribution inside the bent flexible chip, eight-node solid elements were applied to all layers. Regarding the material models, the elastic material model [116] was applied to Polyimide, SU-8 and TiO_2. Silicone was treated as an incompressible hyperelastic solid and was characterized using the Blatz-Ko rubber model [116, 117], where the Poisson's ratio was fixed to the default value of 0.463. The detailed material parameters used in FEM simulation are summarized in Table 6.1.

Table 6.1 Materials parameters used in FEM simulation

Materials	Young's Modulus (GPa)	Density (g/cc)	Poisson ratio
Polyimide SU-8 TiO_2	2.5 2 147	1.42 1.12 3.82	0.34 0.22 0.50
Materials	Shear Modulus (MPa)	Density (g/cc)	Poisson ratio
Silicone	0.50	0.97	0.463

Using the FEM model, the effect of TiO_2 layer on deformation can be identified. Figure 6.8 compares the strain distributions along the centerline OO' in Figure 6.6a. The horizontal strain component (ε_x) in the polyimide and SU-8 layers are compared in Figure 6.8a-c for bending radii (R) of 1 mm, 0.85 mm, and 0.25 mm, respectively. In all cases, the TiO_2 layer decreased the compressive and tensile strains in both polyimide and SU-8 layers, and the decrease is most pronounced at R = 0.25 mm. Moreover, when the device was bent to the opposite direction (reverse bending shown in Figure 6.10), the presence of TiO_2 layer still decreases the strains in SU8 and polyimide layers in a similar manner. These results suggest that it is mandatory to include the TiO_2 layer (despite its small thickness compared to SU-8 and polyimide) in the FEM modeling to ensure accuracy of the result. The results presented in Figure 6.6 have incorporated the TiO_2 layer in the simulations.

Bending in the opposite direction (with the polyimide layer facing outwards) was also simulated, and the strain distributions are compared for both FEM and analytical models in Figure 6.9. At R = 1 mm and R = 0.85 mm, both models show good agreement. When R = 0.25 mm, the analytical model overestimates the strain. These results are consistent with our previous analysis (Figure 6.6).

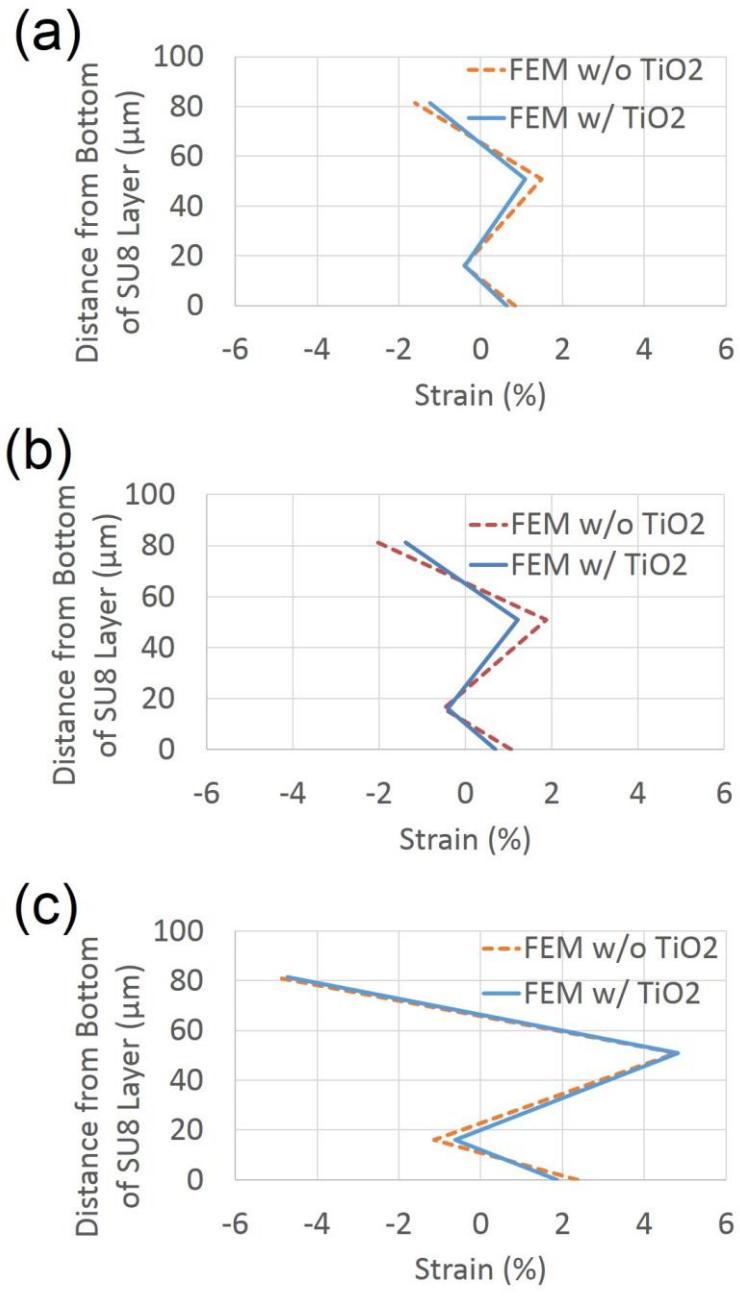

Figure 6.8 Comparison of ε_x along the OO' axis for the cases with TiO_2 and without TiO_2: (a) R = 1 mm, (b) R = 0.85 mm, and (c) R = 0.25 mm.

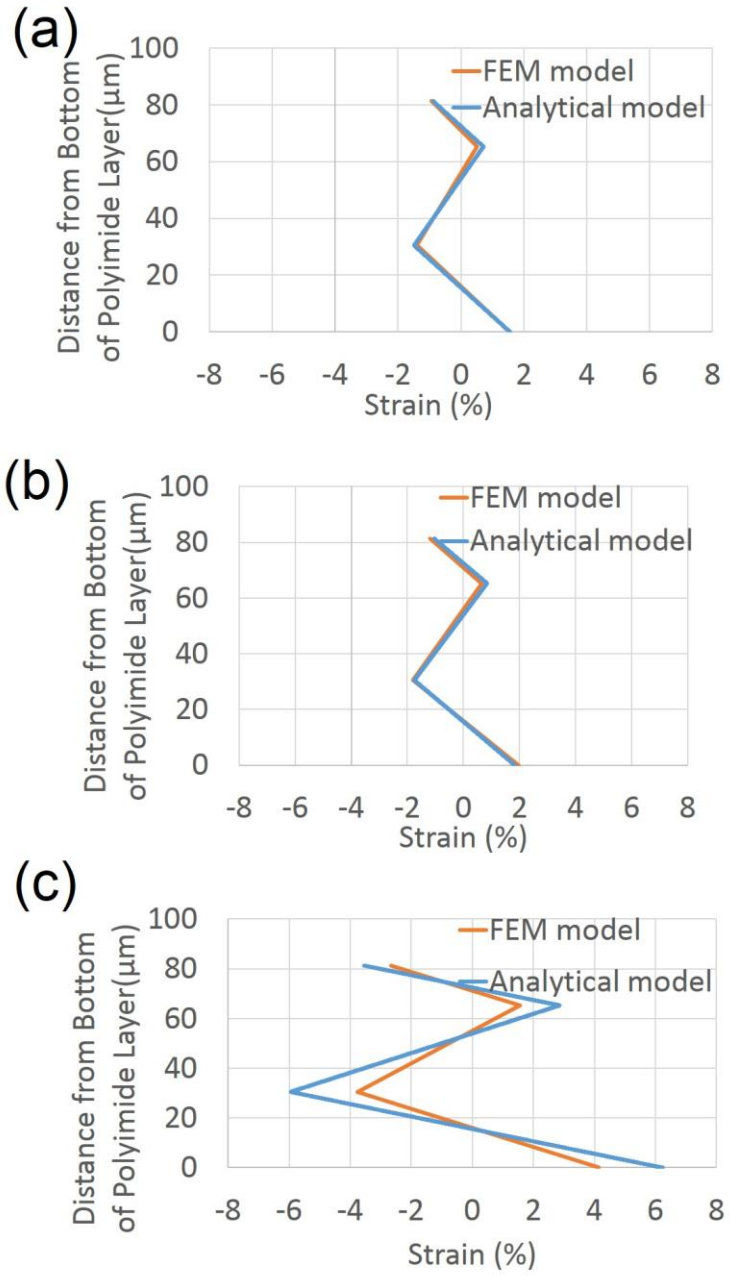

Figure 6.9 Strain ε_x along the structure's center axis OO' calculated using FEM and the analytical multi-neutral-axis model when the bending direction is reversed (reversed bending): (a) R = 1 mm, (b) R = 0.85 mm, and (c) R = 0.25 mm.

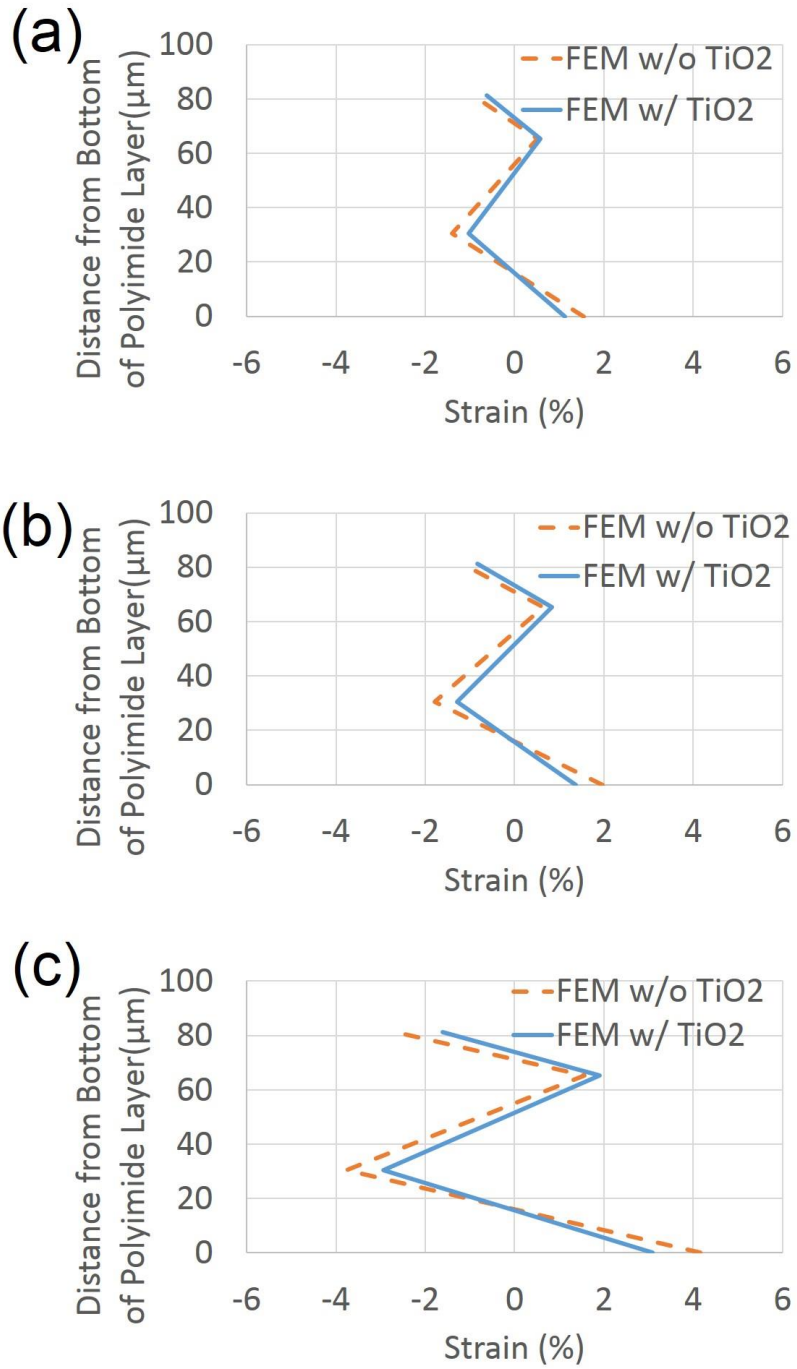

Figure 6.10 Comparison of ε_x along the OO' axis for the cases with TiO_2 and without TiO_2 (reversed bending): (a) R = 1 mm, (b) R = 0.85 mm, and (c) R = 0.25 mm.

6.3.5 Cytocompatibility

To assess the cytocompatibility of our sensor materials (SU-8 and TiO2), we cultured human mesenchymal stem cells (hMSCs) in proximity to and in direct contact with thin layers of each sensor material following established cell culture procedures [118, 119]. Thin films of TiO_2 were deposited on bare silicon wafer via the sol-gel process. SU-8 2002 photoresist was spin coated on select samples to simulate sensor encapsulation in SU-8. The samples were then cleaved and suspended in cell culture inserts above hMSCs cultured in a 12-well plate. Bare silicon wafer was also included in the study as an additional test substrate. Three chips of each sample were included in the study, and three empty trans-well membranes were included in control wells. As shown in Figure 6.11a, hMSCs proliferated over six days of the study, after which the cell monolayer became confluent, prohibiting further cell growth (Figure 6.12). On each day, no statistically significant difference was found between test samples and control groups. The metabolic activity of hMSCs increased significantly ($p < 0.01$) after the culture was initiated until cells reached confluence. By day 8, the average number of cells in all testing groups increased by approximately four folds from day 0, confirming that the SU-8 and TiO_2 films did not compromise the proliferative potential of hMSCs. When plated directly on the sensor materials, hMSCs attached, adopted a spindle-shaped morphology and maintained a high viability (Figure 6.11b-c) with little to no cell death. Collectively, our results confirmed the cytocompatibility of our sensor materials.

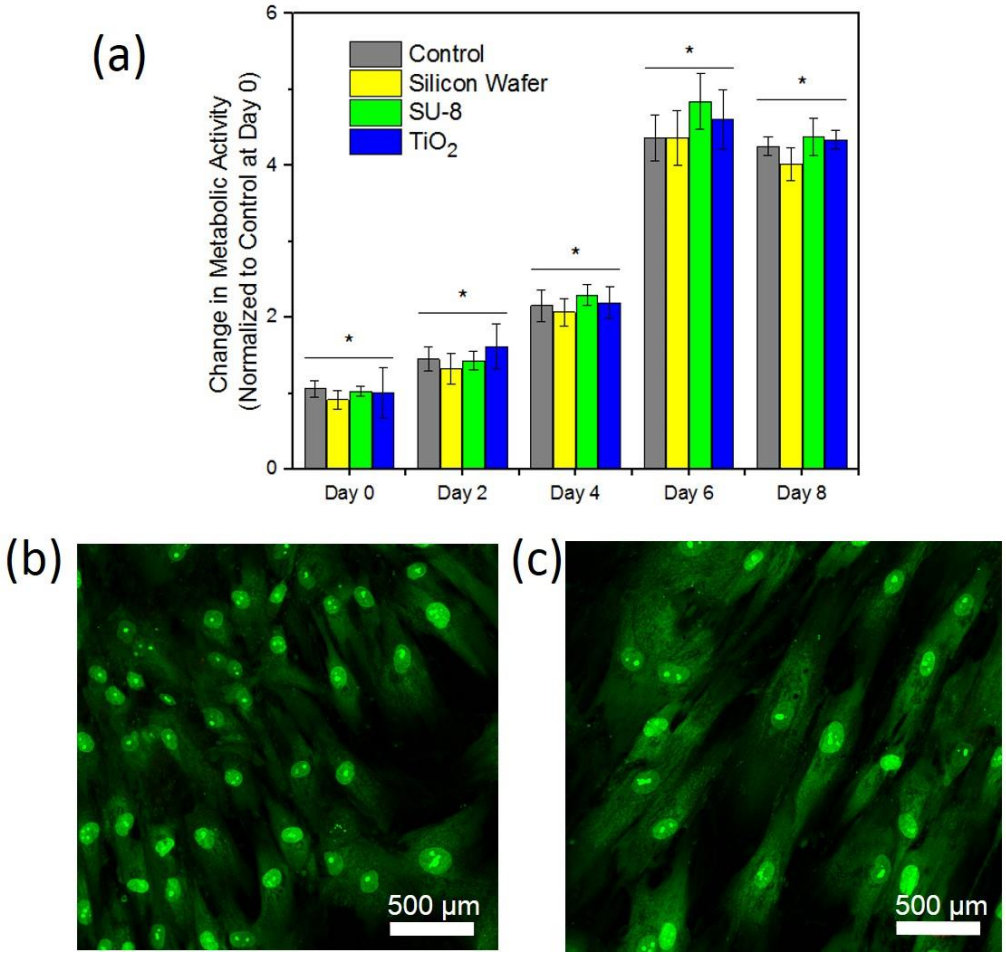

Figure 6.11 Analyses of cytocompatibility of the sensor materials. (a) Proliferation of hMSCs in indirect contact with sensor materials; (b-c) Confocal images of live/dead stained day 10 hMSCs cultured in direct contact with SU-8 (b); and TiO2 (c). Live cells were stained green and dead cells, if any, were stained red. *: significantly different ($p < 0.01$) from day 0-6. No significant difference was observed between day 6 and 8.

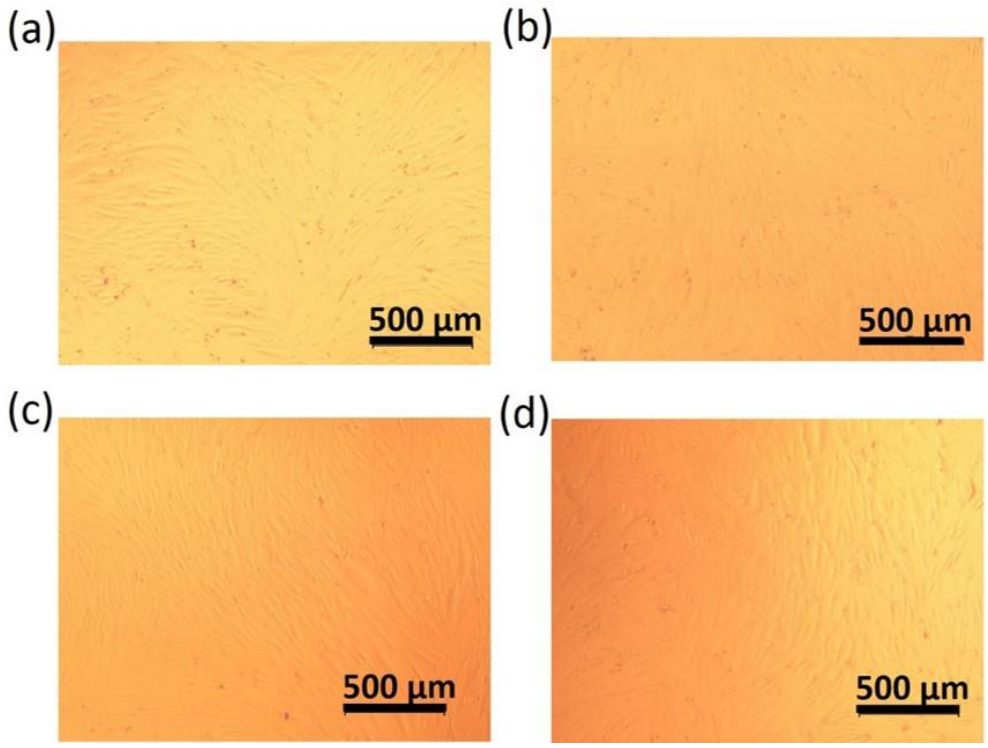

Figure 6.12 Phase contrast light microscope images indicating a confluent monolayer of hMSCs on day 8 of the cytotoxicity test with the sensor materials suspended on top of the cell layer. Here is the evidence of hMSC confluence in wells containing: (a) Tissue culture plastic control; (b) Bare silicon wafer; (c) TiO_2 thin films on silicon, and (d) SU-8 on TiO_2 thin films on silicon.

6.4 Summary

In this study, we demonstrated foldable and cytocompatible photonic devices based on sol-gel synthesized TiO_2 thin films. Our FEM mechanical modeling indicates that while the analytical multi-neutral-axis theory overestimates strain in the flexible chip structure under large bending deformation, it still precisely predicts the neutral axis location in the laminates. Therefore, we apply the configurational multi-neutral-axis design to experimentally demonstrate foldable photonic devices with extraordinary mechanical robustness that can sustain repeated bending at 0.25 mm bending radius.

The fabricated TiO_2 resonator devices exhibit an intrinsic Q-factor of 20,000. Low cytotoxicity of the sol-gel TiO_2 material is confirmed through cell proliferation tests, making it a promising platform for biophotonic applications.

Chapter 7

FUTURE WORK AND SUMMARY

7.1 Future Work

Future will work focus on the application of our developed approaches such as the integration of active photonic devices on flexible substrate. One application example here is the fully integrated photonic link on flexible substrates.

7.1.1 Introduction and Design Analysis [120, 121]

With the increasing demand for information commutation at a faster speed and lower power consumption, traditional copper wiring technology is quickly approaching its fundamental limit set forth by resistive power dissipation, RC delay, and cross talk. Integrated optical interconnects, which already dominate long-haul telecommunications, have emerged as a promising solution to the "interconnect bottleneck". The basic idea behind this is the high frequency of light, which enables a large bandwidth for transporting and managing a huge amount of information. Usually the electrical signal at high transmission rates (~100 MHz) would have a high attenuation (~ 5 dB/Km); while optical signals can operate in the wavelength range (It is usually in the range 0.5-2 μm, corresponding to light frequency from 600 THz to 150 THz, 10^6 times the frequency used in electrical transmission) where devices materials are highly transparent to decrease the propagation loss. According to the ITRS Roadmap, the total on/off chip data I/O is projected to reach 100 Tb/s at the 9 nm node, far exceeding the capacity that can be possibly reached using current copper wiring technology. Optical

interconnects have been intensively investigated as a potential solution to resolve this "interconnect bottleneck". The solutions typically involve on-chip edge-view active components coupled to optical fiber bundles [122], [123] or surface mount VCSELs and detectors vertically integrated with on-board multi-mode waveguides [124], [125]. Both approaches, however, are not scalable to high bandwidth density due to chip geometry constraints. For example, given an edge-coupled waveguide pitch of 100 μm and a single channel bandwidth of 20 Gb/s, the aggregate off-chip bandwidth is limited to 10 Tb/s for a 2.5 cm by 2.5 cm chip (assuming all four chip edges are used for coupling with the waveguides and no wavelength division multiplexing is implemented). New solutions scalable to the 10 Tb/s regime and beyond is thus mandated to resolve the chip-to-chip interconnect challenge, and several innovative interconnect designs are currently being investigated, such as multi-core fiber interconnects [126], optical printed circuit boards [127], [128], silicon photonics [129], [130], and hybrid approaches [131-136]. Thus we propose and analyze a new chip-to-chip interconnect scheme based on a flexible photonics platform we developed (Figure 7.1). We show that our design offers scalable high bandwidth density and potentially enables a simplified packaging solution without involving optical alignment.

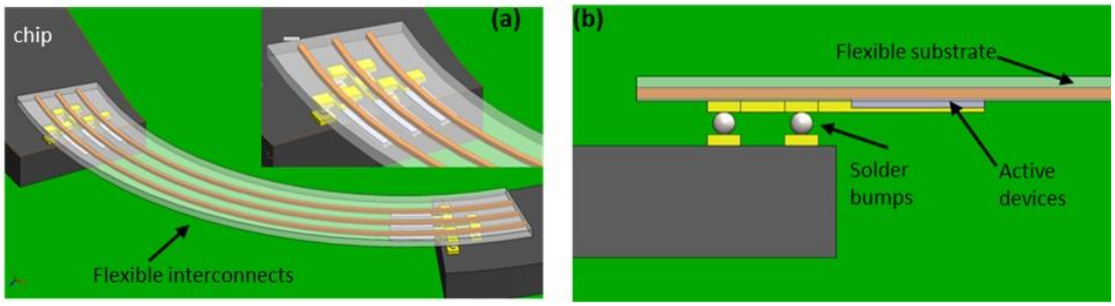

Figure 7.1 The fully-integrated flexible optical interconnect design: (a) Schematic tilted view of a flexible optical link bonded to a chip; (b) Cross-sectional structure of the optical link.

Figure 7.1 schematically illustrates the interconnect design. The interconnect architecture builds on a flexible planar photonic link, which consists of an array of single-mode glass optical waveguides on a common flexible substrate as well as active optoelectronic components (lasers and detectors) bonded onto the flexible substrate and optically coupled to the waveguides. The active devices based on an alignment-free die-to-wafer bonding process [137-139] and are directly coupled to the waveguides. Two ends of the flexible link is flip-chip bonded and electrically connected to chips through solder bumps and on-chip metal vias, which also serve as effective heat conduction channels between the active devices and the chip. The flexible link interconnects present several unique advantages for chip packaging, such as simplified packaging, large bandwidth density, and low power consumption [120]. Stringent alignment accuracy is often cited as the main argument against the use of single-mode waveguides; however, our interconnect link is embedded in polymer substrate, providing enough flexibility for the misalignment between chips surface-mounted on carriers or on a printed circuit board. Besides, no optical alignment is required since the optical link only interfaces with the chips electronically. Figure 7.1b shows the cross section structure of the optical

link. Specifically, the active devices are directly coupled to the waveguides based on an alignment-free die-to-wafer bonding process. And the active dies can be thinned down to a small thickness (< 25 μm) to achieve both the evanescently coupling and low-profile bonding, providing an enough height space for the electronic connection of flexible interconnects through a flip-chip bonding process [120].

Table 7.1 Bandwidth scalability of our flexible optical interconnect platform as compared to other competing optical interconnect technologies.

Technology	Waveguide pitch (μm)	Total I/O channel #	Aggregate data rate (Tb/s)
Flexible optical interconnect	10	5,000	100
Polymer optical fiber ribbons [123]	250	200	4
Multi-mode on-board waveguides [124, 140]	62.5	800	16
Multi-mode off-board waveguides [6, 141]	200	250	5

As shown in Figure 7.1, the interconnect bandwidth density will only be limited by the physical size of on-chip contact pads and solder bumps. Specifically, the bandwidth density can be dramatically increased by arranging the on-chip contact pads in 2-D arrays. In addition, the use of high-index-contrast single-mode waveguides for optical interconnects also contributes to high-density integration. To more clearly present our approach's bandwidth salability benefit, we compare the possibly attainable aggregate bandwidths of several interconnect solutions in Table 7.1. We assume: 1) a bonding pad pitch of 100 μm which is readily achievable using flip chip bonding [142];

2) 10 Gb/s single channel data rate; 3) 2.5 cm × 2.5 cm chip size; 4) all four chip edges are used for interconnects. It is apparent that the bandwidth density of traditional 1-D edge-coupling optical interconnect schemes are limited by the physical size of the chip to < 20 Tb/s, while our approach enables off-chip I/O bandwidth scalable to 100 Tb/s which sufficiently accommodates the interconnect bandwidth need at 9 nm CMOS node [120].

Table 7.2 Optical loss budget (in dB) of the flexible interconnect platform (projected) and typical VCSEL-based multi-mode optical links.

Loss mechanisms	Flexible single-mode photonics	VCSEL-based multi-mode optics
Laser-to-waveguide coupling loss	0	1.1 [143]
Modulator insertion loss	1 [144]	0
Waveguide-to-PD coupling loss	0.5 [145]	1.1 [143]
Waveguide propagation loss	4 [146]	0
Extinction ratio penalty	3	3
Margin	4	4
Total	12.5	9.2

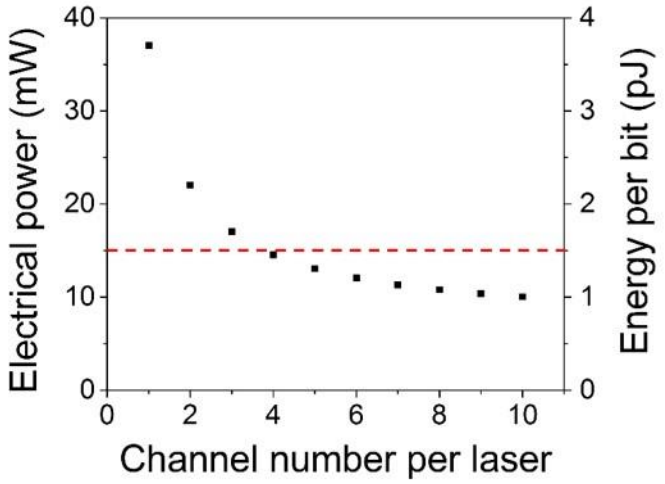

Figure 7.2 Single channel electrical power consumption of the flexible optical link: the horizontal axis denotes the number of channels sharing a single bonded laser. The dotted line indicates the single-channel electrical power consumption of VCSEL-based multi-mode optical links. The assumptions are: 1) 10 Gb/s single-channel data rate; 2) each channel is individually encoded using a modulator with 100 fJ/bit power consumption; 3) receiver sensitivity is -18 dBm; and 4) the bonded laser has a threshold power of 30 mW and 4% slope efficiency [147].

In addition to these packaging benefits and large bandwidth density, the flexible interconnect platform also offers low power consumption comparable or even superior to that of high-performance VCSEL-based links. Table 7.2 compares the estimated optical loss budget of our technology with that of VCSEL-based multi-mode optics which includes the three current technology platforms listed in Table 7.1. The numbers listed in the table are based on values previously reported in literature. Since the evanescent lasers used in the flexible photonic links are waveguide coupled, the laser-waveguide coupling loss vanishes as it becomes part of the laser efficiency. These numbers indicate comparable optical loss for both types of interconnect links and support a low power laser source owing to high sensitivity of modern receivers

(typically better than -18 dBm at 10 Gb/s [148]. In our case, the required output optical power of a continuous-wave (CW) bonded laser is - 5.5 dBm so laser power consumption is currently dominated by relatively large threshold power (~ 30 mW [147]) due to less mature fabrication processes. Certainly the hybrid laser integration technology is still much less developed to date compared to VCSELs and significant improvements are thus expected by design and processing optimization. On the other hand, most VCSELs are directly modulated because of its surface emitting configuration. A VCSEL has to be pumped to high output power in order to be modulated at a high data rate of 10 Gb/s. Direct modulation of a state-of-the-art VCSEL at 10 Gb/s typically requires ~ 15 mW [149] laser power. Figure 7.2 compares the single channel power consumption at 10 Gb/s for our technology and that of VCSEL-based links. Since our approach employs external modulators, using a single bonded laser for different channels will further reduce the power consumption, which largely mitigates the high threshold power issue plaguing bonded lasers. In addition, when considering the electrical circuits driving the optical devices, our approach has significant advantage in power consumption because the electro-absorption modulators (equivalent to reverse-biased diodes) used in this case requires much lower power driver circuits compared to VCSEL's driver circuits which switch at very high current levels. The overall link power consumption is thus expected to be lower in our approach than in the VCSEL approach [120].

7.1.2 Experiment Proposal

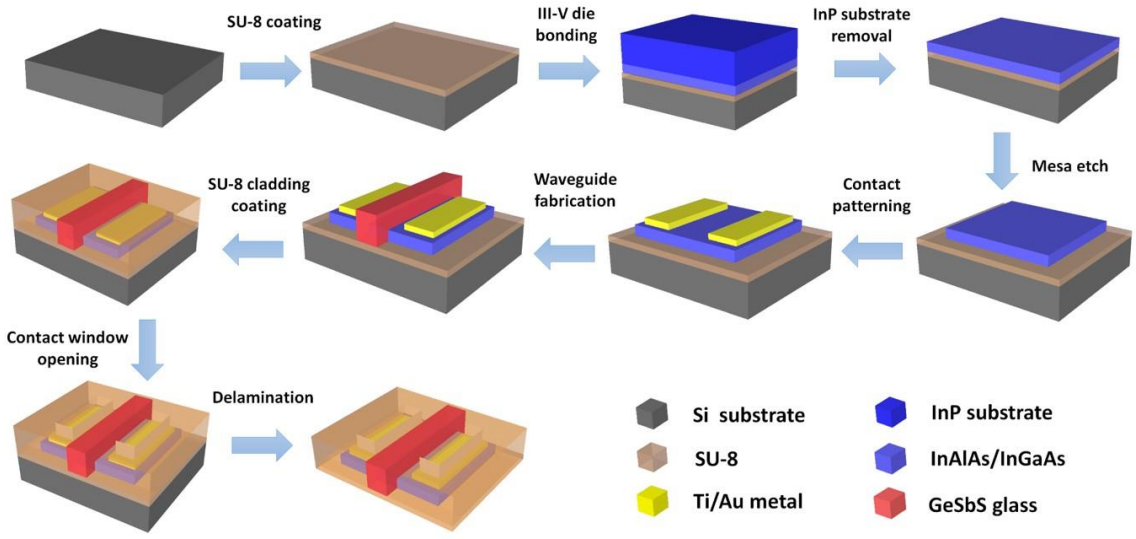

Figure 7.3 Schematic overview of the waveguide integrated photodetector fabrication process.

Figure 7.3 indicates one example of our experiment fabrication process for the integration of active devices on flexible substrates. Waveguide integrated photodetector would be the first demonstration of this designed approach. We adopted an adhesive die bonding process for active component integration on flexible substrates. Since the bonding process use unpatterned III-V semiconductor die rather than fabricated III-V active devices, no alignment is required in the bonding step. The III-V active layers are patterned to form active components only after bonding, substrate removal. The alignment of the III-V patterns to the glass waveguides above is guaranteed in the e-beam lithography process. After glass waveguide fabrication, a thin top cladding polymer layer was spin coated on top of the waveguides to serve both as a top protective cladding.

So my future work will focus on the optimization of the fabricatio process for waveguide integrated photodetectors with good performance. Besides, demonstration on the integration of lasers with passive waveguides would also try to be completed so that we can prove a full optical link with both light sources and detectors on flexible substates, which is not only useful for optical communication, but also for on-chip sensing application in all kinds of fields.

7.2 Summary

In this thesis, we first demonstrate monolithic photonic integration on plastic substrates using high-refractive index chalcogenide glass (ChG) materials. This process yields high-index-contrast nanophotonic devices with record optical performance and benefits significantly from improved processing protocols based on simple, low-cost contact lithography. We show that this versatile monolithic process can be readily adapted to different glass compositions with tailored optical properties to meet different candidate applications. To study the mechanical properties of the flexibe photonic devise, a novel multi-neutral-axis design is implemented to render the structure highly mechanically flexible, enabling repeated bending of the devices down to sub-millimeter bending radius without measurable optical performance degradation. We note that the classical multilayer beam bending theory fails in our design due to the large modulus contrast among different layers. For this reason a new analytical model accounting for the multiple neutral axes in a multilayer stack was then developed to successfully capture the strain-optical coupling behavior in our devices. We have further validated a SU-8 planarization and exploited the monolithic integration approach for 3-D multilayer fabrication. In addition, sol-gel synthesized TiO_2 for the fabrication of flexible and cytocompatible biophotonic devices was also included as my thesis work for its

potential application in wearable sensing and some specific fields of biology. Last but not the least, adhesive bonding process for III-V active photonic integration on the flexible substrates was also presented and would continue to be studied. These results pave the path towards the demonstration of a novel planar, flexible optical interconnect platform with fully-integrated optoelectronic functionalities.

REFERENCES

1. Lifante, G., *Introduction to Integrated Photonics*, in *Integrated Photonics: Fundamentals*. 2005, John Wiley & Sons, Ltd. p. 1-4.
2. Kim, D.H., et al., *Stretchable and foldable silicon integrated circuits.* Science, 2008. **320**(5875): p. 507-511.
3. Zhou, W.D., et al., *Flexible photonic-crystal Fano filters based on transferred semiconductor nanomembranes.* Journal of Physics D: Applied Physics, 2009. **42**(23): p. 234007.
4. Ko, H.C., et al., *A hemispherical electronic eye camera based on compressible silicon optoelectronics.* Nature, 2008. **454**(7205): p. 748-753.
5. Bosman, E., et al., *Highly Reliable Flexible Active Optical Links.* Ieee Photonics Technology Letters, 2010. **22**(5): p. 287-289.
6. Shibata, T. and A. Takahashi. *Flexible opto-electronic circuit board for in-device interconnection*. in *Electronic Components and Technology Conference, 2008. ECTC 2008. 58th*. 2008. IEEE.
7. Kim, D.H., et al., *Epidermal Electronics.* Science, 2011. **333**(6044): p. 838-843.
8. Ma, Z.Q., *An Electronic Second Skin.* Science, 2011. **333**(6044): p. 830-831.
9. Yang, W.Q., et al., *Large-area InP-based crystalline nanomembrane flexible photodetectors.* Applied Physics Letters, 2010. **96**(12).
10. Yoon, J., et al., *Ultrathin silicon solar microcells for semitransparent, mechanically flexible and microconcentrator module designs.* Nature Materials, 2008. **7**(11): p. 907-915.
11. Lee, H.M., et al., *Transparent and flexible amorphous In-Si-O films for flexible organic solar cells.* Applied Physics Letters, 2013. **102**(2).
12. Chou, C.H., J.K. Chuang, and F.C. Chen, *High-Performance Flexible Waveguiding Photovoltaics.* Scientific Reports, 2013. **3**: p. 2244.
13. Hosseini, P., C.D. Wright, and H. Bhaskaran, *An optoelectronic framework enabled by low-dimensional phase-change films.* Nature, 2014. **511**(7508): p. 206-211.
14. Vosgueritchian, M., J.B.H. Tok, and Z. Bao, *Stretchable LEDs: Light-emitting electronic skin.* Nat Photon, 2013. **7**(10): p. 769-771.
15. White, M.S., et al., *Ultrathin, highly flexible and stretchable PLEDs.* Nature Photonics, 2013. **7**(10): p. 811-816.
16. Chen, Y., H. Li, and M. Li, *Flexible and tunable silicon photonic circuits on plastic substrates.* Scientific Reports, 2012. **2**.

17. Zhou, W.D., et al., *Flexible photonic-crystal Fano filters based on transferred semiconductor nanomembranes.* Journal of Physics D-Applied Physics, 2009. **42**(23).
18. Fan, L., et al., *Direct fabrication of silicon photonic devices on a flexible platform and its application for strain sensing.* Optics Express, 2012. **20**(18): p. 20564-75.
19. Choi, C.C., et al., *Flexible optical waveguide film fabrications and optoelectronic devices integration for fully embedded board-level optical interconnects.* Journal of Lightwave Technology, 2004. **22**(9): p. 2168-2176.
20. Huang, Y.Y., et al., *Fabrication and replication of polymer integrated optical devices using electron-beam lithography and soft lithography.* Journal of Physical Chemistry B, 2004. **108**(25): p. 8606-8613.
21. Paloczi, G.T., Y. Huang, and A. Yariv, *Free-standing all-polymer microring resonator optical filter.* Electronics Letters, 2003. **39**(23): p. 1650-1.
22. Kim, K.-J., J.-K. Seo, and M.-C. Oh, *Strain induced tunable wavelength filters based on flexible polymer waveguide Bragg reflector.* Opt. Express, 2008. **16**(3): p. 1423-1430.
23. Lu, T.W., et al., *One-dimensional photonic crystal nanobeam lasers on a flexible substrate.* Applied Physics Letters, 2011. **99**(7).
24. Clark, J. and G. Lanzani, *Organic photonics for communications.* Nat Photon, 2010. **4**(7): p. 438-446.
25. Kim, K.-J., et al., *Flexible polymer waveguide tunable lasers.* Optics Express, 2010. **18**(8): p. 8392-8399.
26. Song, H.-C., et al., *Flexible low-voltage electro-optic polymer modulators.* Applied Physics Letters, 2003. **82**(25): p. 4432-4434.
27. Rogers, J.A., M.G. Lagally, and R.G. Nuzzo, *Synthesis, assembly and applications of semiconductor nanomembranes.* Nature, 2011. **477**(7362): p. 45-53.
28. Novoselov, K.S., et al., *Two-dimensional atomic crystals.* Proceedings of the National Academy of Sciences of the United States of America, 2005. **102**(30): p. 10451-10453.
29. Ma, Z., et al., *Fast Flexible Electronics Based on Printable Thin Mono-Crystalline Silicon.* ECS Transactions, 2011. **34**(1): p. 137-142.
30. Yamane, M. and Y. Asahara, *Glasses for photonics*. 2000: Cambridge University Press.
31. Righini, G.C. and A. Chiappini, *Glass optical waveguides: a review of fabrication techniques.* Optical Engineering, 2014. **53**(7): p. 071819-071819.
32. Hu, J.J., et al., *Flexible integrated photonics: where materials, mechanics and optics meet [Invited]*. Optical Materials Express, 2013. **3**(9): p. 1313-1331.
33. Kwak, K., K. Cho, and S. Kim, *Stable Bending Performance of Flexible Organic Light-Emitting Diodes Using IZO Anodes.* Scientific Reports, 2013. **3**: p. 2787.

34. Park, S., et al., *Flexible molecular-scale electronic devices.* Nature Nanotechnology, 2012. **7**(7): p. 438-442.
35. Munzenrieder, N., et al. *Flexible a-IGZO TFT amplifier fabricated on a free standing polyimide foil operating at 1.2 MHz while bent to a radius of 5 mm*. in *Electron Devices Meeting (IEDM), 2012 IEEE International*. 2012.
36. El-Kady, M.F., et al., *Laser Scribing of High-Performance and Flexible Graphene-Based Electrochemical Capacitors.* Science, 2012. **335**(6074): p. 1326-1330.
37. Jong-Hyun, A., et al., *High-speed mechanically flexible single-crystal silicon thin-film transistors on plastic substrates.* Electron Device Letters, IEEE, 2006. **27**(6): p. 460-462.
38. Ishizaki, K., et al., *Realization of three-dimensional guiding of photons in photonic crystals.* Nature Photonics, 2013. **7**(2): p. 133-137.
39. Aoki, K., et al., *Microassembly of semiconductor three-dimensional photonic crystals.* Nature Materials, 2003. **2**(2): p. 117-121.
40. Koonath, P. and B. Jalali, *Multilayer 3-D photonics in silicon.* Optics Express, 2007. **15**(20): p. 12686-12691.
41. Sherwood-Droz, N. and M. Lipson, *Scalable 3D dense integration of photonics on bulk silicon.* Optics Express, 2011. **19**(18): p. 17758-17765.
42. Li, L., et al., *Foldable and Cytocompatible Sol-gel TiO2 Photonics.* Scientific Reports, 2015. **5**.
43. *National Photonics Initiative Report* Available from: http://www.lightourfuture.org/.
44. Polikov, V.S., P.A. Tresco, and W.M. Reichert, *Response of brain tissue to chronically implanted neural electrodes.* Journal of Neuroscience Methods, 2005. **148**(1): p. 1-18.
45. Bettotti, P., *Hybrid Materials for Integrated Photonics.* Advances in Optics, 2014: p. 24.
46. Parker, S.T., et al., *Biocompatible Silk Printed Optical Waveguides.* Advanced Materials, 2009. **21**(23): p. 2411-2415.
47. Manocchi, A.K., et al., *Facile Fabrication of Gelatin-Based Biopolymeric Optical Waveguides.* Biotechnology and Bioengineering, 2009. **103**(4): p. 725-732.
48. Jain, A., A.H.J. Yang, and D. Erickson, *Gel-based optical waveguides with live cell encapsulation and integrated microfluidics.* Optics Letters, 2012. **37**(9): p. 1472-1474.
49. Xu, X.C., et al., *Stamp printing of silicon-nanomembrane-based photonic devices onto flexible substrates with a suspended configuration.* Optics Letters, 2012. **37**(6): p. 1020-1022.
50. Zablocki, M.J., et al., *Nanomembrane transfer process for intricate photonic device applications.* Optics Letters, 2011. **36**(1): p. 58-60.
51. Chen, Y., H. Li, and M. Li, *Flexible and tunable silicon photonic circuits on plastic substrates.* Scientific Reports 2012. **2**.

52. Hwang, S.-W., et al., *Dissolution Chemistry and Biocompatibility of Single-Crystalline Silicon Nanomembranes and Associated Materials for Transient Electronics.* ACS Nano, 2014. **8**(6): p. 5843-5851.
53. Dagdeviren, C., et al., *Conformal piezoelectric energy harvesting and storage from motions of the heart, lung, and diaphragm.* Proceedings of the National Academy of Sciences, 2014. **111**(5): p. 1927-1932.
54. Fujie, T., et al., *Engineered Nanomembranes for Directing Cellular Organization Toward Flexible Biodevices.* Nano Letters, 2013. **13**(7): p. 3185-3192.
55. Xiaochuan, X., et al. *Stamp printing of silicon nanomembrane based flexible photonic devices*. in *Lasers and Electro-Optics (CLEO), 2012 Conference on*. 2012.
56. Meitl, M.A., et al., *Transfer printing by kinetic control of adhesion to an elastomeric stamp.* Nat Mater, 2006. **5**(1): p. 33-38.
57. Ghaffari, A., et al., *Transfer of micro and nano-photonic silicon nanomembrane waveguide devices on flexible substrates.* Optics Express, 2010. **18**(19): p. 20086-20095.
58. Weidong, Z., et al. *Semiconductor nanomembranes for integrated and flexible photonics*. in *Information Photonics (IP), 2011 ICO International Conference on*. 2011.
59. Chanda, D., et al., *Large-area flexible 3D optical negative index metamaterial formed by nanotransfer printing.* Nat Nano, 2011. **6**(7): p. 402-407.
60. Hines, D.R., et al., *Transfer printing methods for the fabrication of flexible organic electronics.* Journal of Applied Physics, 2007. **101**(2): p. 024503.
61. Yuan, H.-C., et al. *Silicon-based nanomembrane materials: the ultimate in strain engineering*. in *Silicon Monolithic Integrated Circuits in RF Systems, 2006. Digest of Papers. 2006 Topical Meeting on*. 2006.
62. Yuan, H.-C. and Z. Ma, *Microwave thin-film transistors using Si nanomembranes on flexible polymer substrate.* Applied Physics Letters, 2006. **89**(21): p. 212105.
63. Yuan, H.-C., G.K. Celler, and Z. Ma, *7.8-GHz flexible thin-film transistors on a low-temperature plastic substrate.* Journal of Applied Physics, 2007. **102**(3): p. 034501.
64. Zhou, H., et al., *Fast flexible electronics with strained silicon nanomembranes.* Scientific Reports, 2013. **3**: p. 1291.
65. Sun, L., et al., *12-GHz Thin-Film Transistors on Transferrable Silicon Nanomembranes for High-Performance Flexible Electronics.* Small, 2010. **6**(22): p. 2553-2557.
66. Kan, Z., et al., *Fast flexible electronics using transferrable silicon nanomembranes.* Journal of Physics D: Applied Physics, 2012. **45**(14): p. 143001.

67. Shelley, A.S. and G.L. Max, *Elastically strain-sharing nanomembranes: flexible and transferable strained silicon and silicon–germanium alloys.* Journal of Physics D: Applied Physics, 2007. **40**(4): p. R75.
68. Kim, D.-H., et al., *Materials for multifunctional balloon catheters with capabilities in cardiac electrophysiological mapping and ablation therapy.* Nat Mater, 2011. **10**(4): p. 316-323.
69. Kim, D.-H. and J.A. Rogers, *Stretchable Electronics: Materials Strategies and Devices.* Advanced Materials, 2008. **20**(24): p. 4887-4892.
70. Li, L., et al., *Integrated flexible chalcogenide glass photonic devices.* Nat Photon, 2014. **8**(8): p. 643-649.
71. Zou, Y., et al., *Solution Processing and Resist-Free Nanoimprint Fabrication of Thin Film Chalcogenide Glass Devices: Inorganic–Organic Hybrid Photonic Integration.* Advanced Optical Materials, 2014: p. n/a-n/a.
72. Aksu, S., et al., *Flexible Plasmonics on Unconventional and Nonplanar Substrates.* Advanced Materials, 2011. **23**(38): p. 4422-4430.
73. Musgraves, J.D., et al., *Chalcogenide Glass Thin-Film and Fiber Structures for Chemical and Biological Sensing*, in *Amorphous Chalcogenides*. 2014, Pan Stanford Publishing. p. 203-269.
74. Melloni, A., et al. *Waveguide index contrast: implications for passive integrated optical components*. in *Fibres and Optical Passive Components, 2005. Proceedings of 2005 IEEE/LEOS Workshop on*. 2005.
75. Musgraves, J.D., et al., *Comparison of the optical, thermal and structural properties of Ge–Sb–S thin films deposited using thermal evaporation and pulsed laser deposition techniques.* Acta Materialia, 2011. **59**(12): p. 5032-5039.
76. Hu, J., et al., *Si-CMOS-compatible lift-off fabrication of low-loss planar chalcogenide waveguides.* Optics Express, 2007. **15**(19): p. 11798-11807.
77. Nazabal, V., et al., *Sputtering and Pulsed Laser Deposition for Near- and Mid-Infrared Applications: A Comparative Study of Ge25Sb10S65 and Ge25Sb10Se65 Amorphous Thin Films.* International Journal of Applied Ceramic Technology, 2011. **8**(5): p. 990-1000.
78. Zou, Y., et al., *Effect of annealing conditions on the physio-chemical properties of spin-coated As2Se3 chalcogenide glass films.* Optical Materials Express, 2012. **2**(12): p. 1723-1732.
79. Zou, Y., et al., *Solution Processing and Resist-Free Nanoimprint Fabrication of Thin Film Chalcogenide Glass Devices: Inorganic–Organic Hybrid Photonic Integration.* Advanced Optical Materials, 2014. **2**(8): p. 759-764.
80. Tsay, C., Y. Zha, and C.B. Arnold, *Solution-processed chalcogenide glass for integrated single-mode mid-infrared waveguides.* Optics Express, 2010. **18**(25): p. 26744-26753.
81. Mack, C., *Field Guide to Optical Lithography*. SPIE Press Book. 2006.
82. Xiao, S., et al., *Modeling and measurement of losses in silicon-on-insulator resonators and bends.* Optics Express, 2007. **15**(17): p. 10553-10561.

83. Hsueh, C.-H., *Modeling of elastic deformation of multilayers due to residual stresses and external bending.* Journal of Applied Physics, 2002. **91**(12): p. 9652-9656.
84. Sun, J.Y., et al., *Inorganic islands on a highly stretchable polyimide substrate.* Journal of Materials Research, 2009. **24**(11): p. 3338-3342.
85. Fan, L., et al., *Direct fabrication of silicon photonic devices on a flexible platform and its application for strain sensing.* Optics Express, 2012. **20**(18): p. 20564-20575.
86. Zhang, Y., C.T. Lin, and S. Yang, *Fabrication of Hierarchical Pillar Arrays from Thermoplastic and Photosensitive SU‐8.* small, 2010. **6**(6): p. 768-775.
87. Roelkens, G., et al., *Adhesive bonding of InP/InGaAsP dies to processed silicon-on-insulator wafers using DVS-bis-benzocyclobutene.* Journal of the Electrochemical Society, 2006. **153**(12): p. G1015-G1019.
88. Schiltz, A., *AN EMPIRICAL-MODEL FOR PLANARIZATION WITH POLYMER-SOLUTIONS.* Japanese Journal of Applied Physics Part 1-Regular Papers Short Notes & Review Papers, 1995. **34**(8A): p. 4185-4194.
89. Solehmainen, K., et al., *Adiabatic and Multimode Interference Couplers on Silicon-on-Insulator.* Photonics Technology Letters, IEEE, 2006. **18**(21): p. 2287-2289.
90. Fu, Y., et al., *Efficient adiabatic silicon-on-insulator waveguide taper.* Photonics Research, 2014. **2**(3): p. A41-A44.
91. Yariv, A., *Optical electronics in modern communications, 1997.* OxfordNew York: p. 526-531.
92. Sun, R., et al., *Impedance matching vertical optical waveguide couplers for dense high index contrast circuits.* Optics Express, 2008. **16**(16): p. 11682-11690.
93. Schwelb, O., *Transmission, group delay, and dispersion in single-ring optical resonators and add/drop filters - A tutorial overview.* Journal of Lightwave Technology, 2004. **22**(5): p. 1380-1394.
94. Hu, J., *Planar chalcogenide glass materials and devices.* Ph.D. thesis, 2009.
95. Li, L., et al., *A Fully-Integrated Flexible Photonic Platform for Chip-to-Chip Optical Interconnects.* Journal of Lightwave Technology, 2013. **31**(24): p. 4080-4086.
96. Kischkat, J., et al., *Mid-infrared optical properties of thin films of aluminum oxide, titanium dioxide, silicon dioxide, aluminum nitride, and silicon nitride.* Applied Optics, 2012. **51**(28): p. 6789-6798.
97. Jaroenworaluck, A., et al., *Characteristics of silica-coated TiO2 and its UV absorption for sunscreen cosmetic applications.* Surface and Interface Analysis, 2006. **38**(4): p. 473-477.
98. Yoshida, K., M. Tanagawa, and M. Atsuta, *Effects of filler composition and surface treatment on the characteristics of opaque resin composites.* Journal of Biomedical Materials Research, 2001. **58**(5): p. 525-530.

99. Kasuga, T., *Artificial dental root or bone implant material*. 1987, Hoya Corporation.
100. Khan, M.Z.R., et al., *Trapped charge dynamics in a sol–gel based TiO 2 high-k gate dielectric silicon metal–oxide–semiconductor field effect transistor.* Journal of Physics: Condensed Matter, 2009. **21**(21): p. 215902.
101. Chen, D., et al., *Mesoporous Anatase TiO2 Beads with High Surface Areas and Controllable Pore Sizes: A Superior Candidate for High-Performance Dye-Sensitized Solar Cells.* Advanced Materials, 2009. **21**(21): p. 2206-2210.
102. Armelao, L., et al., *Photocatalytic and antibacterial activity of TiO2 and Au/TiO2 nanosystems.* Nanotechnology, 2007. **18**(37).
103. Yu, J.C., et al., *Photocatalytic Activity, Antibacterial Effect, and Photoinduced Hydrophilicity of TiO2 Films Coated on a Stainless Steel Substrate.* Environmental Science & Technology, 2003. **37**(10): p. 2296-2301.
104. Qian, J., et al., *TiO2-Coated Multilayered SnO2 Hollow Microspheres for Dye-Sensitized Solar Cells.* Advanced Materials, 2009. **21**(36): p. 3663-3667.
105. Zhang, W., et al., *High sensitivity photonic crystal biosensor incorporating nanorod structures for enhanced surface area.* Sensors and Actuators B: Chemical, 2008. **131**(1): p. 279-284.
106. Zhang, W., et al., *Deposited nanorod films for photonic crystal biosensor applications.* Journal of Vacuum Science & Technology A, 2010. **28**(4): p. 996-1001.
107. Furuhashi, M., et al., *Development of microfabricated TiO2 channel waveguides.* Aip Advances, 2011. **1**(3).
108. Hayrinen, M., et al., *Low-Loss Titanium Dioxide Strip Waveguides Fabricated by Atomic Layer Deposition.* Lightwave Technology, Journal of, 2014. **32**(2): p. 208-212.
109. Choy, J.T., et al., *Integrated TiO2 resonators for visible photonics.* Optics Letters, 2012. **37**(4): p. 539-541.
110. Park, J., et al., *Titanium Dioxide Whispering Gallery Microcavities.* Advanced Optical Materials, 2014. **2**(8): p. 711-717.
111. Ge, L. and M.X. Xu, *Fabrication and characterization of TiO2 photocatalytic thin film prepared from peroxo titanic acid sol.* Journal of Sol-Gel Science and Technology, 2007. **43**(1): p. 1-7.
112. Ge, L., M.X. Xu, and H.B. Fang, *Synthesis of titanium oxide layers on glass substrates with aqueous refluxed sols (RS) and photocatalytic activities.* Journal of Materials Science, 2007. **42**(13): p. 4926-4934.
113. Swanepoel, R., *Determination of the thickness and optical constants of amorphous silicon.* Journal of Physics E: Scientific Instruments, 1983. **16**(12): p. 1214.
114. Bradley, J.D.B., et al., *Submicrometer-wide amorphous and polycrystalline anatase TiO2 waveguides for microphotonic devices.* Optics Express, 2012. **20**(21): p. 23821-23831.

115. Hu, J.J., et al., *Optical loss reduction in high-index-contrast chalcogenide glass waveguides via thermal reflow.* Optics Express, 2010. **18**(2): p. 1469-1478.
116. *Ls-Dyna Theory Manual*. 2006; Available from: http://www.lstc.com/pdf/ls-dyna_theory_manual_2006.pdf.
117. Bondi, S., *Capturing structural silicone non-linear behavior via the finite element method*, in *Glass Performance Days*. 2009: Tampere.
118. Tong, Z., et al., *Controlling the fibroblastic differentiation of mesenchymal stem cells via the combination of fibrous scaffolds and connective tissue growth factor.* Tissue Eng Part A, 2011. **17**(21-22): p. 2773-85.
119. Jha, A.K., et al., *Controlling the adhesion and differentiation of mesenchymal stem cells using hyaluronic acid-based, doubly crosslinked networks.* Biomaterials, 2011. **32**(10): p. 2466-78.
120. Li, L., et al., *A Fully-Integrated Flexible Photonic Platform for Chip-to-Chip Optical Interconnects.* Journal of Lightwave Technology, 2013. **31**(24): p. 4080-4086.
121. Li, L., et al. *Chip-to-chip optical interconnects based on flexible integrated photonics*. 2014.
122. Lu, D. *Recent advances on chip-to-chip optical interconnect*. in *Photonics and Optoelectronics Meetings 2009*. 2009. International Society for Optics and Photonics.
123. BOCKSTAELE , M.D.W. *Chip-to-chip parallel optical interconnects over optical backpanels based on arrays of multimode waveguides*. in *Proceedings of the 9th Annual Symposium of the IEEE/LEOS Benelux Chapter*. 2004.
124. Doany, F.E., et al. *Waveguide-coupled parallel optical transceiver technology for Tb/s-class chip-to-chip data transmission*. in *Integrated Optoelectronic Devices 2008*. 2008. International Society for Optics and Photonics.
125. Kromer, C., et al., *A 100-mW 4× 10 Gb/s transceiver in 80-nm CMOS for high-density optical interconnects.* Solid-State Circuits, IEEE Journal of, 2005. **40**(12): p. 2667-2679.
126. Li, M.-J., et al. *Multicore fiber for optical interconnect applications*. in *Opto-Electronics and Communications Conference (OECC), 2012 17th*. 2012. IEEE.
127. Van Steenberge, G., et al., *MT-compatible laser-ablated interconnections for optical printed circuit boards.* Lightwave Technology, Journal of, 2004. **22**(9): p. 2083-2090.
128. Bona, G.L., et al. *Characterization of parallel optical-interconnect waveguides integrated on a printed circuit board*. in *Proc. of SPIE Vol*. 2004.
129. Krishnamoorthy, A.V., et al., *Computer systems based on silicon photonic interconnects.* Proceedings of the Ieee, 2009. **97**(7): p. 1337-1361.
130. Batten, C., et al., *Building many-core processor-to-DRAM networks with monolithic CMOS silicon photonics.* Micro, IEEE, 2009. **29**(4): p. 8-21.
131. Chen, R.T., et al., *Fully embedded board-level guided-wave optoelectronic interconnects.* Proceedings of the Ieee, 2000. **88**(6): p. 780-793.

132. Liu, Y., et al., *Optoelectronic integration of polymer waveguide array and metal-semiconductor-metal photodetector through micromirror couplers.* Photonics Technology Letters, IEEE, 2001. **13**(4): p. 355-357.
133. Haney, M., R. Nair, and T. Gu. *Chip-scale integrated optical interconnects: a key enabler for future high-performance computing*. in *SPIE OPTO*. 2012. International Society for Optics and Photonics.
134. Nair, R., T. Gu, and M.W. Haney. *Hybrid chip-scale optical interconnects using multiple quantum well devices bonded to silicon*. in *Optical Interconnects Conference, 2012 IEEE*. 2012. IEEE.
135. Gu, T., R. Nair, and M.W. Haney, *Chip-level Multiple Quantum Well Modulator-based Optical Interconnects*, in *Chip-level Multiple Quantum Well Modulator-based Optical Interconnects*.
136. Gu, T., R. Nair, and M.W. Haney, *Prismatic coupling structure for intrachip global communication.* Quantum Electronics, IEEE Journal of, 2009. **45**(4): p. 388-395.
137. Liang, D., et al., *Hybrid integrated platforms for silicon photonics.* Materials, 2010. **3**(3): p. 1782-1802.
138. Roelkens, G., et al., *Adhesive Bonding of InP ／ InGaAsP Dies to Processed Silicon-On-Insulator Wafers using DVS-bis-Benzocyclobutene.* Journal of the Electrochemical Society, 2006. **153**(12): p. G1015-G1019.
139. Roelkens, G., et al., *III-V/Si photonics by die-to-wafer bonding.* Materials Today, 2007. **10**(7): p. 36-43.
140. Schares, L., et al., *Terabus: Terabit/second-class card-level optical interconnect technologies.* Selected Topics in Quantum Electronics, IEEE Journal of, 2006. **12**(5): p. 1032-1044.
141. Bosman, E., et al. *Flexible embedded active optical link*. in *Photonics Europe*. 2008. International Society for Optics and Photonics.
142. Gan, H., et al. *Pb-free microjoints (50/spl mu/m pitch) for the next generation microsystems: the fabrication, assembly and characterization*. in *Electronic Components and Technology Conference, 2006. Proceedings. 56th*. 2006. IEEE.
143. Young, I.A., et al., *Optical I/O Technology for Tera-Scale Computing.* Solid-State Circuits, IEEE Journal of, 2010. **45**(1): p. 235-248.
144. Hofrichter, J., et al., *A low-power high-speed InP microdisk modulator heterogeneously integrated on a SOI waveguide.* Opt. Express, 2012. **20**(9): p. 9363-9370.
145. Ahn, D., et al., *High performance, waveguide integrated Ge photodetectors.* Opt. Express, 2007. **15**(7): p. 3916-3921.
146. Madden, S.J., et al., *Long, low loss etched As2S3 chalcogenide waveguides for all-optical signal regeneration.* Opt. Express, 2007. **15**(22): p. 14414-14421.
147. Lamponi, M., et al., *Low-threshold heterogeneously integrated InP/SOI lasers with a double adiabatic taper coupler.* Photonics Technology Letters, IEEE, 2012. **24**(1): p. 76-78.

148. WTD. *10Gb/s PIN-TIA ROSA PTCM992-405*. 2009; Available from: http://www.wtd.com.cn/en/uploadfile/ptcm992-405.pdf.
149. JDSU. *JDSU 850 nm 10 G connectorized transmit optical sub-assembly (TOSA)*. 2012; Available from: http://www.jdsu.com/ProductLiterature/pl-xxd-00-s40-cx-ds-oc-ae.pdf.

Appendix A

COPYRIGHT PERMISSION

Work presented in Chapter 2.1.3 and Chapter 6 has been published in: *Foldable and Cytocompatible Sol-gel TiO_2 Photonics.* Scientific Reports, 2015. **5**.

Work presented in Chapter 2.2 and Chapter 4.1 has been published in *Flexible integrated photonics: where materials, mechanics and optics meet.* Optical Materials Express, 2013. **3**(9): p. 1313-1331.

Work presented in Chapter 3.2-3.4, Chapter 4.1-4.2 and Chapter 5 has been published in: *Integrated flexible chalcogenide glass photonic devices.* Nat Photon, 2014. **8**(8): p. 643-649.

Work presented in Chapter 7.1 has been published in: 1) *A Fully-Integrated Flexible Photonic Platform for Chip-to-Chip Optical Interconnects.* Journal of Lightwave Technology, 2013. **31**(24): p. 4080-4086; 2) *Chip-to-chip optical interconnects based on flexible integrated photonics*. Proc. SPIE 8991, Optical Interconnects XIV, 89910T, 2014.

Permission letters are listed below.

NATURE PUBLISHING GROUP LICENSE TERMS AND CONDITIONS

Dec 29, 2015

This is an Agreement between Lan Li ("You") and Nature Publishing Group ("Nature Publishing Group"). It consists of your order details, the terms and conditions provided by Nature Publishing Group, and the payment terms and conditions.

All payments must be made in full to CCC. For payment instructions, please see information listed at the bottom of this form.

License Number	3778230509468
License date	Dec 27, 2015
Licensed Content Publisher	Nature Publishing Group
Licensed Content Publication	Nature Photonics
Licensed Content Title	Integrated flexible chalcogenide glass photonic devices
Licensed Content Author	Lan Li, Hongtao Lin, Shutao Qiao, Yi Zou, Sylvain Danto, Kathleen Richardson
Licensed Content Date	Jun 29, 2014
Volume number	8
Issue number	8
Type of Use	reuse in a dissertation / thesis
Requestor type	academic/educational
Format	print and electronic
Portion	Full article
Circulation/distribution	>50,000
Author of this NPG article	yes
Your reference number	1
Title of your thesis / dissertation	Materials and Devices for Mechanically Flexible Integrated Photonics
Expected completion date	Jan 2016
Estimated size (number of pages)	137
Total	**0.00 USD**
Terms and Conditions	

Terms and Conditions for Permissions

Nature Publishing Group hereby grants you a non-exclusive license to reproduce this material for this purpose, and for no other use,subject to the conditions below:

1. NPG warrants that it has, to the best of its knowledge, the rights to license reuse of this material. However, you should ensure that the material you are requesting is original to Nature Publishing Group and does not carry the copyright of another entity (as credited in the published version). If the credit line on any part of the material you have requested indicates that it was reprinted or adapted by NPG with permission from another source, then you should also seek permission from that source to reuse the material.

2. Permission granted free of charge for material in print is also usually granted for any electronic version of that work, provided that the material is incidental to the work as a whole and that the electronic version is essentially equivalent to, or substitutes for, the print version.Where print permission has been granted for a fee, separate permission must be obtained for any additional, electronic re-use (unless, as in the case of a full paper, this has already been accounted for during your initial request in the calculation of a print run).NB: In all cases, web-based use of full-text articles must be authorized separately through the 'Use on a Web Site' option when requesting permission.

3. Permission granted for a first edition does not apply to second and subsequent editions and for editions in other languages (except for signatories to the STM Permissions Guidelines, or where the first edition permission was granted for free).

4. Nature Publishing Group's permission must be acknowledged next to the figure, table or abstract in print. In electronic form, this acknowledgement must be visible at the same time as the figure/table/abstract, and must be hyperlinked to the journal's homepage.

5. The credit line should read:
   Reprinted by permission from Macmillan Publishers Ltd: [JOURNAL NAME] (reference citation), copyright (year of publication)
   For AOP papers, the credit line should read:
   Reprinted by permission from Macmillan Publishers Ltd: [JOURNAL NAME], advance online publication, day month year (doi: 10.1038/sj.[JOURNAL ACRONYM].XXXXX)

   Note: For republication from the *British Journal of Cancer*, the following credit lines apply.
   Reprinted by permission from Macmillan Publishers Ltd on behalf of Cancer Research UK: [JOURNAL NAME] (reference citation), copyright (year of publication)For AOP papers, the credit line should read:
   Reprinted by permission from Macmillan Publishers Ltd on behalf of Cancer Research UK: [JOURNAL NAME], advance online publication, day month year (doi: 10.1038/sj.[JOURNAL ACRONYM].XXXXX)

6. Adaptations of single figures do not require NPG approval. However, the adaptation should be credited as follows:

   Adapted by permission from Macmillan Publishers Ltd: [JOURNAL NAME] (reference citation), copyright (year of publication)

   Note: For adaptation from the *British Journal of Cancer*, the following credit line applies.
   Adapted by permission from Macmillan Publishers Ltd on behalf of Cancer Research UK: [JOURNAL NAME] (reference citation), copyright (year of publication)

7. Translations of 401 words up to a whole article require NPG approval. Please visit http://www.macmillanmedicalcommunications.com for more information.Translations of up to a 400 words do not require NPG approval. The translation should be credited as follows:

   Translated by permission from Macmillan Publishers Ltd: [JOURNAL NAME] (reference citation), copyright (year of publication).

   Note: For translation from the *British Journal of Cancer*, the following credit line applies.
   Translated by permission from Macmillan Publishers Ltd on behalf of Cancer Research UK: [JOURNAL NAME] (reference citation), copyright (year of publication)

We are certain that all parties will benefit from this agreement and wish you the best in the use of this material. Thank you.
Special Terms:
v1.1

Questions? customercare@copyright.com or +1-855-239-3415 (toll free in the US) or +1-978-646-2777.

Dear Lan,

Thank you for seeking permission from SPIE to reprint material from our publications. As author, SPIE shares the copyright with you, so you retain the right to reproduce your paper in part or in whole.

Publisher's permission is hereby granted under the following conditions:

(1) the material to be used has appeared in our publication without credit or acknowledgment to another source; and

(2) you credit the original SPIE publication. Include the authors' names, title of paper, volume title, SPIE volume number, and year of publication in your credit statement.

Sincerely,

Nicole Harris

Administrative Editor, SPIE Publications

1000 20th St.

Bellingham, WA 98225

+1 360 685 5586 (office)

nicoleh@spie.org

SPIE Publisher's permission is hereby granted under the following conditions: (1) you obtain permission of the author(s); (2) the material to be used has appeared in our publication without credit or acknowledgment to another source; and (3) you redit the original SPIE publication. Include the authors' names, title of aper, volume title, SPIE volume number, and year of publication in your redit statement.

Director of Publications
SPIE
PO Box 10, Bellingham, WA 98227-0010 USA
360/676-3290 (Pacific Time) eric@spie.org

Eric Pepper, Director of Publications Date 12/29/15

SPIE is the international society for optics and photonics. http://SPIE.org